

AFIT/GE/ENG/02M-21



FABRICATION TECHNIQUES FOR III-V
MICRO-OPTO-ELECTRO-MECHANICAL SYSTEMS

THESIS
Jeremy A. Raley
Captain, USAF

AFIT/GE/ENG/02M-21

DEPARTMENT OF THE AIR FORCE
AIR UNIVERSITY

AIR FORCE INSTITUTE OF TECHNOLOGY
Wright-Patterson Air Force Base, Ohio

Approved for public release; distribution unlimited.

Report Documentation Page		
Report Date 26 Mar 02	Report Type Final	Dates Covered (from... to) Jun 01 - Mar 02
Title and Subtitle Fabrication Techniques for III-V Micro-Opto-Electro-Mechanical Systems		Contract Number
		Grant Number
		Program Element Number
Author(s) Captain Jeremy A. Raley, USAF		Project Number
		Task Number
		Work Unit Number
Performing Organization Name(s) and Address(es) Air Force Institute of Technology Graduate School of Engineering and Management (AFIT/EN) 2950 P Street, Bldg 640 WPAFB OH 45433-7765		Performing Organization Report Number AFIT/GE/ENG/02M-21
Sponsoring/Monitoring Agency Name(s) and Address(es) AFRL/SNDD ATTN: Dr. Thomas R. Nelson, Jr. 2241 Avionics Circle, Rm C2G69 WPAFB OH 45433-7322		Sponsor/Monitor's Acronym(s)
		Sponsor/Monitor's Report Number(s)
Distribution/Availability Statement Approved for public release, distribution unlimited		
Supplementary Notes		
<p>Abstract</p> <p>This thesis studies selective etching techniques for the development of Al_xGa_{1-x}As micro-opto-electro-mechanical systems (MOEMS). New MEMS technology based on materials such as Al_xGa_{1-x}As enables the development of micro-systems with embedded active micro-optical devices. Tunable micro-lasers and optical switching based on MOEMS technology will improve future wavelength division multiplexing (WDM) systems. WDM vastly increases the speed of military communications and sensor data processing. From my designs, structures are prepared by molecular beam epitaxy. I design a mask set for studies of crystal plane selectivity. I perform a series of experiments on the selective removal of GaAs and AlAs. I convert AlAs and Al_{0.98}Ga_{0.02}As layers within the test structures to AlO_x and Al_{0.98}Ga_{0.02}O_x and perform selective etching experiments on these sacrificial oxide layers. The etchants and materials studied showed high selectivity for removal of all materials studied. Results suggest that any of these material layers are useful as sacrificial layers for general MOEMS technology. I design, fabricate, and characterize prototype III-V MOEMS. Using AlO_x sacrificial layers, I investigate a new technique for transplanting microcavity light-emitting devices. I successfully transplant arrays of light-emitting diodes. Finally, I discuss ideas on how this work forms the basis for nano-electro-mechanical systems (NEMS) fabrication in III-V materials.</p>		

Subject Terms Microelectromechanical Systems, Aluminum Gallium Arsenide, Etching, Oxidation, Micromachining, Micro-Opto-Electro-Mechanical Systems, III-V Micromachining, Lift-off Optical Devices	
Report Classification unclassified	Classification of this page unclassified
Classification of Abstract unclassified	Limitation of Abstract UU
Number of Pages 176	

The views expressed in this thesis are those of the author and do not reflect the official policy or position of the United States Air Force, the United States Department of Defense or the United States Government.

AFIT/GE/ENG/02M-21

FABRICATION TECHNIQUES FOR III-V
MICRO-OPTO-ELECTRO-MECHANICAL SYSTEMS

THESIS

Presented to the Faculty of the Graduate School of Engineering and Management
of the Air Force Institute of Technology
Air University
In Partial Fulfillment of the
Requirements for the Degree of
Master of Science in Electrical Engineering

Jeremy A. Raley, B.S.E.E.

Captain, USAF

26 March 2002

Approved for public release; distribution unlimited.

FABRICATION TECHNIQUES FOR III-V
MICRO-OPTO-ELECTRO-MECHANICAL SYSTEMS

THESIS

Jeremy A. Raley, B.S.E.E.

Captain, USAF

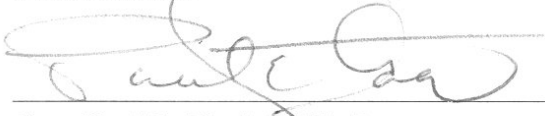
Approved:



Lt Col James A. Lott, Ph. D.
Professor of Electrical Engineering
Thesis Advisor

01 MARCH 2002

Date



Capt Paul E. Kladitis, Ph. D.
Assistant Professor of Electrical Engineering
Committee Member

01 MARCH 2002

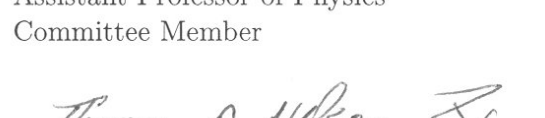
Date



Lt Col Michael A. Marciniak, Ph. D.
Assistant Professor of Physics
Committee Member

1 Mar 02

Date



Thomas R. Nelson, Jr., Ph. D.
Air Force Research Laboratory
Committee Member

1 March 02

Date

Acknowledgements

First, I would like to thank my Creator for providing me with insight into a small part of His creation. I am also grateful for His protection while working in the laboratory and His provision for my family during this time.

I would like to thank my wife and son for providing a loving home even when I was not available to do my part. A Proverbs 31 woman that supports me the way my wife has is an uncommon find and I thank God for her every day.

As a thesis advisor, Lt Col Lott gave me ideas and then allowed me to investigate them independently. I appreciate his trust and encouragement throughout my research and course work.

My sponsor, Dr. Nelson, was equally confident in me and encouraged my independent research. I am also grateful for his help in refining my processing ideas and useful suggestions for making them better, simpler, or possible.

The technicians and engineers at the Air Force Research Laboratory are also very much appreciated. Their attitudes contributed significantly to my enjoyment of this research, and I look forward to continued work with these competent professionals.

Finally, I would like to thank my parents, siblings and in-laws for their encouragement. I especially want to thank them for their support when my son was born during my research quarter.

Table of Contents

	Page
Acknowledgements	iii
List of Figures	ix
List of Tables	xviii
List of Symbols	xix
List of Abbreviations	xxi
Abstract	xxii
I. Introduction	1-1
1.1 Motivation	1-1
1.1.1 Applications	1-2
1.1.2 Scientific Merit	1-3
1.2 Brief Background of III-V MEMS	1-3
1.3 Problem Statement	1-4
1.3.1 Accomplishments	1-4
1.3.2 Uniqueness of Thesis	1-4
1.4 Thesis Scope and Approach	1-5
1.5 Main Results	1-6
1.6 Thesis Overview	1-6
Bibliography	1-8

	Page
II. Background	2-1
2.1 Introduction	2-1
2.2 Microelectromechanical Systems	2-1
2.2.1 Fabrication and Processing	2-1
2.2.2 Electrostatic Actuation	2-4
2.3 MEMS Materials	2-9
2.3.1 Silicon	2-9
2.3.2 $\text{Al}_x\text{Ga}_{1-x}\text{As}$ MEMS	2-10
2.4 Molecular Beam Epitaxy for Aluminum Gallium Arsenide	2-14
2.4.1 Growth by Molecular Beam Epitaxy	2-14
2.4.2 Regrowth with MBE	2-15
2.5 Photolithography	2-18
2.6 Metal Deposition	2-18
2.7 Etching	2-21
2.7.1 Wet Etching	2-21
2.7.2 Dry Etching	2-23
2.7.3 Reactive Ion Etching	2-24
2.8 Wet Oxidation of AlAs	2-25
2.9 Structure Release	2-30
2.9.1 Wet Release	2-30
2.9.2 Dry Release	2-33
2.9.3 Wet Release with CO_2 Drying	2-34
2.10 Optical Devices	2-36
2.10.1 Distributed Bragg Reflectors	2-36
2.10.2 Fabry-Perot Interferometers	2-37
2.11 Zygo New View 5000 Interferometry System	2-39
2.12 Conclusion	2-39

	Page
Bibliography	2-41
III. Experimental Procedures	3-1
3.1 Introduction	3-1
3.2 Process Steps	3-1
3.2.1 Metal Deposition	3-1
3.2.2 DBR Removal	3-2
3.2.3 Mesa Etch	3-3
3.3 Mask Design	3-4
3.3.1 Structures for Etch Studies	3-4
3.3.2 Tunable Fabry-Perot Filters	3-8
3.4 Selective Etch Studies	3-13
3.4.1 Etch Study Material	3-13
3.4.2 Dry Etch Study Experimental Procedure . . .	3-13
3.4.3 Wet Etch Study for Selective GaAs Removal: Experimental Procedure	3-16
3.4.4 Oxidation Etch Study: Experimental Procedure	3-18
3.5 III-V MOEMS Applications	3-19
3.5.1 Tunable Fabry-Perot Interferometer	3-19
3.5.2 Lift-off Optical Devices	3-23
3.6 Conclusions	3-25
Bibliography	3-26
IV. Results and Analysis	4-1
4.1 Introduction	4-1
4.2 Dry Etch Study	4-1
4.3 Wet Etch Study for Selective GaAs Removal	4-1
4.3.1 Etch Rate Characterization	4-4

	Page
4.3.2 Etch Selectivity Characterization	4-4
4.4 Oxidation Etch Study	4-12
4.4.1 Oxidation Rate and Crystal Plane Selectivity Characterization	4-12
4.4.2 Oxidation Etching Material Selectivity	4-13
4.5 Applications	4-17
4.5.1 Tunable Fabry-Perot Filters with GaAs Sacrificial Layers	4-17
4.5.2 Tunable Fabry-Perot Filters with $\text{Al}_{0.98}\text{Ga}_{0.02}\text{As}$ Sacrificial Layers	4-20
4.5.3 Lift-off Optical Devices	4-24
4.6 Conclusion	4-30
Bibliography	4-32
V. Conclusions	5-1
5.1 Introduction	5-1
5.2 Concerning Experiments	5-1
5.2.1 Dry Etch Study	5-1
5.2.2 Wet Etch Study	5-2
5.2.3 Oxidation Etch Study	5-3
5.2.4 Applications	5-3
5.3 Lessons Learned	5-8
5.3.1 Semiconductor Processing	5-8
5.3.2 Etch Study Mask Design	5-13
5.3.3 Mechanical Structure Mask Design	5-13
5.4 Contributions	5-13
5.4.1 III-V Micromachining	5-13
5.4.2 Lift-Off Optical Devices	5-13

	Page
5.5 Future Work	5-14
5.5.1 Tunable Optical Devices	5-14
5.5.2 Nano-Electro-Mechanical-Systems	5-14
5.5.3 Lift-Off Optical Devices	5-15
5.6 Conclusion	5-16
Bibliography	5-17
Appendix A. Processing Recipes	A-1
A.1 Dry Etch Study Processing Recipe	A-1
A.2 Wet Etch Study for Selective GaAs Removal Processing Recipe	A-5
A.3 Oxidation Etch Study Processing Recipe	A-7
A.4 Fabrication of Tunable Fabry-Perot Interferometers . .	A-11
A.5 Fabrication of Lift-off Optical Devices	A-14
Appendix B. Materials and Epitaxial Growths Used	B-1
B.1 Details for Growth G2-2696	B-2
B.2 Details for Growth G2-2697	B-2
B.3 Details for Growth G2-2698	B-2
B.4 Details for Growth G2-2718	B-3
B.5 Details for Growth G2-2722	B-3
B.6 Details for Growth G2-2738	B-4
B.7 Details for Growth G2-2747	B-4
B.8 Details for Growth G2-2748	B-5
B.9 Growth Details for UNM Run 1152	B-5
B.10 Growth Details for UNM Run 1184	B-6

List of Figures

Figure		Page
1.1.	Illustration of the concept of Wavelength Division Multiplexing [11].	1-2
2.1.	Similarities and differences between bulk and surface micromachining [36].	2-2
2.2.	Surface micromachining process used in my work.	2-3
2.3.	Electrostatic actuation of a micromachined cantilever [44].	2-4
2.4.	Plot of the relationship between normalized load and normalized deflection as given by Equation 2.7 (solid line) and curve fit to actual deflection versus load data gathered by Petersen [44] (dashed line). The abrupt horizontal line indicates sudden, complete deflection of the cantilever at approximately one third the original distance between the cantilever and the substrate ($\Delta = 0.33$).	2-8
2.5.	Circular micromotor structure fabricated using MUMPs® before (a) and after (b) removal of the sacrificial layers [43].	2-11
2.6.	Structures fabricated from $\text{Al}_x\text{Ga}_{1-x}\text{As}$ compounds: (a) cantilevers formed by bulk micromachining [17], and (b) a comb resonator made using surface micromachining with epitaxial regrowth [19]	2-12
2.7.	Diagram of a solid source molecular beam epitaxy system [48].	2-15
2.8.	Comparison and contrast between structures fabricated (a) with, and (b) without epitaxial regrowth.	2-17
2.9.	Metalized ohmic contacts deposited on VCSELs by e-beam evaporation.	2-20
2.10.	Diagram of a generic wet etching system, after [48].	2-21
2.11.	Comparison of isotropic and anisotropic wet etching [28].	2-22
2.12.	Diagram of a dry or gaseous etching system [21].	2-23

Figure		Page
2.13.	Example of a GaAs and $\text{Al}_x\text{Ga}_{1-x}\text{As}$ ($x = 0.1, 0.9$) structure etched using BCl_3	2-24
2.14.	Diagram of the wet oxidation system used in my research [31]. The one-liter water bottle is warmed to approximately 50 °C. The phase separator traps liquid water droplets to keep them from propagating through the system and causing erroneous pressure or mass flow readings.	2-25
2.15.	Graphical illustration of the effects of time and temperature on oxidation progress [14].	2-26
2.16.	TEM image of oxidation progress depending only on layer thickness [11].	2-27
2.17.	Graphical illustration of the effect of thickness upon oxidation rate [24].	2-28
2.18.	Optical image where the crystal plane selectivity of the oxidation process is manifested [31].	2-29
2.19.	Illustration of the concept of sacrificial etching, after [13]. . .	2-30
2.20.	Forces involved in the problem of stiction [28]. In my structures, the opposing forces are limited to those resulting from the spring constant of the released structure.	2-31
2.21.	Image of an array of fixed-fixed beam structures fabricated using the MUMPs® process where stick-down has occurred. This array was processed with wet-release and no precautions were taken in its drying. The forces causing this stick-down are most likely capillary in nature rather than residual stress as evidenced by the fact that the longer beam did not experience stiction. The longer beam would have been more prone to buckling if the deflection were caused by residual stress. The longer structure did not stick down due to capillary forces because of the random nature of stiction induced by surface tension [46]. . .	2-32

Figure	Page
2.22. Phases of CO ₂ for various combinations of pressure and temperature with the regions used for release annotated, after [23]. The release process begins at point 1, where liquid CO ₂ displaces methanol. The pressure of the drying chamber is raised (point 2) to prevent the liquid from evaporating in the normal fashion when the temperature is raised (point 3). The CO ₂ now exists in a supercritical state where it is both a liquid and a gas with no interface between the two. As the pressure is released the CO ₂ becomes all vapor and escapes from the drying chamber (point 4).	2-35
2.23. Illustration of a basic DBR, after [16].	2-36
2.24. Mathematically modelled power reflectance and transmittance versus wavelength at normal incidence for a DBR designed to be 97% reflecting at $\lambda_{design} = 9800 \text{ \AA}$. The high-index layers of the 14 pair quarter-wave stack are composed of Al _{0.1} Ga _{0.9} As ($n = 3.47$, 706 Å thick) and the low-index layers are composed of Al _{0.9} Ga _{0.1} As ($n = 3.02$, 810 Å thick) all on a GaAs substrate. This model assumes no absorption, since absorption is negligible over the range shown for these materials [42].	2-37
2.25. Mathematically modelled power reflectance and transmittance versus wavelength for a Fabry-Perot interferometer with $\lambda_{design} = 980 \text{ nm}$. The compositions and thicknesses of layers are identical to those in Figure 2.24, except that the two DBRs are designed to be 99% reflecting. The microcavity is composed of air and is 4900 Å-thick [42].	2-38
3.1. Schematic of my process after the metal deposition step. . .	3-2
3.2. Schematic of a Fabry-Perot etalon after DBR removal,prior to mesa definition.	3-3
3.3. Schematic of a study structure after mesa definition and prior to selective oxidation of AlAs or selective etching of GaAs. .	3-3

Figure		Page
3.4.	Crystal plane selectivity evidenced by the square pattern left after etching from a structure that was initially round. The structural layer was mechanically removed from the top to show this behavior in the sacrificial layer.	3-4
3.5.	Mask pattern aligned to GaAs crystal planes for etch studies. These shapes were placed at several different orientations relative to the wafer to determine which would accelerate etching or oxidation and which would inhibit etching or oxidation.	3-5
3.6.	The basic mask unit containing two arrays of various sizes of each of the test shapes included in the etch study.	3-6
3.7.	Mask reticle for the basic etch studies. Includes features shown in Figure 3.6 arranged at various angles.	3-7
3.8.	Mask layout of one of my basic circle base, circle mirror structures.	3-8
3.9.	The standard used for measuring cantilevers that connect to circles or diamonds. The measurement is taken from the point where both corners of the rectangular cantilever make contact with the edge of the base or mirror.	3-9
3.10.	Layout of the structures investigated while fabricating a tunable Fabry-Perot filter. The features are placed at angles of 45° and 54.74° relative to the bottom row in an attempt to take advantage of crystal plane selectivity.	3-10
3.11.	Example layout of a piston mirror [5].	3-11
3.12.	Unit of the mask used to define tunable Fabry-Perot interferometer structures. Shaded areas indicate regions where the top DBR will be removed to allow for in-situ monitoring during the selective oxidation of AlAs or Al _{0.98} Ga _{0.02} As sacrificial layers.	3-12
3.13.	Schematic of a general epitaxial growth consisting of a sacrificial layer between two DBRs.	3-13
3.14.	Photograph of the mask used to define circular mesas for dry and wet etch studies. Circle sizes shown are 16, 18, 20, 25, 35, 50, and 100 μm.	3-14

Figure		Page
3.15.	Plot of power reflectance at 789 nm as material is etched away. (a) Calculated power reflectance at normal incidence versus distance etched from original top surface. (b) Measured power reflectance versus etch time at near normal incidence. Structural information for the growth referenced in this figure is available in Appendix B.	3-15
3.16.	Image of metal deposited on etch study structures for the oxidation etch study.	3-18
3.17.	Schematic of an epitaxial growth consisting of a sacrificial layer between two DBRs.	3-20
3.18.	Image of tunable Fabry-Perot structures before the sacrificial layer release etch.	3-21
3.19.	Image of a MEM-tunable Fabry-Perot etalon after the release etch. This device was produced using sample G2-2747 (see Appendix B for detailed structure).	3-22
3.20.	Example of an epitaxial growth for the purpose of fabricating lift-off microcavity light-emitting devices.	3-23
3.21.	An array of optical devices after metal deposition and mesa definition.	3-24
4.1.	SEM images of test structures after a dry etch. (a) Image taken after initial RIE mesa definition. There is still a layer of photoresist atop the structure to protect it from any directional etching that might happen during the selective dry etch. (b) Image taken after exposure to BCl_3 and SF_6 to selectively remove GaAs. The image is magnified so that it is clear that the GaAs layer (the bulk material visible just above the bottom DBR layers where the mesa etch was stopped) has not been etched.	4-2

Figure	Page
4.2. Image of a sample processed from wafer G2-2696 where bulk GaAs has been selectively removed from between two DBRs. (a) Missing material is apparent from an angled view of the structure. (b) The structure was milled using a focused ion beam (FIB) system in order to look inside the layers and make the selective removal more apparent. Note that undulating edges were caused by mask degradation during RIE.	4-3
4.3. SEM image of a wafer where some of the structures have been completely undercut and others that are slightly larger still remain.	4-4
4.4. Graphical representation of the data collected during experiments to determine the etch rate of $C_6H_8O_7:K_3C_7H_5O_2:H_2O_2$ 10:10:3 on a 1.5 μm GaAs sacrificial layer.	4-5
4.5. Structure where the top DBR has been milled to determine the removal rate of $Al_{0.1}Ga_{0.9}As$	4-6
4.6. Image of an undercut and displaced DBR structure illustrating the smoothness of the top surface after the GaAs is selectively removed.	4-7
4.7. Image illustrating crystal plane selectivity by virtue of the fact that the sacrificial GaAs started patterned as a circle and ended up patterned as a diamond.	4-8
4.8. Image of an array of structures used to study crystal plane selectivity for GaAs etched with citric acid: $K_3C_7H_5O_2:H_2O_2$. The structural layer was mechanically removed from the top to show this behavior in the sacrificial layer.	4-9
4.9. Images of structures where the middle was undercut before the edges due to crystal plane selectivity. This structure has been milled with a FIB to show that its edges are attached while its middle is released.	4-11

Figure	Page
4.10. SEM image of a DBR structure consisting of alternating layers of $\text{Al}_{0.1}\text{Ga}_{0.9}\text{As}$ and $\text{Al}_{0.9}\text{Ga}_{0.1}\text{As}$ on top of an AlAs sacrificial layer (see UNM 1152 in Appendix B) after oxidation and oxide removal. A portion of the structure has been milled to allow for a determination of selectivity among the layers.	4-14
4.11. Image of a structure released by oxidation and selective oxide removal. This image illustrates the smoothness of the material left behind by this selective removal technique.	4-15
4.12. Effect of oxidation and oxide removal on gold contacts. (a)Roughness and pitting in the surface of the gold contact. (b)Structure deformation due to wet release and CO_2 drying.	4-16
4.13. Graph of the data collected for actuation voltage versus deflection distance for a cantilever mirror structure with a circular base and circular contact ($400 \mu\text{m}$ and $100 \mu\text{m}$ -diameter respectively released by selectively removing GaAs).	4-18
4.14. (a)Reflectivity plots illustrating the undesirable optical performance of my tunable Fabry-Perot filters. These structures consist of $\text{Al}_{0.1}\text{Ga}_{0.9}\text{As} / \text{Al}_{0.9}\text{Ga}_{0.1}\text{As}$ DBRs surrounding a GaAs sacrificial layer (sample G2-2747). (b)Modelled reflectivity plot from the growth details in Appendix B.7 assuming complete removal of the GaAs sacrificial layer.	4-19
4.15. Series of images for varying applied voltages depicting the irregular fringe lines due to mirror deformation during oxidation. The series shows how the lines shift as actuation voltage is increased. These structures are $100 \mu\text{m}$ measured between their two closest vertices. They were fabricated from growth G2-2738.	4-21
4.16. (a)Reflectivity plots illustrating the undesirable optical performance of my tunable Fabry-Perot filters. These structures consist of $\text{Al}_{0.1}\text{Ga}_{0.9}\text{As} / \text{Al}_{0.9}\text{Ga}_{0.1}\text{As}$ DBRs surrounding a $\text{Al}_{0.98}\text{Ga}_{0.02}\text{As}$ sacrificial layer (sample G2-2738). (b)Modelled reflectivity plot from the growth details in Appendix B.6 assuming complete removal of the $\text{Al}_{0.98}\text{Ga}_{0.02}\text{As}$ sacrificial layer.	4-23

Figure		Page
4.17.	Image of a lift-off optical device that I attempted to release with HF:DIW 1:1.	4-24
4.18.	Profile obtained using a Tencor profilometer of a lift-off optical device where release was attempted using HF:DIW 1:1.	4-25
4.19.	SEM image of $\text{Al}_{0.1}\text{Ga}_{0.9}\text{As}$ disks left after an attempt to release an optical device from its substrate using HF:ISP:DIW 1:3:6.	4-26
4.20.	Image of microcavity devices on the acceptor substrate after successful, intact removal from their native substrate.	4-27
4.21.	Electroluminescence spectral profiles of the optical devices used in the microcavity device lift-off study: (a) before release, and (b) after transplantation. These measurements were both taken at a temperature of 300 Kelvins (K) using a continuous current.	4-28
4.22.	Reflectivity plots showing cavity resonance for the middle and edge of sample UNM 1184.	4-29
4.23.	L-I-V characteristics of a transplanted RCLED. Luminescence is the upper curve and is measured by the scale on the right. Current is the lower curve and is read according to the scale on the left.	4-30
4.24.	SEM image of the thin bridge connecting the RCLED lift-off devices to one another and causing them to transplant in arrays.	4-31
5.1.	Measured and modelled reflectivity plots taken from sample G2-2747 (tunable Fabry-Perot filter with GaAs sacrificial) before any processing was performed.	5-5
5.2.	Measured and Modelled reflectivity plots taken from sample G2-2738 (tunable Fabry-Perot filter with $\text{Al}_{0.98}\text{Ga}_{0.02}\text{As}$ sacrificial) before any processing was performed.	5-6
5.3.	A proposed design for a lithography mask that would facilitate better lift-off of small structures both (a) alone and (b) in strings.	5-7
5.4.	Image showing the thin residual film that prevented wet etching after RIE and photoresist removal.	5-9

Figure	Page
5.5. SEM images of residual material left behind after a release etch.	5-11
5.6. Zygo interferometry system image of a mirror warped during actuation due to incomplete release. (a) Flat mirror with no actuation voltage. (b) Bent mirror with 11 V applied. . . .	5-12

List of Tables

Table	Page
1.1. Combinations of materials and etchants studied.	1-5
2.1. Comparison of properties of Si and GaAs for micromachining [35].	2-13
3.1. Combinations of base and mirror shapes for studies of MEM-tunable Fabry-Perot interferometers.	3-10
3.2. Conditions for the intial dry etch for selective removal of GaAs [7].	3-16
3.3. Etch parameters for the dry etch study [7].	3-17
4.1. Data collected for groups of 4 structures from a single sample after 55 minutes in etching solution concerning the etch progress for several shapes at various crystal plane orientations for selective removal of GaAs.	4-10
4.2. Data collected for groups of 4 structures from a single sample concerning the oxidation progress of several shapes at various crystal plane orientations for an oxidation layer thickness of 329 nm after 2 hours and 34 minutes in the wet oxidation system. This was accomplished using sample UNM 1152 (see Appendix B for growth plan)	4-12

List of Symbols

Symbol	Page
$\text{Al}_x\text{Ga}_{1-x}\text{As}$ Aluminum Gallium Arsenide	1-1
InP Indium Phosphide	1-1
GaAs Gallium Arsenide	1-4
Al_xO_y Aluminum Oxide	1-4
BCl_3 Boron Trichloride	1-5
SF_6 Sulfur Hexafluoride	1-5
$\text{C}_6\text{H}_8\text{O}_7$ Citric Acid	1-5
$\text{K}_3\text{C}_7\text{H}_5\text{O}_2$ Tripotassium Citrate	1-5
H_2O_2 Hydrogen Peroxide	1-5
HF Hydrofluoric Acid	1-5
KOH Potassium Hydroxide	1-5
AlAs Aluminum Arsenide	2-4
\mathcal{L} Normalized Load (dimensionless)	2-6
SiO_2 Silicon Dioxide	2-9
SiC Silicon Carbide	2-9
SiN Silicon Nitride	2-9
eV electron Volts	2-13
$^{\circ}\text{C}$ Degrees Centigrade	2-14
$^{\circ}\text{F}$ Degrees Fahrenheit	2-18
Au Gold	2-19
Ti Titanium	2-19
\AA Angstroms	2-19
XeF_2 Xenon Difluoride	2-33
BrF_3 Bromine Trifluoride	2-33
ClF_3 Chlorine Trifluoride	2-33

Symbol		Page
O ₂	Oxygen	2-33
Cl	Chlorine	2-33
F	Fluorine	2-33
SiCl ₄	Silicon Tetrachloride	2-33
SiF ₄	Silicon Tetrafluoride	2-34
λ_{design}	Design Wavelength (\AA , nm, or μm)	2-36
n	Index of Refraction (dimensionless)	2-36
HCl	Hydrochloric Acid	3-16
M	Molarity (moles/liter)	3-17
mA	Millamps	4-29

List of Abbreviations

Abbreviation		Page
USAF	United States Air Force	1-1
DoD	Department of Defense	1-1
WDM	Wavelength Division Multiplexing	1-2
MEMS	MicroElectroMechanical Systems	1-3
AFRL	Air Force Research Laboratory	1-3
MOEMS	Micro-Opto-Electro-Mechanical Systems	1-3
VCSEL	Vertical Cavity Surface Emitting Laser	1-4
SEM	Scanning Electron Microscope	1-4
MBE	Molecular Beam Epitaxy	1-5
RIE	Reactive Ion Etching	1-5
DBR	Distributed Bragg Reflector	1-5
DIW	Deionized Water	1-5
ISP	Isopropyl Alcohol	1-5
RCLEDs	Resonant Cavity Light Emitting Diodes	1-6
ICs	Integrated Circuits	2-1
MUMPs®	Multi-User MEMS Process	2-9
UV	Ultraviolet	2-18
e-beam	Electron Beam	2-19
TEM	Tunneling Electron Microscope	2-26
ICP	Inductively Coupled Plasma	3-14
sccm	Standard Cubic Centimeters per Minute	3-17
ISP	Isopropyl Alcohol	3-24
FIB	Focused Ion Beam	4-1
L-I-V	Light Power-Current-Voltage	4-29

Abstract

This thesis studies techniques for selective removal of semiconductor material in $\text{Al}_x\text{Ga}_{1-x}\text{As}$ systems for the purpose of fabricating Micro-Opto-Electro-Mechanical Systems (MOEMS). Fabrication in $\text{Al}_x\text{Ga}_{1-x}\text{As}$ allows for the emission, control, and detection of light from the near-infrared to the visible region of the spectrum. Specifically, MOEMS will enable wavelength division multiplexing (WDM) in the next generations of communications equipment, which will multiply the amount of information that can be sent through existing optical fiber cabling.

This work was accomplished by performing an etch study on the selective removal of GaAs from an $\text{Al}_x\text{Ga}_{1-x}\text{As}$ structure. The technique of oxidizing AlAs or $\text{Al}_{0.98}\text{Ga}_{0.02}\text{As}$ and removing the oxide was also investigated along with methods for the direct removal of AlAs. The knowledge gained during these etch studies was then applied to the fabrication of Micro-Electro-Mechanical tunable Fabry-Perot filters as well as lift-off microcavity light emitting devices.

The etchants and materials studied showed high selectivity for removal of both GaAs and AlAs. Mechanical structures were fabricated and actuated using these techniques and resonant cavity light emitting diodes were transplanted from their native substrate to another substrate singly and in arrays.

This thesis presents three methods for fabricating MEM systems in III-V materials. This fabrication knowledge will be applied to the fabrication of devices such as tunable vertical cavity surface emitting lasers (VCSELs). Transplantable optical devices have broad applications in the areas of computing and communications. This work can also be used as a basis for fabrication of Nano-Electro-Mechanical Systems using crystalline III-V materials.

FABRICATION TECHNIQUES FOR III-V MICRO-OPTO-ELECTRO-MECHANICAL SYSTEMS

I. Introduction

1.1 Motivation

The flow of information is the key to the standard of living enjoyed in the modern era. Although it is now possible to move great amounts of information at incredible speeds, the demand for bandwidth is always in excess of the bandwidth available. Because much of modern data flow takes place utilizing optical devices, the equipment required to increase the volume and rate of information flow requires the use of III-V materials such as aluminium gallium arsenide ($\text{Al}_x\text{Ga}_{1-x}\text{As}$) or indium phosphide (InP). These materials are required because they are capable of integrating the electrical and optical properties necessary for modern signalling applications. The properties and processing methods for III-V semiconductor materials are not completely mature. In this thesis, I undertake the study of new fabrication techniques for the next generation of information systems.

My work is of particular importance to the United States Air Force (USAF) because information superiority is one of the core competencies identified in the United States Department of Defense's (DoD) strategic planning document Joint Vision 2010. Information superiority is of great concern and wide application to the military because improved information technology can “significantly impact future military operations by providing decision makers with accurate information in a timely manner” [13]. My work enables the fabrication of devices that improve information flow, thus leading to information superiority for the U.S. military and improved communication capabilities for the private sector.

1.1.1 Applications. The first, primitive radios operated by discharging a high voltage across an air gap and detecting the resulting impulse at a distant receiver. In essence, this method of communication utilized the entire electromagnetic spectrum and communicated at Morse code speed [3]. Although this scheme of communication is clearly inefficient, communications via fiber-optic cables are in much the same state today relative to what is possible. In radio, the inefficiency was overcome by dividing the useable electromagnetic spectrum into channels so that multiple communications could take place in the same space at the same time [2]. Wavelength division multiplexing (WDM) will allow the same progress with signals sent over fiber optic cabling, effectively multiplying the amount of data that can be transferred with no increase or replacement of the transmitting medium [9]. This concept is illustrated in Figure 1.1.

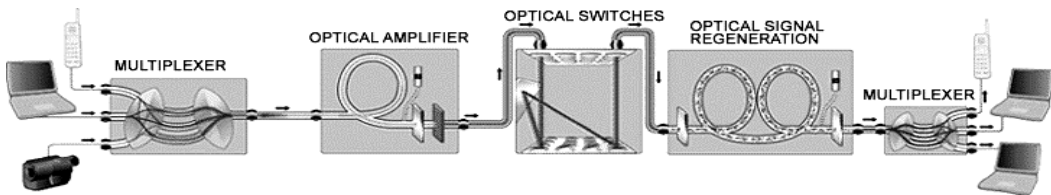


Figure 1.1 Illustration of the concept of Wavelength Division Multiplexing [11].

The chief application advantage of WDM is faster and more copious data transport at relatively little expense compared to installing or replacing fiber-optic cables [9]. This capability is even more advantageous in military aerospace applications where both weight and space must be limited to as great a degree as possible.

The most immediate obstacle to implementing WDM systems is the fact that even though the fiber-optic cabling itself can support multiple wavelengths, the end equipment is usually designed to operate at one wavelength. This can lead to bottlenecks at optical cross connects and does not allow dynamic wavelength hopping depending on cable and load conditions. Furthermore, the fixed wavelength end

equipment causes the need to keep massive inventories of spares because the parts designed for each wavelength are not interchangeable [9].

The solution to this limitation is to use end equipment capable of operating at several wavelengths. If the end equipment can be dynamically programmed to operate at the different wavelengths, network congestion can be mitigated. Furthermore, since all the equipment can be made to operate across the same range, the need for large spare inventories is eliminated [9]. The type of tunable lasers and photodetectors needed to realize dynamic WDM also have applications in “spectroscopy, instrumentation, beam steering, interferometers, and optical interconnects” [9].

1.1.2 Scientific Merit. The characterization of etchants and materials required to realize the structures that enable WDM adds knowledge to the sparsely investigated field of III-V MicroElectroMechanical systems (MEMS). This study benefits the Air Force specifically by characterizing material grown and processed at the Air Force Research Laboratory (AFRL), but will also add to the growing body of knowledge about III-V MEMS. Characterizing this material will benefit future research in III-V MEMS for any purpose, not just the limited scope of mechanically tunable optical devices.

1.2 Brief Background of III-V MEMS

MEMS are finding an increasing number of optical applications, which is creating a separate class of optical MEMS, also known as Micro-Opto-Electro-Mechanical Systems (MOEMS). Although silicon is currently the dominant material for realizing MEMS [8], it has limitations that make other materials (particularly III-V materials) much more suitable for MOEMS [6, 10].

A significant amount of work has taken place in microfabrication using III-V materials [4–7, 12] as discussed in Section 2.3.2. A number of etchants have been characterized with respect to various sacrificial and mechanical layers [6], and novel

etchants have been reported for highly selective removal of gallium arsenide (GaAs) in transistor applications [1]. While MOEMS are becoming more prevalent, there is still further research that must be conducted in order to realize many of the mechanical structures necessary to create useful MOEMS.

1.3 Problem Statement

1.3.1 Accomplishments. The objective of this thesis is to characterize several etchants, sacrificial materials, and mechanical materials with respect to their optical and mechanical properties. All materials consist of $\text{Al}_x\text{Ga}_{1-x}\text{As}$ with x ranging from zero to one. I used the knowledge gained during the characterization process to suggest a basic III-V MEMS fabrication process. The fabrication process is demonstrated by making electrically tunable Fabry-Perot interferometers/filters with several different mechanical structure geometries. I also demonstrate a process for moving active optical devices from one substrate to another, using III-V micromachining techniques.

1.3.2 Uniqueness of Thesis. Although similar to the III-V materials work reported in Section 1.2, my research probes several areas that need to be investigated for the production of a tunable vertical cavity surface emitting laser (VCSEL), as well as for the purpose of fabricating “lift-off VCSELs.” Lift-off VCSELs are optical devices that can be removed from an original substrate and transplanted to a second substrate. My concerns were directed toward how the systems of etchants and sacrificial layers affect the optical properties of the structure left behind. I concerned myself with the flatness of surfaces left behind, as well as the selectivity of the etching methods against material used to make optical devices. I investigated these concerns by performing the various etches and making observations about rate, selectivity, and surface quality using a scanning electron microscope (SEM) with ion milling capability. Furthermore, I used native hydrolyzed aluminum oxide (Al_xO_y)

as a sacrificial layer and controlled the formation of the Al_xO_y sacrificial layer during the oxidation step, which I have not found reported in the literature.

1.4 Thesis Scope and Approach

The aim of this research is to discover what combination of etchants and sacrificial layers produce the most optically useful released III-V mechanical layer. To that end, I used structures made up of several different layers, grown by Molecular Beam Epitaxy (MBE), for my etch study. I performed experiments using the combinations of etchants, sacrificial layers, and mechanical layers listed in Table 1.1. Structures comprising each of the combinations in Table 1.1 are immersed in an excess of etchant after test features have been defined using non-selective reactive ion etching (RIE). By inspecting the results of this etch with an SEM, I determined etch progress and selectivity.

Table 1.1 Combinations of materials and etchants studied.

Sacrificial Material	Mechanical Material	Etchant
GaAs	$\text{Al}_{0.1}\text{Ga}_{0.9}\text{As}:\text{Al}_{0.9}\text{Ga}_{0.1}\text{As}$ Distributed Bragg Reflector (DBR)	$\text{BCl}_3:\text{SF}_6$
GaAs	$\text{Al}_{0.1}\text{Ga}_{0.9}\text{As}$ $\text{Al}_{0.9}\text{Ga}_{0.1}\text{As}$ DBR	Citric Acid ($\text{C}_6\text{H}_8\text{O}_7$): Tripotassium Citrate($\text{K}_3\text{C}_7\text{H}_5\text{O}_2$): Hydrogen Peroxide(H_2O_2): Deionized Water(DIW)
GaAs	$\text{Al}_{0.1}\text{Ga}_{0.9}\text{As}:$ $\text{Al}_{0.9}\text{Ga}_{0.1}\text{As}$ DBR	$\text{C}_6\text{H}_8\text{O}_7:$ $\text{K}_3\text{C}_7\text{H}_5\text{O}_2:$ $\text{H}_2\text{O}_2:$ DIW
AlAs	$\text{Al}_{0.1}\text{Ga}_{0.9}\text{As}:$ $\text{Al}_{0.9}\text{Ga}_{0.1}\text{As}$ DBR	Hydrofluoric Acid (HF): DIW
AlAs	$\text{Al}_{0.1}\text{Ga}_{0.9}\text{As}:$ $\text{Al}_{0.9}\text{Ga}_{0.1}\text{As}$ DBR	HF:Isopropyl Alcohol(ISP): DIW
$\text{AlAs} \Rightarrow \text{Al}_x\text{O}_y$	$\text{Al}_{0.9}\text{Ga}_{0.1}\text{As}$	Potassium Hydroxide (KOH):DIW

Based on the results of this etch study, I explored the application of surface micromachining using the materials listed in Table 1.1. The concept of surface micromaching is discussed further in Section 2.2.1 and illustrated in Figure 2.2. I patterned a simple anchored cantilever structure made of a DBR and released it using the etchant determined to be most suitable. The power reflectance across a range of wavelengths of the resulting Fabry-Perot interferometer was then measured before and after release as well as when actuated to produce tuning.

I further demonstrated the utility of the $\text{AlAs} \Rightarrow \text{Al}_x\text{O}_y$ release process by releasing functional resonant cavity light emitting diodes (RCLEDs). These RCLEDs were suspended in the etching fluid and allowed to land on an acceptor substrate so that they could be tested.

1.5 Main Results

I have characterized the etch rate for GaAs being removed with $\text{C}_6\text{H}_8\text{O}_7:\text{K}_3\text{C}_7\text{H}_5\text{O}_2:\text{H}_2\text{O}_2$ for a $1.5 \mu\text{m}$ thick sacrificial layer. I also characterize selectivity relative to the special case of thin, alternating layers of $\text{Al}_{0.1}\text{Ga}_{0.9}\text{As}$ and $\text{Al}_{0.9}\text{Ga}_{0.1}\text{As}$.

I characterize oxidation rate for a 329 nm thick AlAs sacrificial layer as well as selectivity relative to a DBR consisting of alternating layers of $\text{Al}_{0.1}\text{Ga}_{0.9}\text{As}$ and $\text{Al}_{0.9}\text{Ga}_{0.1}\text{As}$. I also confirm the usefulness of removing Al_xO_y with a KOH solution.

I demonstrate the ability to release MEMS structures using both of these etching schemes. I also demonstrate the ability to release an active optical device from its substrate and transplant it to another substrate using oxidation followed by oxide removal without significant degradation of its ability to emit light.

1.6 Thesis Overview

In Chapter II, I review current reported progress in III-V MEMS, as well as provide background information on the principles of the structures I fabricate and the

methods of processing. In Chapter III, I detail the experiments performed. Chapter IV contains the results of my experiments along with a brief analysis of my results. Chapter V contains conclusions drawn from the entire research, a summary of my contributions, and suggestions for future research in this area. References used in each chapter are cataloged at the end of that chapter.

Bibliography

1. Chang, H.-C., Chang, E. Y., Chung, C.-C., and Kuo, C. T. “Highly Selective GaAs/Al_{0.2}Ga_{0.8}As Wet Etch Process for the Gate Recess of Low-Voltage-Power Pseudomorphic High-Electron-Mobility Transistor,” *Japanese Journal of Applied Physics, Part 1*, 39(8):4699–4703 (2000).
2. Dunlap, O. E. *Marconi: The Man and His Wireless*. New York: The MacMillan Company, 1937.
3. Gunston, D. *Marconi: Father of Radio*. New York: Crowell-Collier Press, 1965.
4. Hjort, K. “Micromachining in Bulk GaAs,” *Sensors and Materials*, 2(1):1–5 (1990).
5. Hjort, K. “Gallium Arsenide as a Mechanical Material,” *Journal of Micromechanics and Microengineering*, 4(1):1–13 (March 1994).
6. Hjort, K. “Sacrificial Etching of III–V Compounds for Micromechanical Devices,” *Journal of Micromechanics and Microengineering*, 6(4):370–375 (December 1996).
7. Hjort, K., Schweitz, J.-Å., and Hök, B. “Bulk and Surface Mircromachining of GaAs Structures,” *Proceedings of the Annual International Workshop on Micro-Electro-Mechanical Systems*. Napa Valley, California, February 1990.
8. Kovacs, G. T. A. *Micromachined Transducers Sourcebook*. Boston: McGraw-Hill, 1998.
9. Ochoa, E. M. *Microelectromechanically-Tunable Vertical Cavity Surface Emitting Lasers*. Dissertation Prospectus, Air Force Institute of Technology, Wright-Patterson Air Force Base, OH, August 2001. Unpublished.
10. Saleh, B. E. A. and Teich, M. C. *Fundamentals of Photonics*. Wiley Series in Pure and Applied Optics, New York: John Wiley & Sons, Inc., 1991.
11. Stix, G. “The Triumph of the Light,” *Scientific American* (January 2001).
12. Uenishi, Y., Tanaka, H., and Ukita, H. “Characterization of AlGaAs Microstructure Fabricated by AlGaAs/GaAs Micromachining,” *IEEE Transactions on Electron Devices*, 41(10):1778–1783 (October 1994).
13. United States Department of Defense. *Joint Vision 2010*. June 2000. <http://www.dtic.mil/jv2010/jvpub.htm>.

II. Background

2.1 Introduction

Since the overarching focus of my work is the integration of microelectromechanical systems (MEMS) and optical devices, there are a variety of topics covered in this chapter. The background begins with a discussion of MEMS fabrication techniques, actuation schemes, material trade-offs, and current research in III-V MEMS (Section 2.2, Section 2.3). Methods of growing III-V materials are detailed next (Section 2.4). A discussion of basic microelectronic processing techniques including photolithography (Section 2.5), metal deposition (Section 2.6), etching (Section 2.7) and oxidation (Section 2.8) is included next. A discussion on MEMS structure release ties the discussion of processing together with the discussion of MEMS (Section 2.9). The optical principles behind the operation of my devices are detailed in Section 2.10. Finally, I give a brief explanation of the technique used to make device actuation measurements and surface flatness determinations.

2.2 Microelectromechanical Systems

The basic concept behind MEMS is that advantages with respect to the speed, durability, volume, weight and cost can be gained by making devices extremely small. In general, MEMS are fabricated using micromachining techniques that were originally developed for microelectronic devices and integrated circuits (ICs) [28].

2.2.1 Fabrication and Processing. For all types of MEMS, there are three methods of micromachining: bulk, surface, and microforming. Bulk and surface micromachining are most common, and are commonly used in concert when the designer deems it advantageous. Bulk micromachining is basically a subtractive process—it is used to remove large amounts of substrate material. This technique is useful for creating membranes, holes and trenches, or for undercutting structures that

will need to move [29]. “Surface micromachining is characterized by the fabrication of micromechanical structures from deposited thin films” [6]. Surface micromachining is used to form structures above the substrate similar to those obtained by bulk micromachining, and offers the advantage of greater compatibility with device and IC processing techniques [6]. These terms are applicable regardless of the type of material or exact processing method used. Figure 2.1 shows examples of the two types of micromachining.

TYPES OF MICROMACHINING

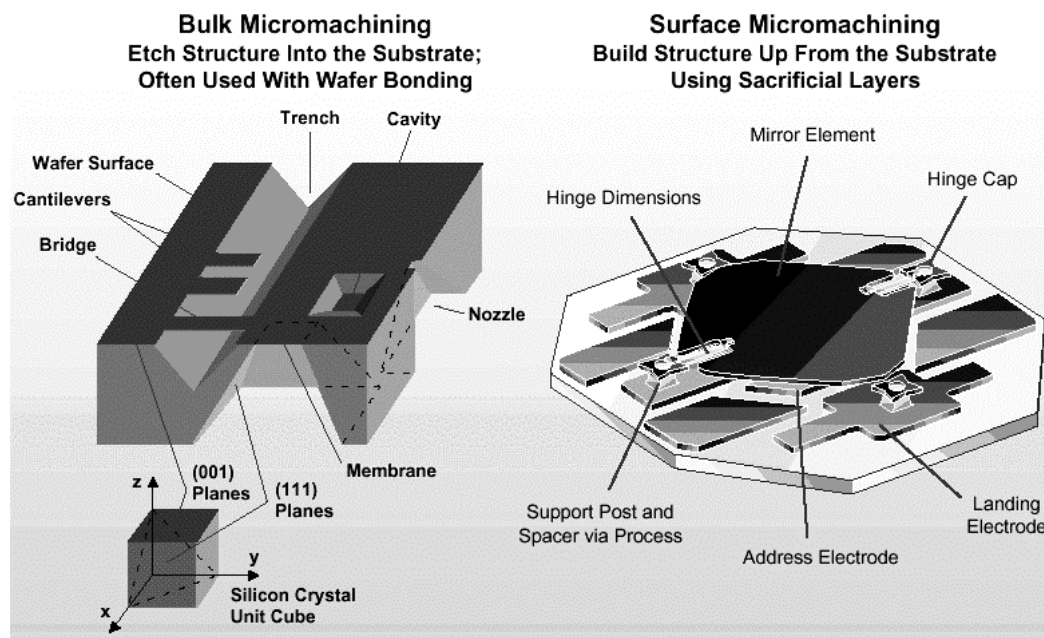


Figure 2.1 Similarities and differences between bulk and surface micromachining [36].

For most types of micromachining, additional material must be added above the substrate. This material can be a continuation of the substrate crystal (epitaxial growth is discussed further in Section 2.4), a deposited polycrystalline form of the substrate, an amorphous dielectric, a metal, a ceramic material, or an organic material [28]. Patterning of these layers to form useful structures can occur by either

selectively etching materials that are in place or selectively depositing materials. An example of the process I use to realize cantilever structures is depicted in Figure 2.2, which includes and clarifies the steps involved in surface micromachining as applied to my work.

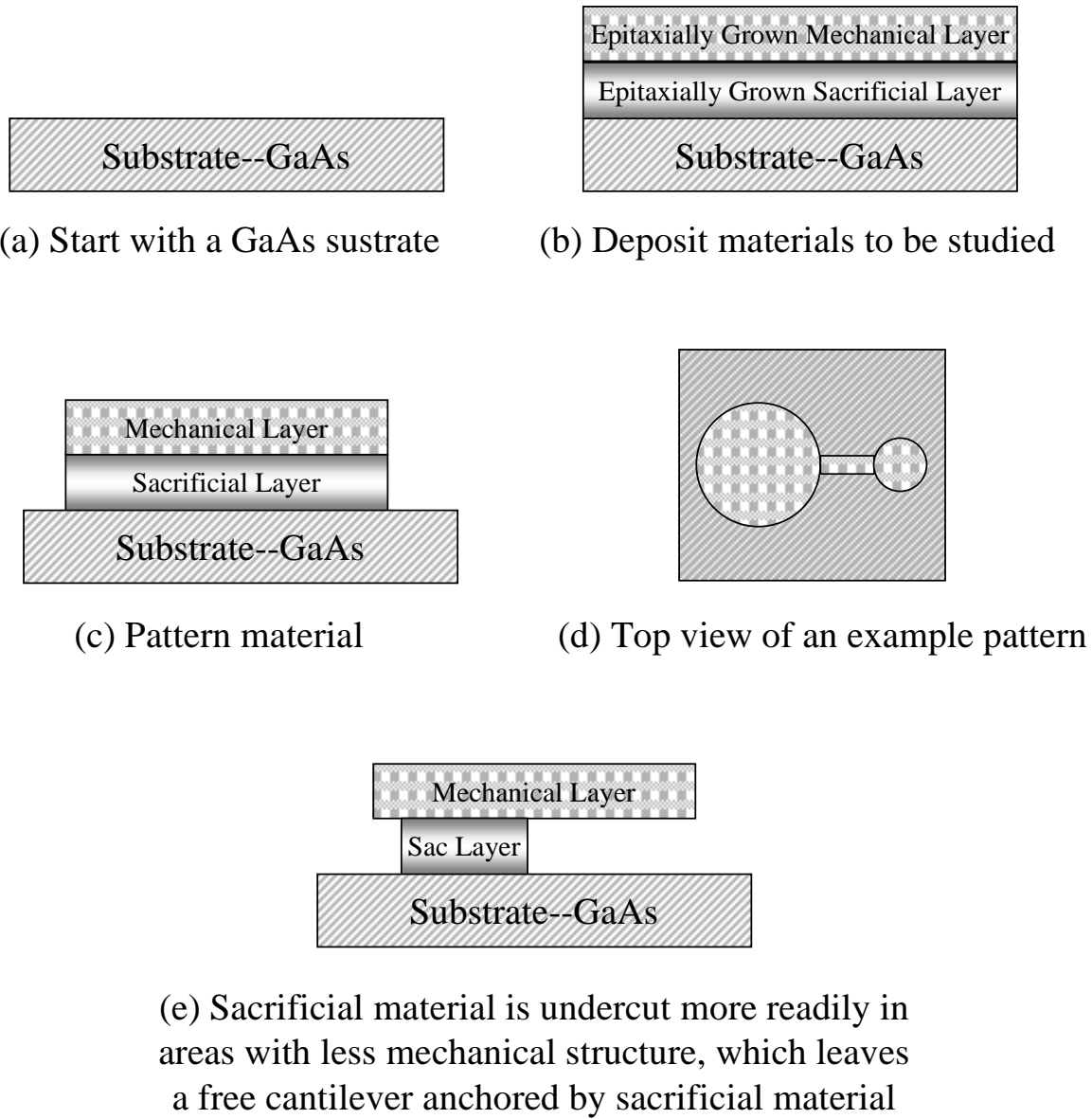


Figure 2.2 Surface micromachining process used in my work.

The processing steps I use to perform micromachining include photolithography, etching, wet oxidation of aluminum arsenide (AlAs), and material deposition: all of which are discussed within this chapter.

2.2.2 Electrostatic Actuation. Once devices have been fabricated and processed, a great deal more utility can be gained if the devices can be purposefully moved. Current MEMS actuation and assembly mechanisms include electrostatic, thermal, electromagnetic, residual stress, pneumatic, shape memory alloy, magnetoresistive, thermodynamic, and piezoelectric [25]. For the structures I have fabricated, electrostatic actuation is the most practical scheme. With electrostatic actuation, the actuator need only move itself [28], which is most practical for applications that only endeavor to manipulate light.

Benjamin Franklin discovered the basic principle behind electrostatic actuation: two oppositely charged plates exert an attractive force on one another [28]. Figure 2.3 shows the side view of a cantilever wherein the flexible top plate is attracted to a stationary substrate by a difference in applied voltage.

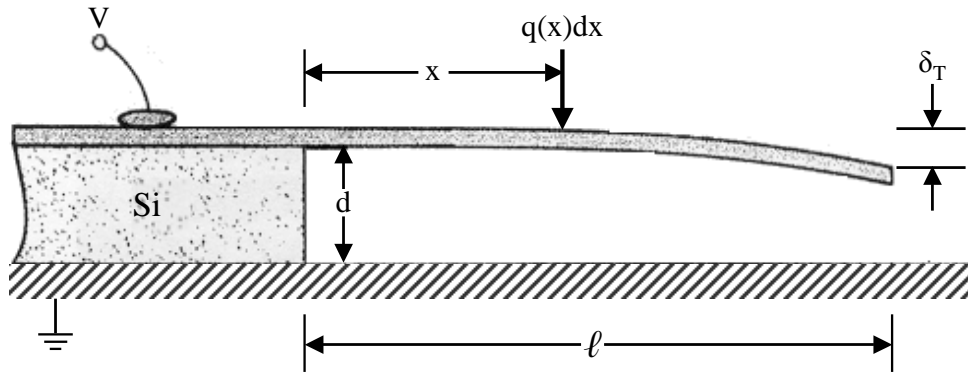


Figure 2.3 Electrostatic actuation of a micromachined cantilever [44].

The equations governing operation of electrostatically actuated cantilevers start with the equation describing the deflection at the tip of a cantilever caused by a concentrated load at a position x units away from its fixed end [44]:

$$(d\delta)_T = \frac{x^2}{6EI} (3\ell - x) w q(x) dx \quad (nm) \quad (2.1)$$

where

- $(d\delta)_T$ = Differential deflection at the tip of the cantilever
- x = Distance of load from fixed end
- E = Young's modulus: a material constant proportional to stiffness that is derived from measurements of stress divided by strain [28]
- I = Cantilever moment of inertia
- ℓ = Beam length
- w = Width of the cantilever
- $q(x)$ = Electrostatic force at a point x away from the fixed end

Since the electrostatic force is present along the entire length of the beam, the following integral describes the total deflection at the tip of the cantilever [44]:

$$\delta_T = w \int_0^\ell \frac{(3\ell - x)}{6EI} x^2 q(x) dx \quad (nm) \quad (2.2)$$

where the electrostatic force at a point x distance away from the fixed end of the cantilever, $q(x)$, is defined by:

$$q(x) = \frac{\epsilon_0}{2} \left(\frac{V}{d - \delta(x)} \right)^2 \quad (Newtons) \quad (2.3)$$

where

- ϵ_0 = Permittivity of free space
- V = Potential difference between the cantilever and substrate
- d = Original distance between the cantilever and substrate
- $\delta(x)$ = Deflection at a point x nm away from the fixed end of the cantilever

Because of reasonable agreement with experimental measurements, deflection at a given point is approximated by square-law curvature, as shown in Equation 2.4 [44]:

$$\delta(x) \simeq \left(\frac{x}{\ell} \right)^2 \delta_T \quad (nm) \quad (2.4)$$

By substituting Equation 2.3 and Equation 2.4 into Equation 2.2 and solving for the normalized load (\mathcal{L}) [44]:

$$\mathcal{L} = \frac{\epsilon_0 w \ell^4 V^2}{2 E I d^3} \quad (\text{Dimensionless}) \quad (2.5)$$

The normalized load may be couched in terms of normalized tip deflection, $\Delta = (\delta_T/d)$, and thus [44]:

$$\mathcal{L} = 4\Delta^2 \left(\frac{2}{3(1-\Delta)} - \frac{\tanh^{-1} \sqrt{\Delta}}{\sqrt{\Delta}} - \frac{\ln(1-\Delta)}{3\Delta} \right)^{-1} \quad (\text{Dimensionless}) \quad (2.6)$$

By setting Equation 2.5 equal to Equation 2.7 and solving numerically I find the expected deflection for a given applied voltage, if sufficient data is available concerning the material properties of the constituent layers.

$$\frac{\epsilon_0 w \ell^4 V^2}{2 E I d^3} = 4\Delta^2 \left(\frac{2}{3(1-\Delta)} - \frac{\tanh^{-1} \sqrt{\Delta}}{\sqrt{\Delta}} - \frac{\ln(1-\Delta)}{3\Delta} \right)^{-1} \quad (\text{Dimensionless}) \quad (2.7)$$

The advantages associated with electrostatic actuation of cantilevers are ease of fabrication and low power consumption [28], but there are also challenges associated with using this technique. Electrostatic actuation is non-linear because the attractive force between the two plates is inversely proportional to the square of the distance between them, as given by Coulomb's Law:

$$F_{elec} = \frac{1}{4\pi\epsilon_r\epsilon_0} \cdot \frac{q_1 q_2}{x^2} \quad (\text{Newtons}) \quad (2.8)$$

where

- ϵ_r = Relative permittivity
- q_1, q_2 = Charge on surface 1,2
- x = Distance between the two surfaces

An increasing force with decreasing distance leads to the phenomenon of “snap through.” When sufficient voltage is applied to the structure to move the cantilever flexure approximately 1/3 of the distance from its original horizontal resting position toward the substrate, the attractive electrostatic force overwhelms the restoring mechanical force and the cantilever deflects all the way to the substrate [44]. For cantilevers the threshold voltage at which the stick down phenomenon occurs is estimated as [44]

$$V_{th} \simeq \sqrt{\frac{18EI d^3}{5\epsilon_0 \ell^4 w}} \quad (\text{Volts}) \quad (2.9)$$

This non-linear behavior including the occurrence of snap through is illustrated in Figure 2.4, where a graph of Equation 2.7 is given along with experimental data collected during electrostatic actuation of a cantilever structure [44]. Stick down is shown as the horizontal line, which indicates that no additional loading is required to cause complete deflection ($\Delta = 1$).

A second challenge to electrostatic actuation is the fact that the stick down behavior is not always predictable. Fringing fields, surface leakage, and conduction through the spacing layer between the cantilever flexure and the substrate can lead to discrepancies between actual and theoretical values for efficiency and actuation voltage [28].

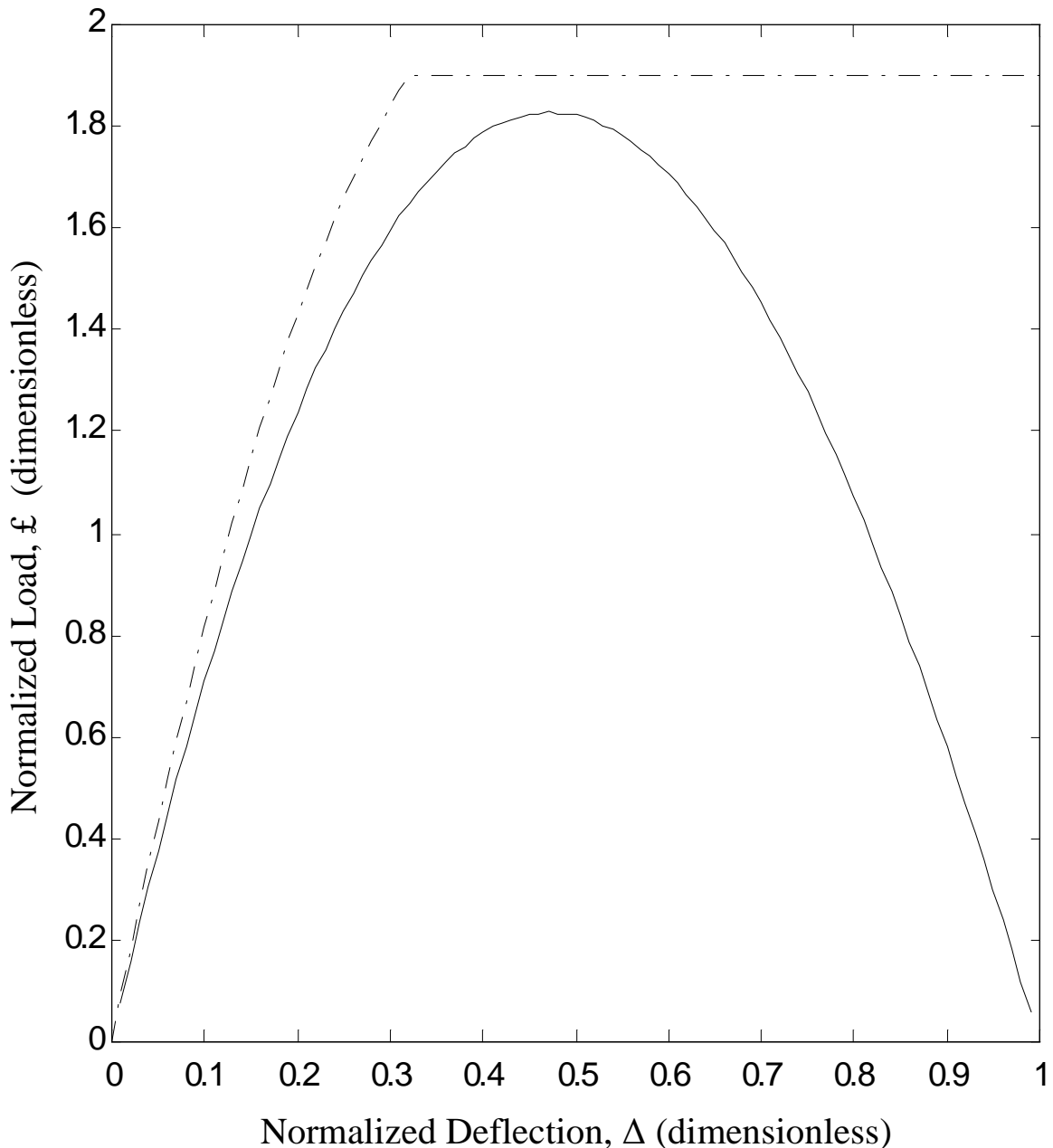


Figure 2.4 Plot of the relationship between normalized load and normalized deflection as given by Equation 2.7 (solid line) and curve fit to actual deflection versus load data gathered by Petersen [44] (dashed line). The abrupt horizontal line indicates sudden, complete deflection of the cantilever at approximately one third the original distance between the cantilever and the substrate ($\Delta = 0.33$).

2.3 MEMS Materials

2.3.1 Silicon. Silicon is the most commonly used material for microfabrication. This is due largely to economic considerations. Silicon compounds comprise 25 percent of the earth's crust, and it is second only to oxygen in natural abundance. Silicon is the least expensive of the semiconductor materials [48]. Furthermore, silicon and silicon dioxide(SiO_2) processing techniques are highly developed [28]. Finally, single crystal silicon is one of the strongest semiconductors commonly available [35] with the possible exceptions of diamond and silicon carbide SiC [26]. Additionally, Silicon forms a stable oxide that has been used with great success as an insulator in semiconductor manufacturing [48].

2.3.1.1 Single Crystal Silicon. There are several advantages to micromachining with monocrystalline silicon. Chiefly, crystal plane selectivity of etchants can be exploited to fabricate structures with three-dimensional characteristics that are difficult to achieve with amorphous material [28]. This is most important for bulk micromachining.

2.3.1.2 Polycrystalline Silicon. For surface micromachining with silicon, some of the advantages of micromachining with epitaxial regrowth can be achieved without the processing difficulties cited in Section 2.4.2 by depositing polycrystalline silicon for use as a mechanical layer. This is commonly practiced in the Multi-User MEMS Process (MUMPs[®]) [26]. Figure 2.5 shows an example of a structure fabricated and released using the MUMPs[®] process. The effect of the patterned sacrificial layers is clear in that the first polysilicon mechanical layer (Poly1) has been anchored to the silicon nitride (SiN) just above the substrate and mechanical structures have been released in other areas. Sacrificial layer patterning also allows the Poly2 mechanical layer to be anchored to the Poly1 mechanical layer or to the Poly0 mechanical layer as shown in Figure 2.5.

2.3.1.3 Applications of Silicon MEMS. Many devices have been fabricated using MUMPs® or similar processes and a variety of applications have been found for silicon MEMS. These include passive microchannels and tubes to direct fluids, sensors detecting infrared radiation, pressure, or acceleration, actuators that move only themselves or other tiny components, and integrated MEMS-based sensor systems that can detect their environment and take action on the basis of what they detect [39].

2.3.1.4 Limitations of Silicon MEMS. Notably absent from the list of applications for silicon MEMS is any function that involves the generation of light in the visible portion of the electromagnetic spectrum. The reason for this limitation is that silicon does not have a direct band gap. A change in crystal momentum is required for electrons to move between the top of the valence band and the bottom of the conduction band, and indirect band gap materials do not emit light efficiently [45]. Additionally, silicon's relatively small band gap causes it to absorb electromagnetic radiation with wavelengths shorter than about $1.1\text{ }\mu\text{m}$ [19]. These limitations are important as they are a primary justification for my research using $\text{Al}_x\text{Ga}_{1-x}\text{As}$ compounds.

2.3.2 $\text{Al}_x\text{Ga}_{1-x}\text{As}$ MEMS.

2.3.2.1 Comparison to Silicon MEMS. Most III-V MEMS are lattice matched to GaAs or InP. This allows for heteroepitaxy with very little strain on the material [19], which means that a single crystal structure can be grown with regions of differing materials. This enables applications where a crystalline structure is required on top of a sacrificial layer.

Many structures that have been micromachined in silicon have been replicated in $\text{Al}_x\text{Ga}_{1-x}\text{As}$ and most of the same structures are possible [18,20] although dimensions may differ. Two of these structures are shown in Figure 2.6.

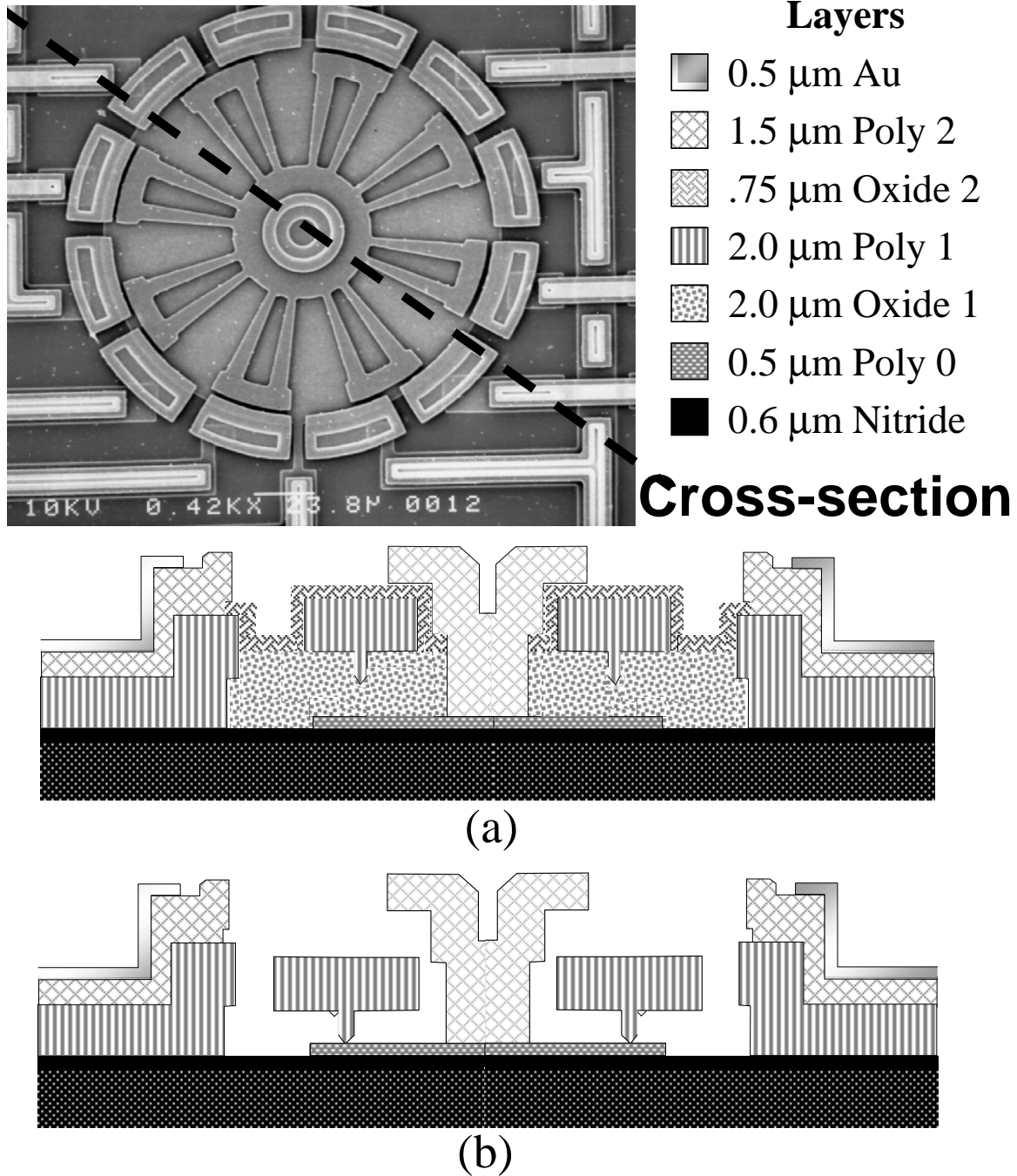
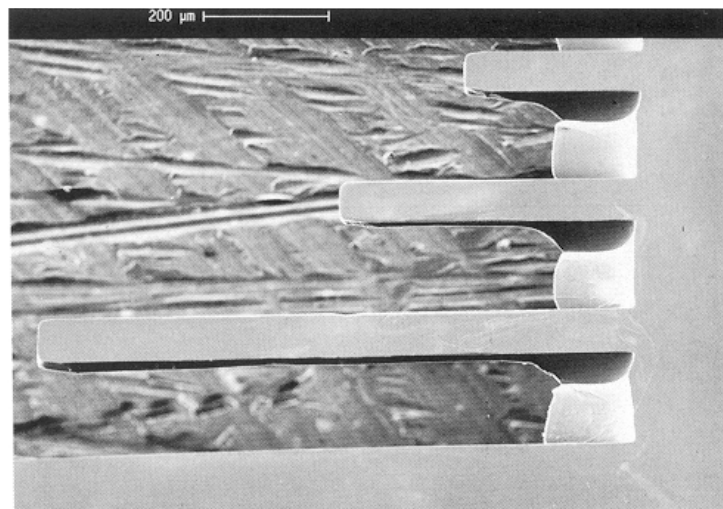
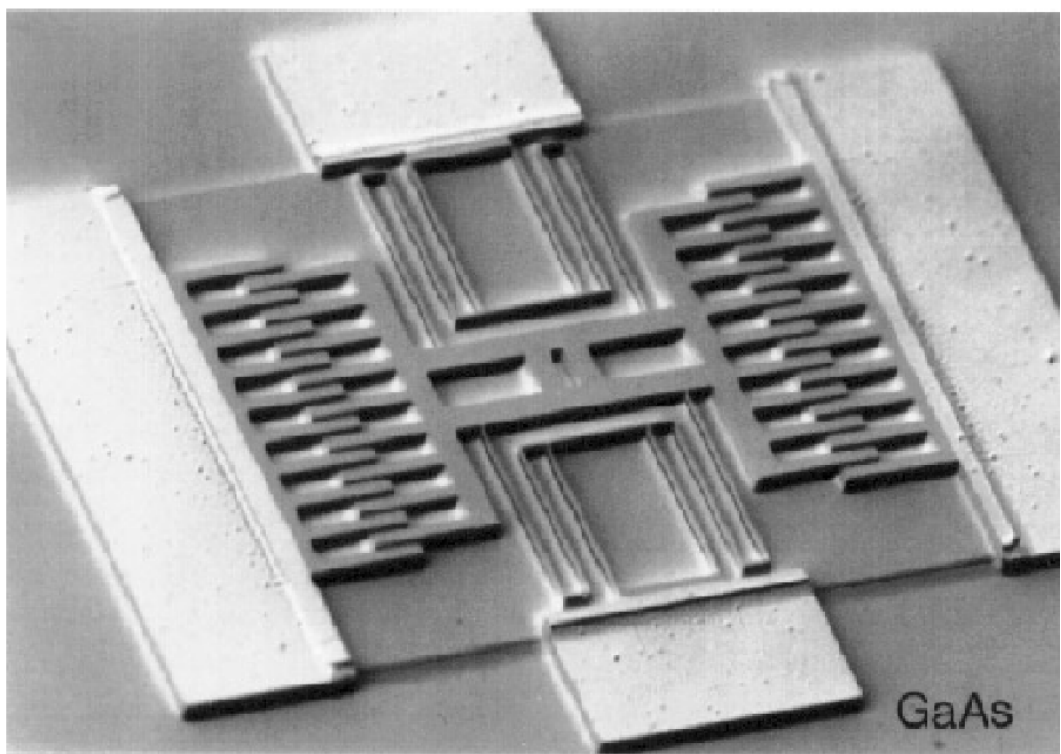


Figure 2.5 Circular micromotor structure fabricated using MUMPs® before (a) and after (b) removal of the sacrificial layers [43].



(a)



(b)

Figure 2.6 Structures fabricated from $\text{Al}_x\text{Ga}_{1-x}\text{As}$ compounds: (a) cantilevers formed by bulk micromachining [17], and (b) a comb resonator made using surface micromachining with epitaxial regrowth [19]

Table 2.1 reports some factors and properties concerning silicon and gallium arsenide. The difference of greatest importance to my work is the direct band gap present in GaAs, which allows it to be an efficient emitter of photons. Furthermore, GaAs has a band gap corresponding to infrared radiation near 870 nm, which allows it to interact with shorter wavelength radiation than Si without absorbing [45].

Table 2.1 Comparison of properties of Si and GaAs for micromachining [35].

Property	GaAs	Si
Speed	+	-
Heterostructures	Many	SiGe
Opto-electronics	+	-
Piezo effect	Yes	No
Thermal Conductivity	Relatively low	Relatively high
Integration density	+	++
Cost	High	Low
Bonding to other substrates	Difficult	Relatively easy
Fracture	Brittle, fragile	Brittle, strong
Operation temperature	High	Low
Bandgap (eV)	1.424	1.12
Bandgap Transition	Direct	Indirect
Physical Stability	Fair: sublimation of arsenic is a problem	Very good
Etching behavior	Isotropic/anisotropic	Isotropic/anisotropic

The most important limitation to the use of III-V materials is the fact that they are at least 10 times more expensive than silicon [19]. Even advocates of III-V MEMS concede that it should only be used when it “offers properties that silicon lacks” [18].

2.3.2.2 Work to Date in III-V MEMS. As mentioned previously, a number of MEMS have been fabricated in III-V materials. Many systems of etchants and sacrificial layers have also been characterized [19]. The use of GaAs as a sacrificial layer has also been reported [50], although the etching selectivity of GaAs to

$\text{Al}_{0.4}\text{Ga}_{0.6}\text{As}$ reported is only listed as $> 100 : 1$ [19]. Another etchant, tripotassium citrate, has been reported for the highly selective removal of GaAs in transistor manufacture, but the etchant's ability to selectively etch GaAs has only been reported against $\text{Al}_{0.2}\text{Ga}_{0.8}\text{As}$ with a selectivity of 3400:1 [7].

2.4 Molecular Beam Epitaxy for Aluminum Gallium Arsenide

2.4.1 Growth by Molecular Beam Epitaxy. Epitaxial processes use a substrate as a seed crystal and continue single-crystal growth in additional layers. These layers can be the same material as the substrate or a different material with a similar lattice constant [48]. Molecular beam epitaxy (MBE) occurs in a vacuum with pressure ranging from 10^{-8} to 10^{-6} Torr. The great advantage of MBE over other methods of epitaxial growth is that the grower has the ability to precisely control material composition, doping profile, and layer thickness [48]. MBE is carried out in a chamber like the one illustrated in Figure 2.7.

During the growth process, the single-crystal substrate is heated to between 400 °C and 800 °C [35]. The effusion ovens as they are labelled in Figure 2.7 are held at a constant temperature. This temperature determines the flux of atoms or molecules that are emitted by sublimation toward the substrate [43]. In the case of $\text{Al}_x\text{Ga}_{1-x}\text{As}$ epitaxial layers, the growth takes place in an overpressure of As_2 or As_4 since arsenic will sublime away from the growth surface unless a layer of column III atoms is present. This process is also true to a lesser degree in reverse: column III atoms will not remain in the crystal unless there is sufficient arsenic. Hence the growth rate is governed by the flux of the column III elements—gallium and aluminum [48]. The relative composition of the material can be controlled in an analog manner, where the flux of each element, and therefore the final $\text{Al}_x\text{Ga}_{1-x}\text{As}$ composition, is controlled via the temperature of individual effusion ovens. There also exists the possibility of creating a digital alloy by alternately growing layers of two distinct materials with proportional thicknesses on the order of several monolayers [15].

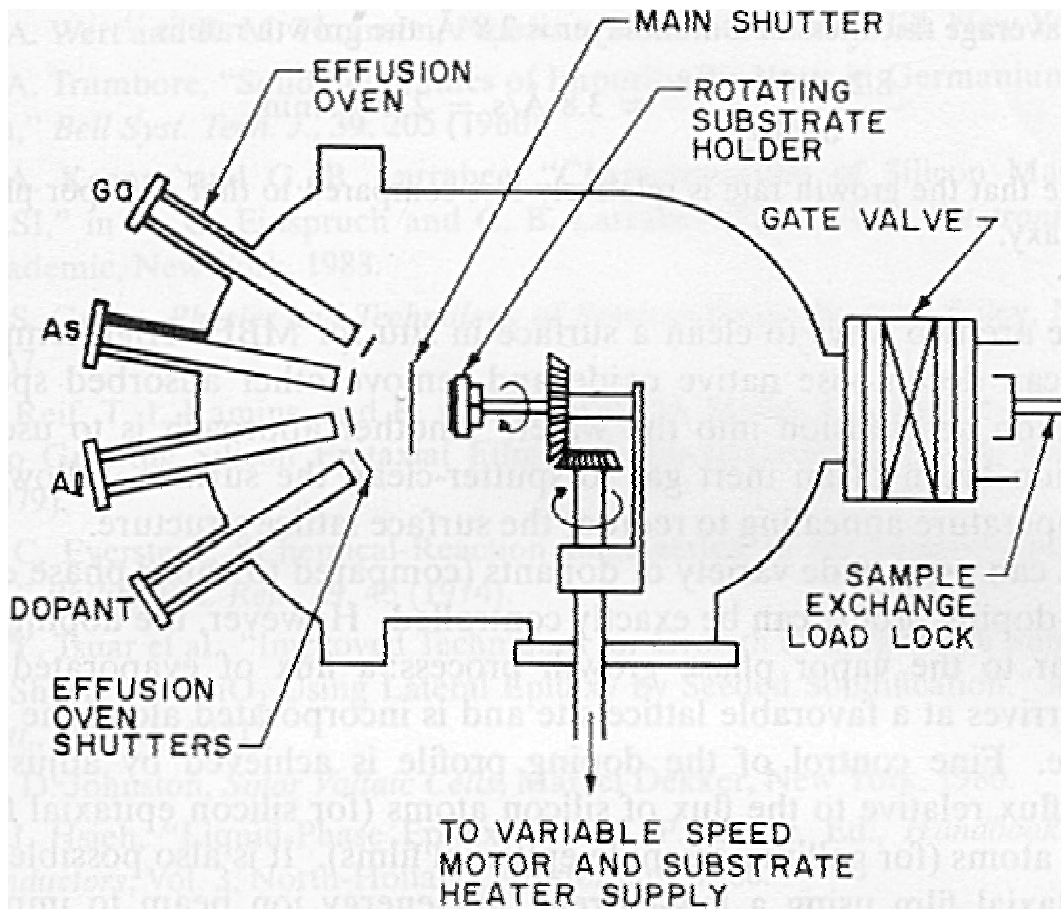


Figure 2.7 Diagram of a solid source molecular beam epitaxy system [48].

Typically, the substrate is rotated during growth to ensure uniformity of layer thickness, composition, and dopant distribution [43]. However, to ensure that one area of the wafer contains structures of exactly the designed layer thickness, there is a technique documented where the substrate is purposely not rotated [34]. All samples grown for my thesis were rotated during growth.

2.4.2 Regrowth with MBE. Epitaxial regrowth is the process of depositing one or more epitaxial layers, patterning, and selectively etching one or more of these layers away, and then continuing epitaxial growth. The regrowth technique allows surface micromachining to result in structures that are anchored to the substrate

directly, not via a sacrificial layer [19]. Figure 2.8 contrasts processing using regrowth with processing that depends on a single crystal growth step.

The advantages of utilizing regrowth are the use of a crystalline mechanical material as an anchor and reduced dependence on timing for the release etch—none of the sacrificial layer has to be left behind. If the crystalline mechanical layer is used as the anchor then the structure has a more predictable shape. The reduced dependence on timing makes the micromachining process more robust. Another advantage is that the sample can be exposed to the etchant longer. This overetch is helpful in removing stringers [49]. Stringers are threads of material unintentionally left behind after an etching step. Stringers cause otherwise free standing structures to remain stuck together or supported unintentionally.

Given the advantages of using epitaxial regrowth, the question arises as to the difficulties associated with using this technology for III-V MEMS. The nature of the problems that prohibit regrowth deal mainly with the condition of the material’s surface [36]. Surfaces are inevitably damaged during etching and oxidized when removed from the ultra-high vacuum environment of the MBE growth chamber [51]. Oxidation leaves an amorphous film which causes polycrystalline deposition in subsequent layers and acts as a deep acceptor, raising the resistivity of the deposited film [51]. Polycrystalline material is also unsuited for many optical applications since the resulting grain boundaries act as centers for non-radiative recombination, thus inducing absorption [32]. Oxidation is removed by heating the substrate beyond the growth temperature after it is returned to the vacuum chamber [22] or by cleaning the surface with hydrogen radicals [4, 5]. Structural defects and impurities introduced due to etching, however, are not easily removed and result in crystal defects that propagate to all subsequent epitaxial layers [51]. Specialized in situ etching can provide relief from some of these problems [12, 38], but these capabilities are not currently available in the facilities where I accomplished my work. Thus, I will not report on epitaxially regrown MEMS in this thesis.

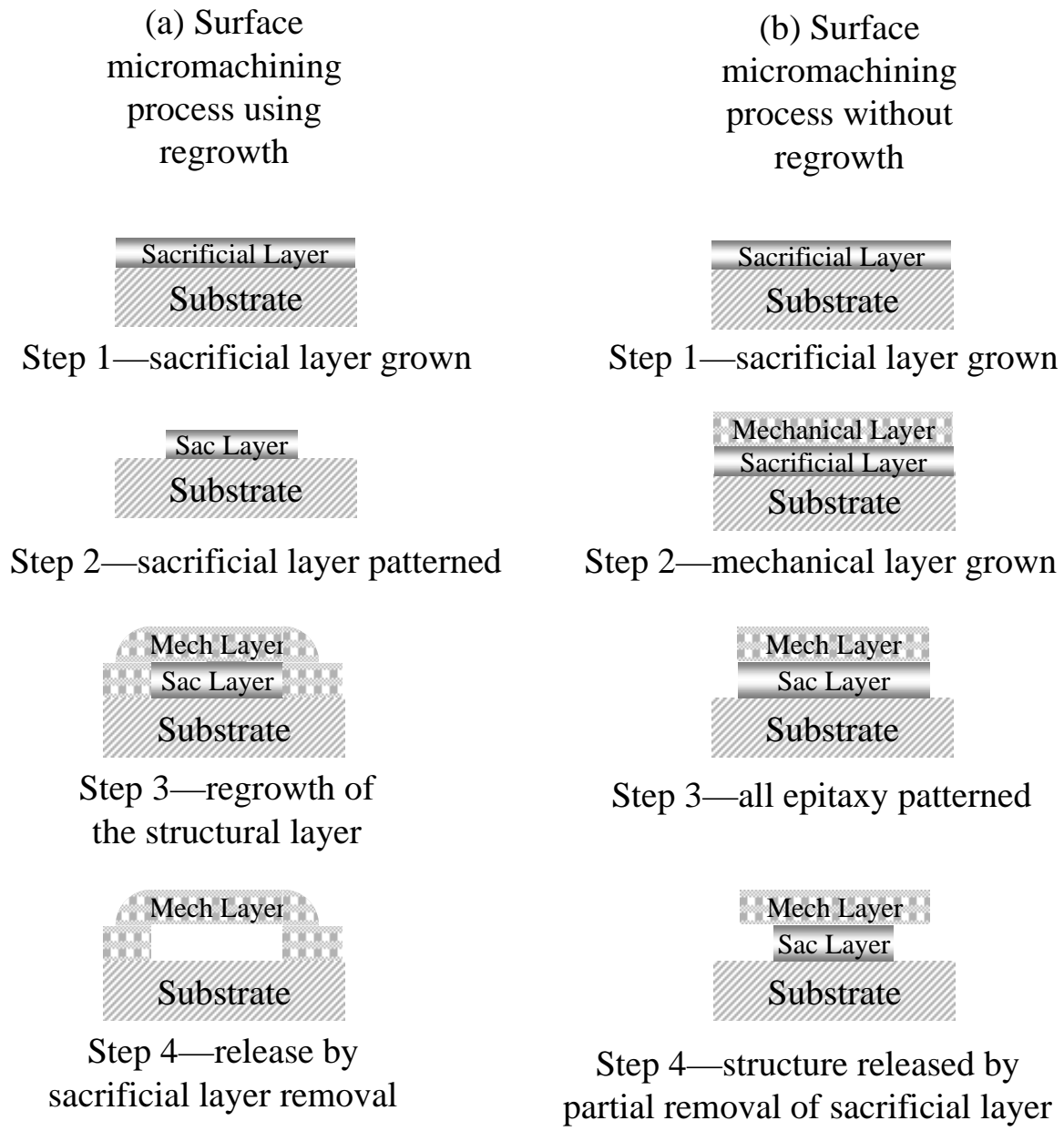


Figure 2.8 Comparison and contrast between structures fabricated (a)with, and (b)without epitaxial regrowth.

2.5 Photolithography

The photolithography process consists of coating a wafer with photoresist, exposing the photoresist to ultraviolet (UV) radiation through a contact mask, and then developing the photoresist so that either the exposed photoresist, if positive, or unexposed photoresist, if negative, is washed away. The behavior of photoresist is dependent on environmental factors such as temperature and humidity as well as exposure to ambient light. To minimize undesired affects from fluctuations in temperature and humidity, the environmental controls on the clean room where lithography occurs are held within narrow tolerances. In the clean room facility used, the temperature is held within a few degrees of 68 °F and the humidity is maintained very close to 40 percent. Records of the actual temperature and humidity are maintained so that they can be checked if a process yields unexpected results. To minimize the effect of exposure to ambient light, the clean room is lighted with special bulbs in which the shorter wavelengths, to which the photoresist is most sensitive, have been filtered out. Additionally, wafers that are not being processed are stored in a lithography dry box and photoresist that has been on a wafer for more than 24 hours is not used in further lithography steps.

The control variables associated with lithography include type of photoresist, length, intensity and wavelength of exposure, length of developing, and thickness of the photoresist, which is dictated by spin speed when the photoresist is applied. These factors are detailed when I report the methodology for each experiment. In general, I relied on the experience of others and used known lithography recipes. Alteration of these parameters is not part of my investigation, so I report only photolithography procedures used to fabricate the structures needed for my experiments.

2.6 Metal Deposition

For efficient electrical actuation of devices, an ohmic contact to the semiconductor should be put in place, so that a probe can later be used for actuation. The

method of metal deposition used in my work is electron beam (e-beam) metallization. This method operates by directing an intense beam of electrons into a crucible filled with a metal, all under high vacuum ($\sim 10^{-6}$ Torr). The metal slowly evaporates and coats the sample [37]. The most notable advantages of e-beam metallization are the low contamination levels achieved and the speed of the process [37]. The majority of the time required is spent drawing the necessary vacuum.

Although gold (Au) contacts have many desirable properties, the low reactivity of gold keeps it from adhering to the surface of the semiconductor. The solution to this problem is the placement of a thin adhesion layer composed of titanium (Ti) [28]. For the structures used in my research, the standard contact is composed of 200 Å Ti followed by 2550 Å Au. Unless noted, this is the standard ohmic contact I used.

To pattern the metal, two layers of photoresist are laid out. Their cumulative thickness is approximately 800 nm. The metal is deposited over the entire sample and the metal atop the photoresist is removed using cellophane tape or pressurized acetone. An example of a finished metallization process is shown in Figure 2.9.

One concern with any metallization process for ohmic contacts is the inadvertent formation of a Schottky barrier. Two methods to ensure creation of an ohmic contact are to highly dope the material near the metal contact [41] and to perform thermal annealing after the metal is in place [10]. A contact composed of Ti and Au will form a Schottky barrier, but the highly doped material next to the metal allows tunneling, which makes the contact behave as though it were ohmic [32].

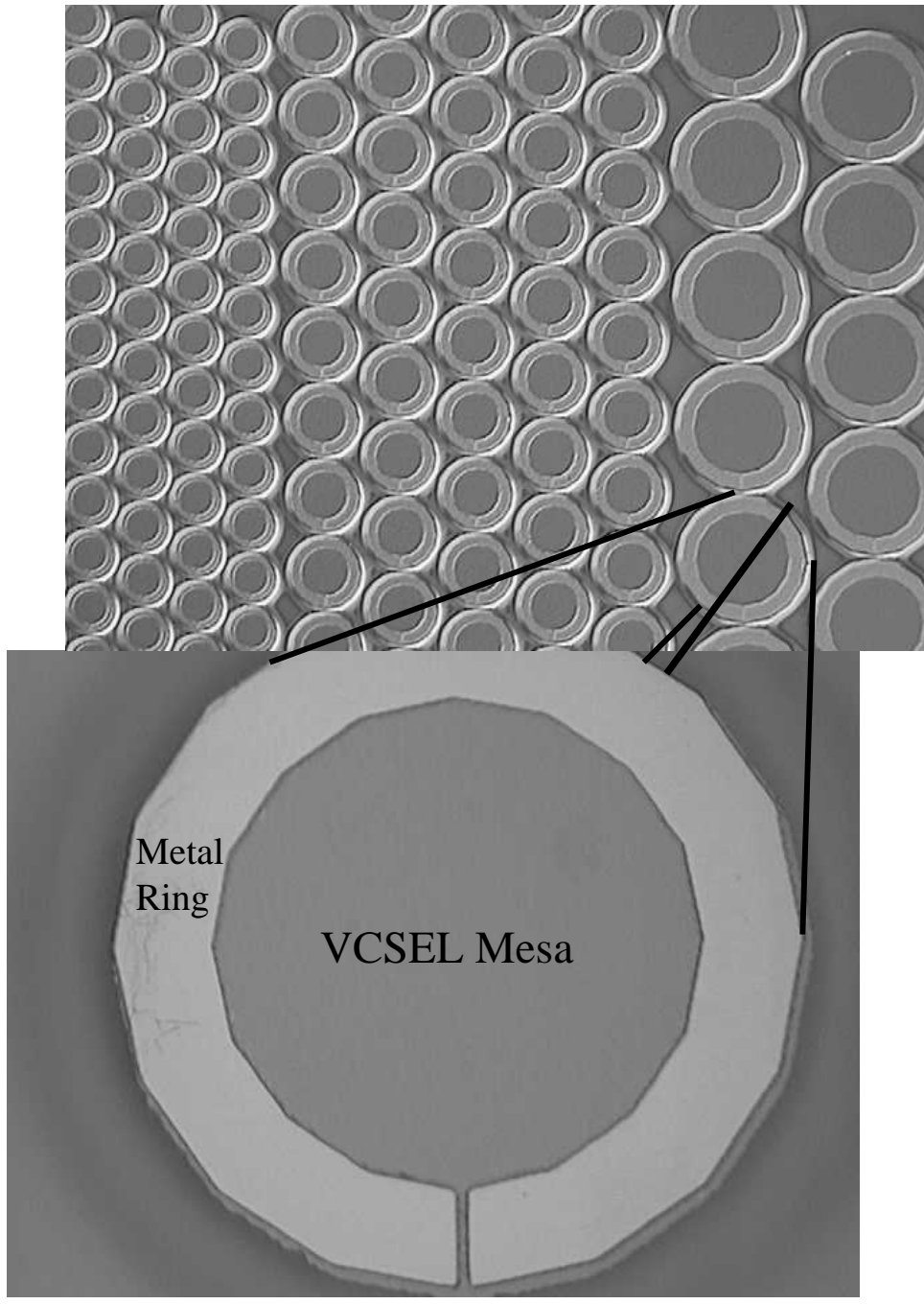


Figure 2.9 Metallized ohmic contacts deposited on VCSELs by e-beam evaporation.

2.7 Etching

2.7.1 *Wet Etching.* Wet etching consists of using a chemical that is either a liquid or dissolved in a liquid to remove semiconductor material from either the substrate or epitaxial layers. The three necessary elements for any wet chemical etch process are transportation of reactants to the surface, chemical reactions occurring at the material's surface, and removal of the reaction products [48]. These processes are illustrated in Figure 2.10.

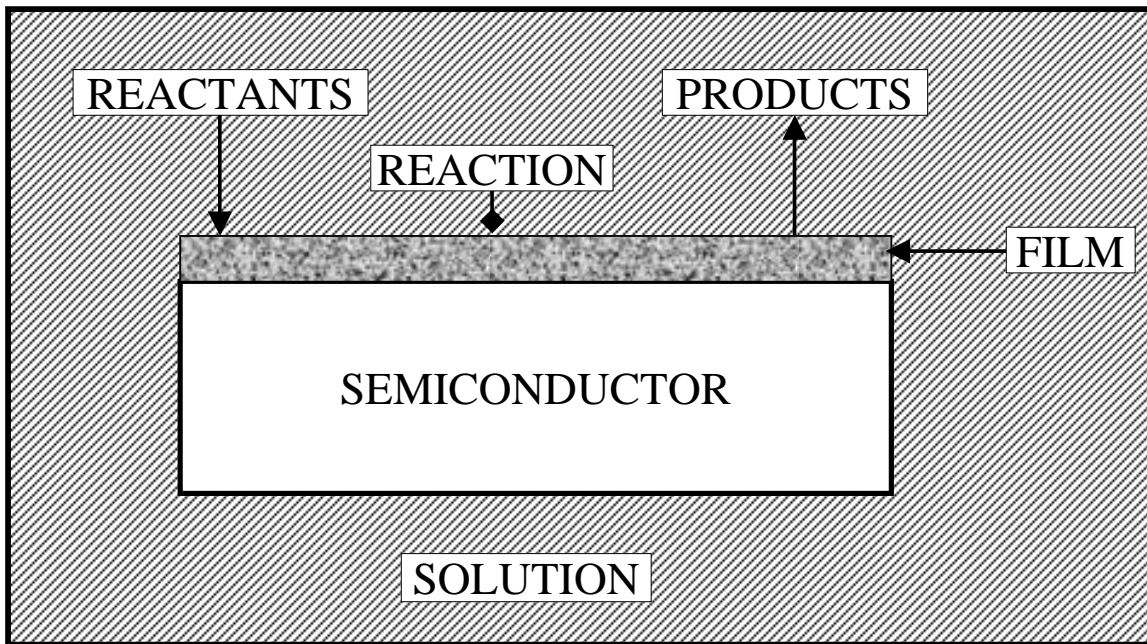
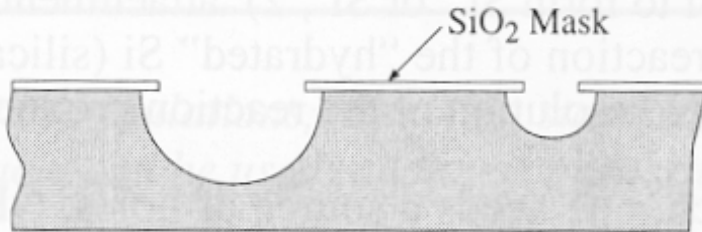


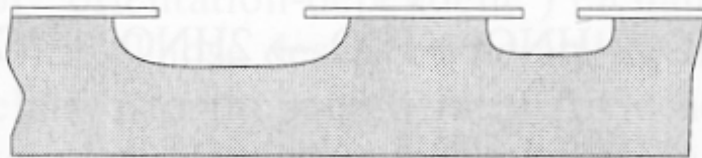
Figure 2.10 Diagram of a generic wet etching system, after [48].

Etch rates are affected by temperature, agitation of the etchant solution, mixture of etching chemicals, and crystal plane selectivity [48]. Whether an etch is selective against certain crystal planes determines whether it is isotropic or anisotropic. The difference between the two is illustrated in Figure 2.11.

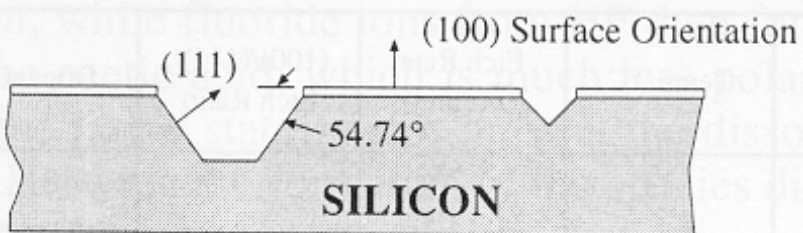
ISOTROPIC WET ETCHING: AGITATION



ISOTROPIC WET ETCHING: NO AGITATION



ANISOTROPIC WET ETCHING: (100) SURFACE



ANISOTROPIC WET ETCHING: (110) SURFACE

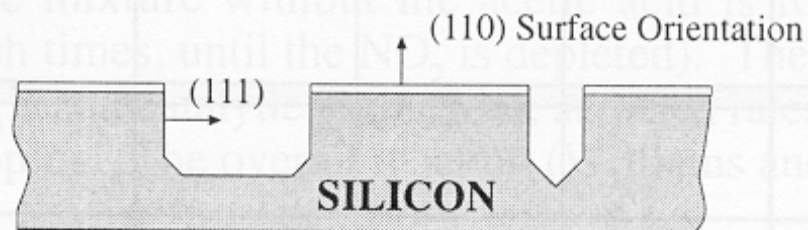


Figure 2.11 Comparison of isotropic and anisotropic wet etching [28].

2.7.2 Dry Etching. It is possible to etch materials in gases much the same way that they are etched in liquids. Namely, by immersion in the etching fluid. Gaseous etchants are available as isotropic etchants or with both crystal plane and material selectivity comparable to that found in liquid etchants. The main drawback to dry etching is difficulty associated with handling gases, especially since many of the etchants and the gaseous etch byproducts are toxic. The advantage of dry etching is the greater control over the process achieved by manipulating the flow rate of the etch gases rather than by immersing the sample in excess etchant as is done in wet etching [28]. An example of a dry etching system is shown in Figure 2.12.

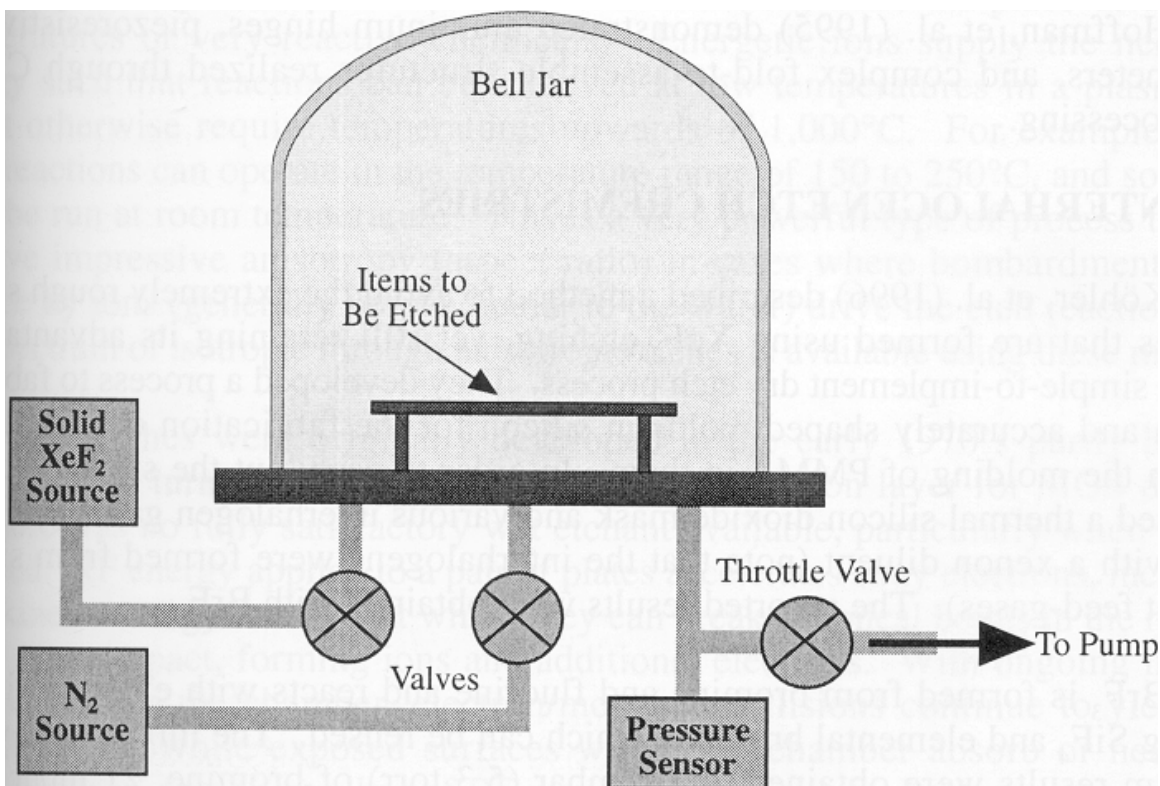


Figure 2.12 Diagram of a dry or gaseous etching system [21].

2.7.3 Reactive Ion Etching. Reactive Ion Etching (RIE) is a special type of dry etching that allows great anisotropy without dependence on crystal plane selectivity. This technology allows the formation of high-aspect-ratio structures with relatively vertical sidewalls [28]. For the purpose of this research RIE exposes multiple layers of epitaxially grown material so that etch selectivity among the materials can be observed. This technique of micromachining is relatively mature and has been used to etch III-V materials for several years [54]. Figure 2.13 shows an etch profile that is possible with RIE on a GaAs substrate with a Distributed Bragg Reflector (DBR) composed of alternating layers of $\text{Al}_{0.1}\text{Ga}_{0.9}\text{As}$ and $\text{Al}_{0.9}\text{Ga}_{0.1}\text{As}$. DBRs are described

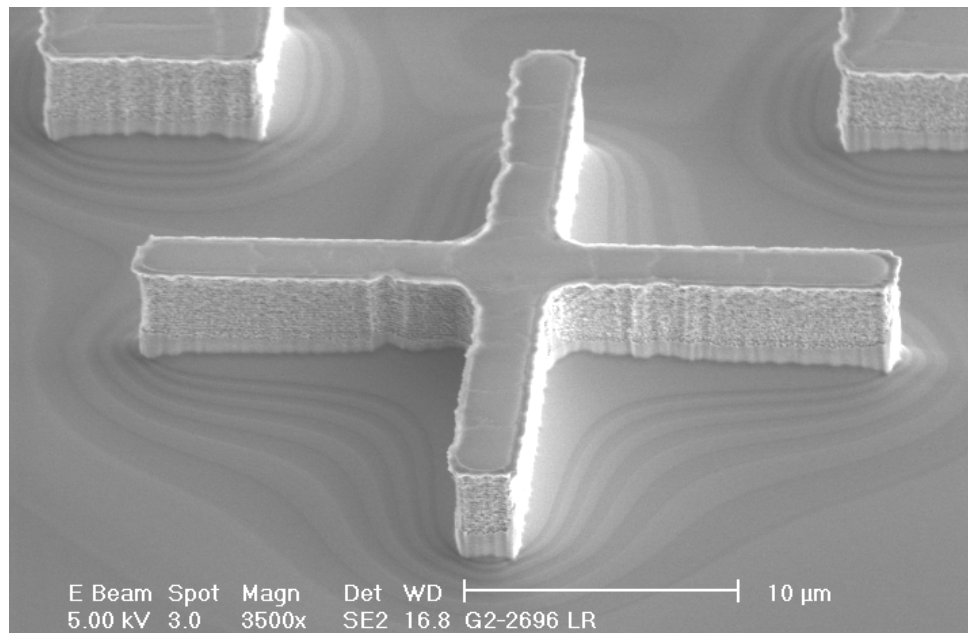


Figure 2.13 Example of a GaAs and $\text{Al}_x\text{Ga}_{1-x}\text{As}$ ($x = 0.1, 0.9$) structure etched using BCl_3 .

2.8 Wet Oxidation of AlAs

The oxidation process consists of exposing a sample containing an $\text{Al}_x\text{Ga}_{1-x}\text{As}$ ($x \geq 0.92$) at an elevated temperature to a source of oxygen. In the case of wet oxidation, the source of oxygen is water vapor. All oxidation performed for this research was executed in the low-temperature, low-pressure steam furnace constructed and reported by Feld, et al. [14, 31]. Figure 2.14 depicts this oxidation system.

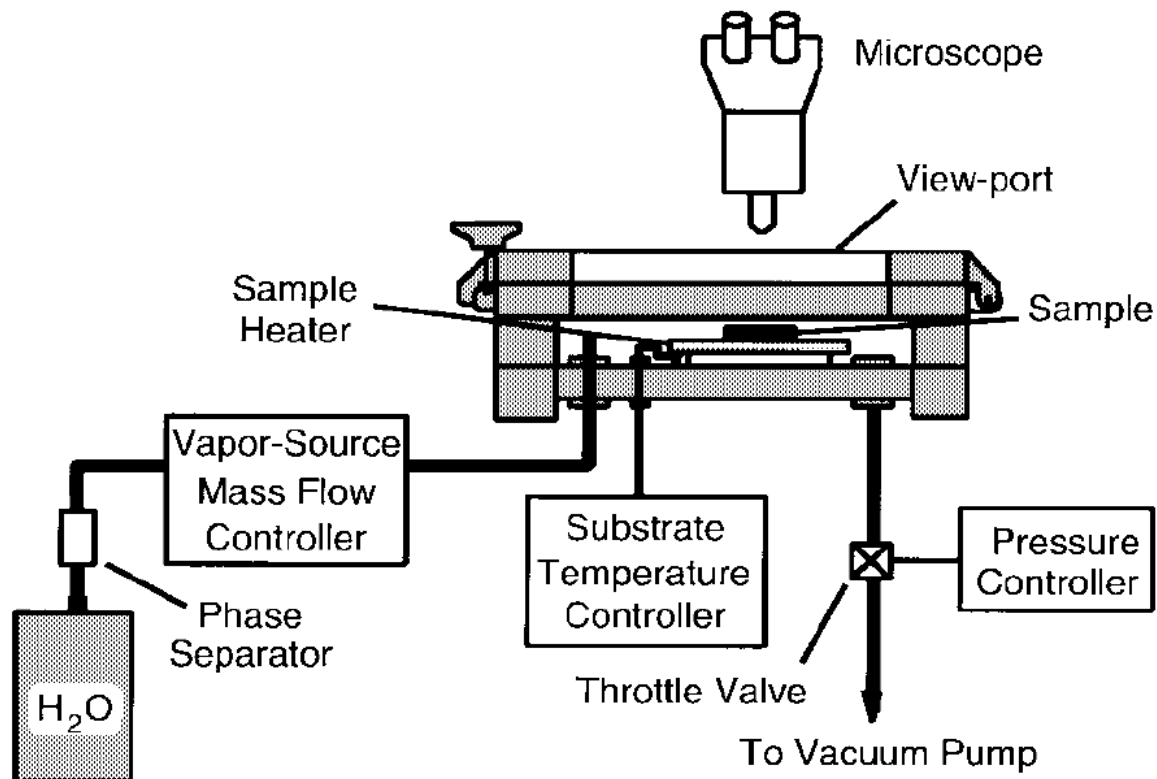


Figure 2.14 Diagram of the wet oxidation system used in my research [31]. The one-liter water bottle is warmed to approximately 50 °C. The phase separator traps liquid water droplets to keep them from propagating through the system and causing erroneous pressure or mass flow readings.

The most commonly manipulated variable in the oxidation process is time. Obviously, more material will oxidize the longer the process is allowed to continue. Temperature also affects the oxidation rate and is sometimes varied when a sample must not be subjected to temperature above a certain point or to manipulate the

quality of the oxide formed. The effects of time and temperature on samples oxidized in the system depicted in Figure 2.14 are illustrated graphically in Figure 2.15

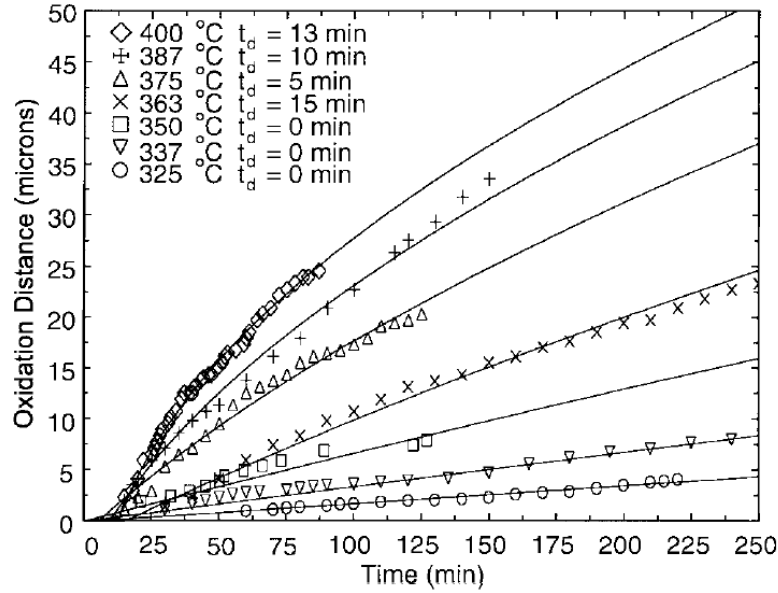


Figure 2.15 Graphical illustration of the effects of time and temperature on oxidation progress [14].

Other variables that affect the oxidation rate include pressure and mass flow of water vapor. These are generally not used to control the oxidation process since pressure must be kept low and water vapor is usually flowed in excess and not as a limiting reagent. In the design and MBE growth phase prior to oxidation, the aluminum content in the $\text{Al}_x\text{Ga}_{1-x}\text{As}$ alloy may be controlled. This has a profound effect on the rate of oxidation. The more aluminum present, the faster the rate of oxidation [2]. Layer thickness also affects the oxidation rate of a material in that a thicker layer oxidizes more rapidly [24]. This effect, however, is less important for layers more than 500 Å [40] to 800 Å [24] thick. Figure 2.16 shows a tunneling electron microscope (TEM) image of the progress of oxidation in AlAs depending only on layer thickness. Figure 2.17 more precisely shows experimental data collected on the effect of layer thickness on the oxidation rate of AlAs.

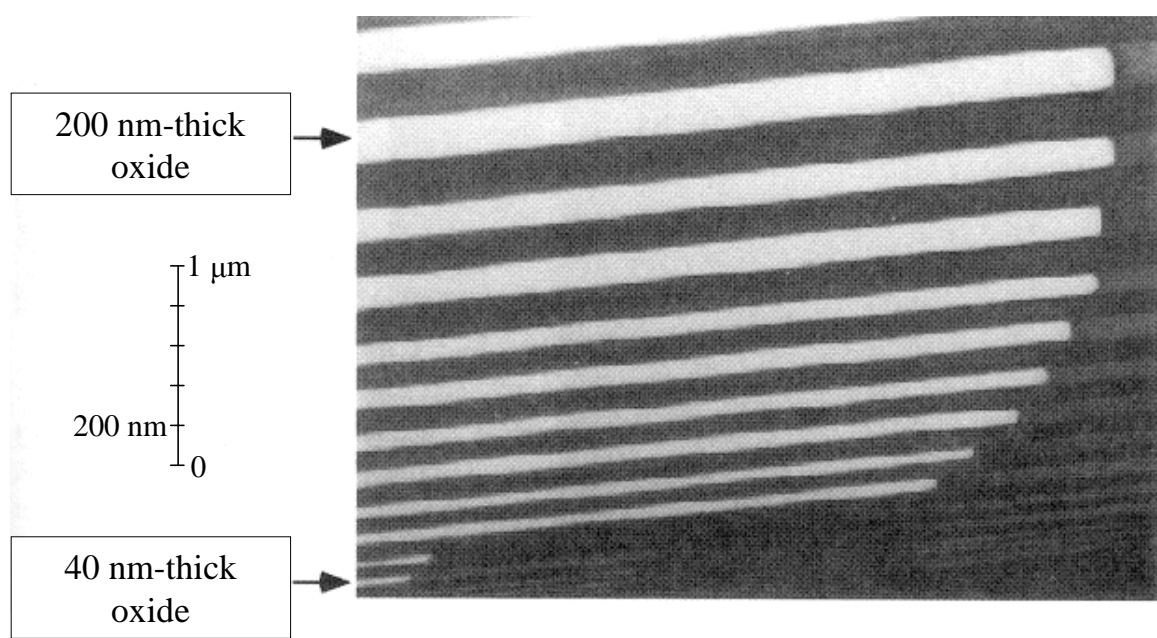


Figure 2.16 TEM image of oxidation progress depending only on layer thickness [11].

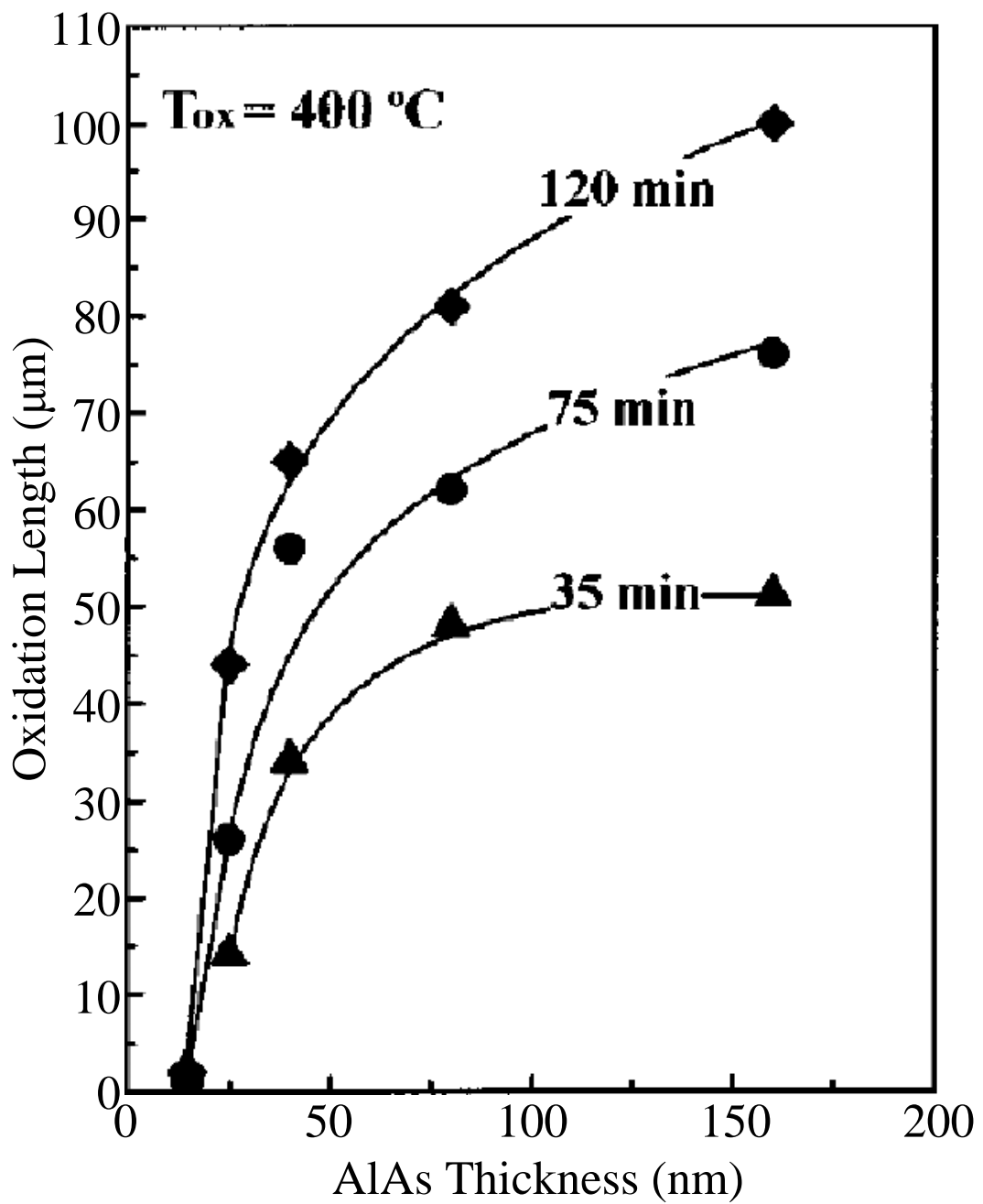


Figure 2.17 Graphical illustration of the effect of thickness upon oxidation rate [24].

Another fact that should be noted regarding wet oxidation with this system is that it does exhibit crystal plane selectivity. Figure 2.18 shows a picture of a structure that has a circular outer geometry and a square post indicating where material has not oxidized. In Figure 2.18 the $\{110\}$ planes have oxidized more rapidly than the $\{111\}$ planes, thus indicating crystal plane selectivity for $\text{Al}_x\text{Ga}_{1-x}\text{As}$ with high aluminum content ($x \geq 0.96$).

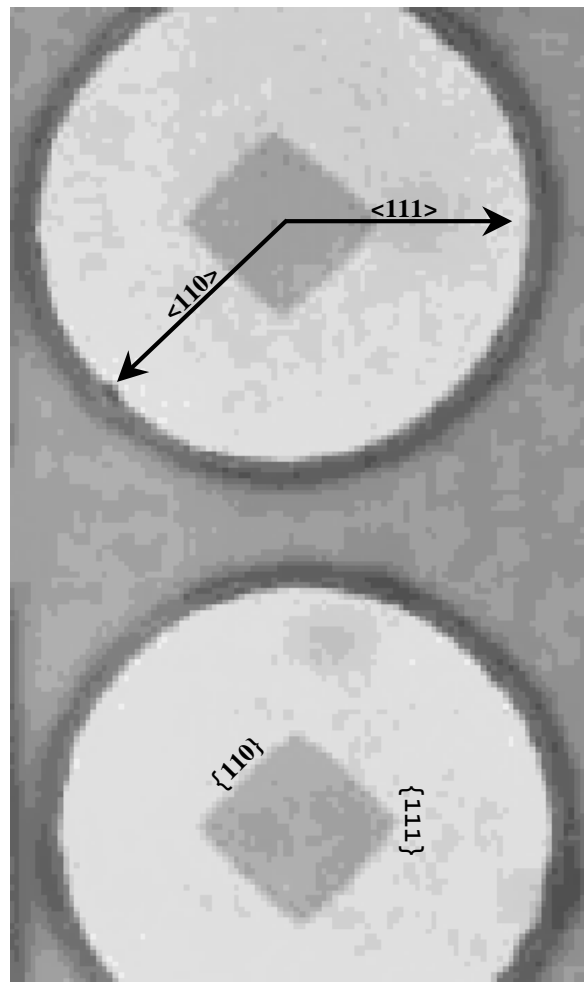


Figure 2.18 Optical image where the crystal plane selectivity of the oxidation process is manifested [31].

2.9 Structure Release

The key to surface micromachining for the construction of electrostatic actuators is the ability to release mechanical layers after growth and processing so that the layers are capable of motion. Release is achieved by performing a selective etch that dissolves a sacrificial layer while leaving the mechanical layers intact [6]. The challenge for releasing structures is to avoid allowing the surface tension of the evaporating rinse fluids to pull structures into contact with the substrate. This phenomenon is commonly called “stiction,” which can be defined as “the sticking of structures to the substrate after rinsing and drying” [6]. The concept of mechanical structure release is illustrated in Figure 2.19.

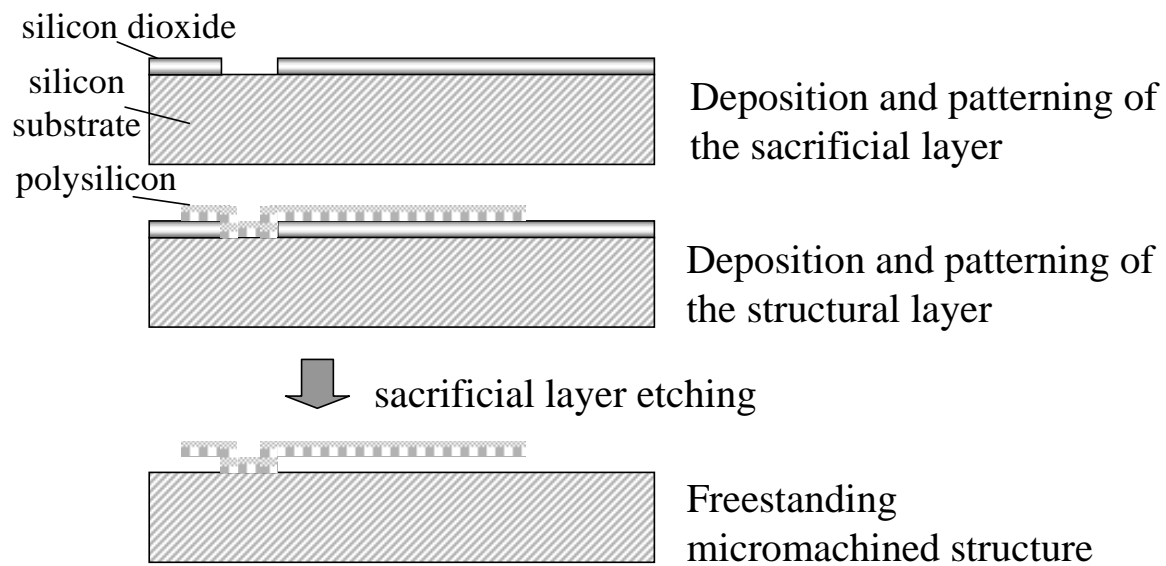


Figure 2.19 Illustration of the concept of sacrificial etching, after [13].

2.9.1 Wet Release. By far the easiest method of structural release is wet release. Wet release consists of immersing an entire wafer or die into a liquid etchant that removes the sacrificial layer(s) without etching the structural layers. High selectivity etchants are available for both silicon [3] and III-V materials [19]. The problem with wet release is that surface tension forces produced by evaporating

liquid etchant cause structures to come into contact at which point they may stick together due to van der Waals forces [28]. This capillary attraction is illustrated in Figure 2.20, and its effects on a test structure are shown in Figure 2.21.

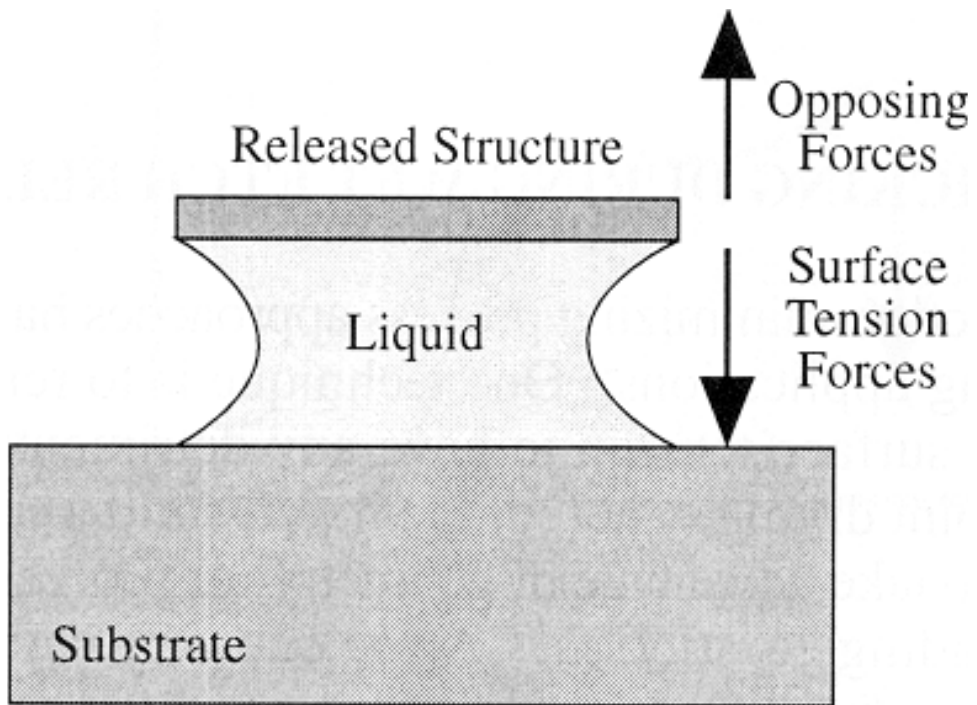


Figure 2.20 Forces involved in the problem of stiction [28]. In my structures, the opposing forces are limited to those resulting from the spring constant of the released structure.

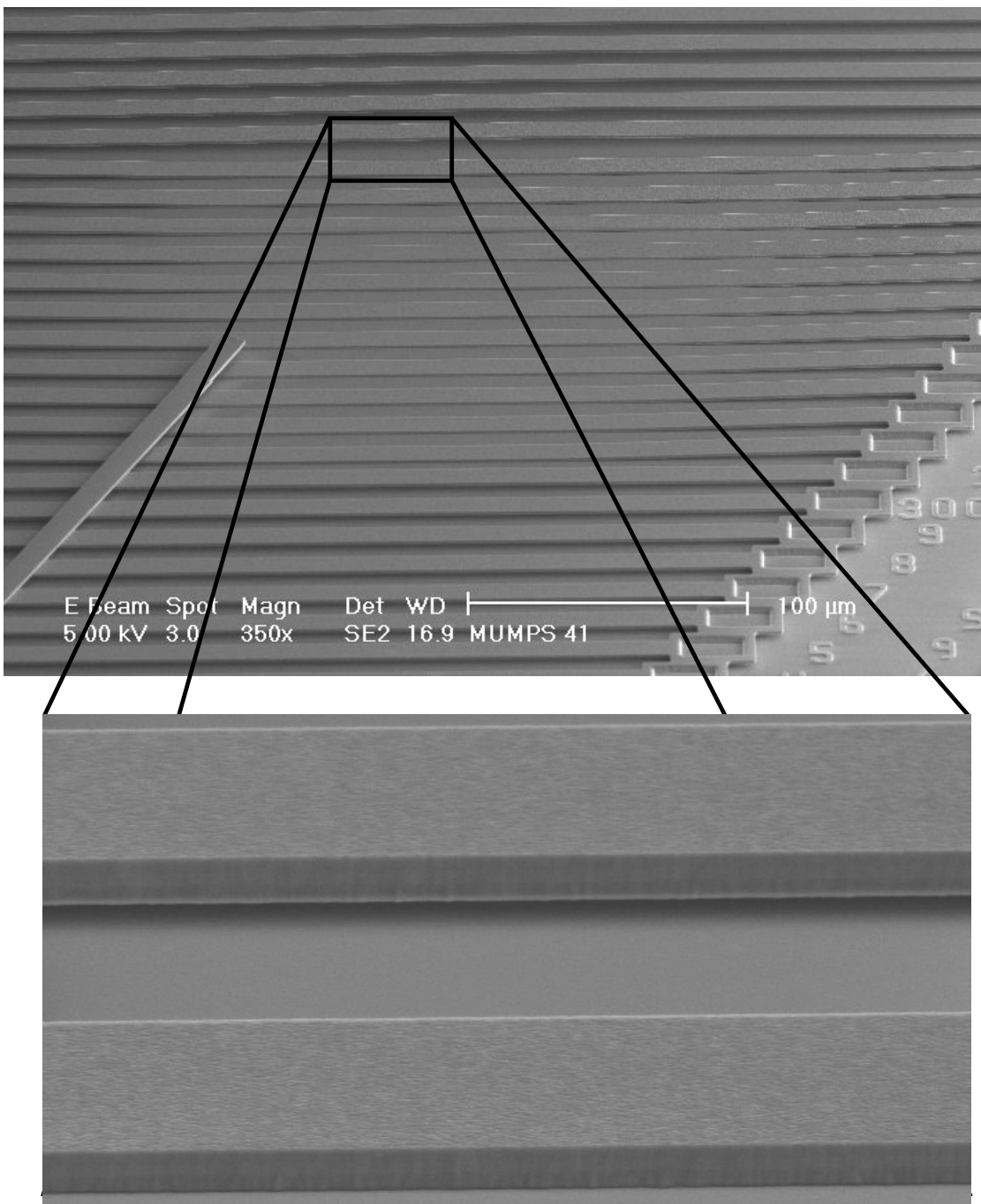


Figure 2.21 Image of an array of fixed-fixed beam structures fabricated using the MUMPs® process where stick-down has occurred. This array was processed with wet-release and no precautions were taken in its drying. The forces causing this stick-down are most likely capillary in nature rather than residual stress as evidenced by the fact that the longer beam did not experience stiction. The longer beam would have been more prone to buckling if the deflection were caused by residual stress. The longer structure did not stick down due to capillary forces because of the random nature of stiction induced by surface tension [46].

2.9.2 Dry Release. Stiction due to surface tension in liquids is eliminated when a gaseous chemical is used to release structures. This can be either a native gas, such as BCl_3 or a vapor form of a liquid etching solution [1]. This process can be either isotropic or anisotropic, as discussed in Section 2.7.3. The chief difficulty with this process is handling toxic etchants and by-products, as well as the appearance of a residual film on the sample, which must be removed [43].

2.9.2.1 Dry Release with a Silicon Sacrificial Layer. A variety of gases have been used for dry etching and dry release. Silicon has been selectively removed for MEMS applications using xenon difluoride (XeF_2) [21]. XeF_2 , however, tends to leave behind rough surfaces, so several interhalogen etch gases have been synthesized and used to etch silicon. These gases include bromine trifluoride (BrF_3) and chlorine trifluoride (ClF_3) [27]. A number of other gaseous etchants can be used to remove silicon and its common derivatives such as SiC , SiN and SiO_2 , but the most common gas for this purpose is SF_6 due to the fact that the others are largely chlorinated fluorocarbons which damage the earth's ozone layer when released [28].

2.9.2.2 Dry Release with an Organic Sacrificial Layer. Organic materials commonly used as sacrificial layers include photoresist and polyimide. Organic chemicals are commonly etched using oxygen (O_2) plasma. This process, known as "plasma ashing," can also be used to remove photoresist that is not easily removed with acetone or photoresist stripper due to processing conditions [28].

2.9.2.3 Dry Release with a Gallium Arsenide Sacrificial Layer. In order to remove GaAs selectively from a $\text{GaAs}/\text{AlGaAs}/\text{AlAs}$ system, the aluminum containing layers can be passivated by forming "a nonvolatile layer of aluminum fluoride" [30]. In general, a selective etch that attacks GaAs over AlGaAs must contain both a chlorine (Cl) donor and a fluorine (F) donor. Chlorine is typically supplied by BCl_3 or silicon tetrachloride (SiCl_4). Fluorine is typically supplied by

SF₆ or silicon tetrafluoride (SiF₄) [30]. Because of environmental concerns and the difficulty of handling the extremely toxic SiCl₄, I used only BCl₃ and SF₆ in my research.

2.9.3 Wet Release with CO₂ Drying. Recent research has shown that a drying process utilizing “supercritical carbon dioxide can be successfully used to alleviate the stiction problem and provide a clean and dry surface” [23]. The process works by rinsing etchants from the sample with methanol, displacing the methanol with liquid CO₂ in a pressure vessel (drying chamber), and raising the drying chamber’s temperature above the critical point of CO₂. The critical point exists in the range of pressure and temperature values where CO₂ exists as both a liquid and a gas. This process is illustrated graphically in Figure 2.22. The pressure vessel’s temperature is held constant at this supercritical temperature while it is vented, allowing the CO₂ to escape as a gas without ever forming a liquid to solid interface. The lack of an interface eliminates the effects of surface tension during drying [23].

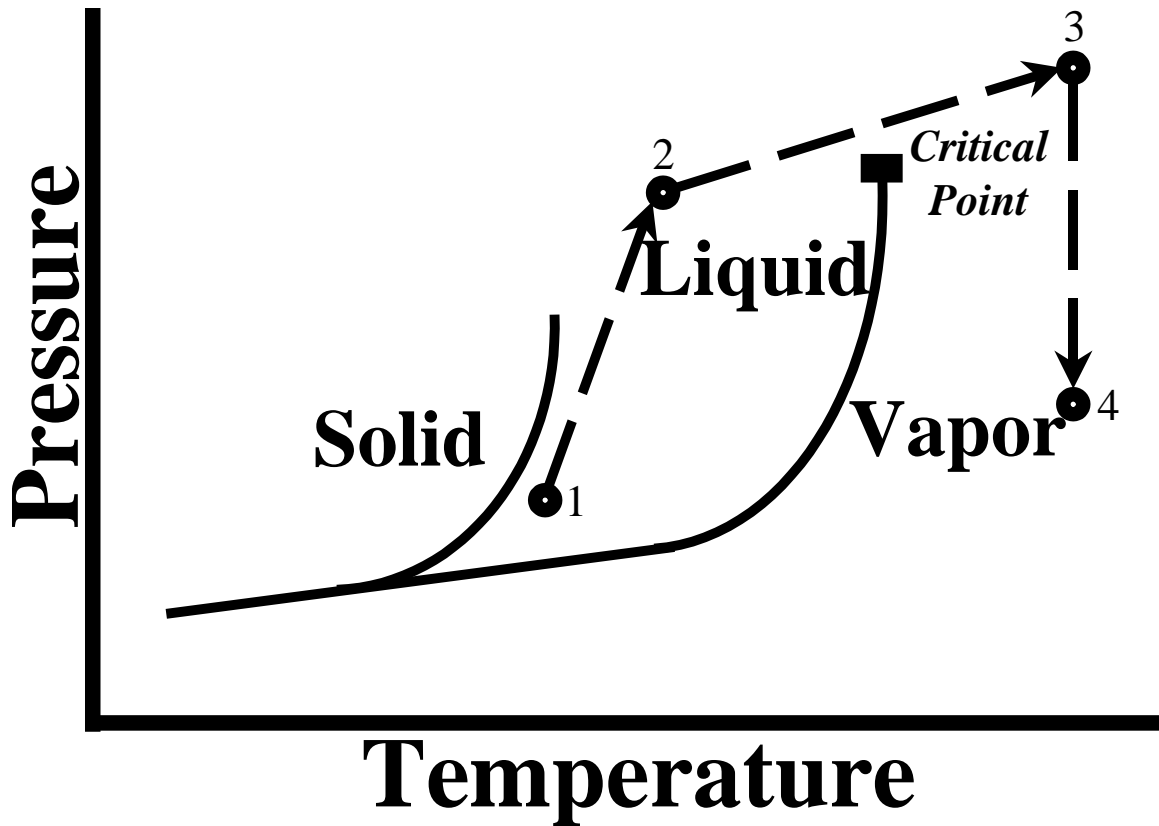


Figure 2.22 Phases of CO₂ for various combinations of pressure and temperature with the regions used for release annotated, after [23]. The release process begins at point 1, where liquid CO₂ displaces methanol. The pressure of the drying chamber is raised (point 2) to prevent the liquid from evaporating in the normal fashion when the temperature is raised (point 3). The CO₂ now exists in a supercritical state where it is both a liquid and a gas with no interface between the two. As the pressure is released the CO₂ becomes all vapor and escapes from the drying chamber (point 4).

2.10 Optical Devices

2.10.1 Distributed Bragg Reflectors. A distributed Bragg reflector (DBR) consists of a number of pairs of high (n_h) and low(n_l) index of refraction materials stacked atop a substrate(n_s) as shown in Figure 2.23.

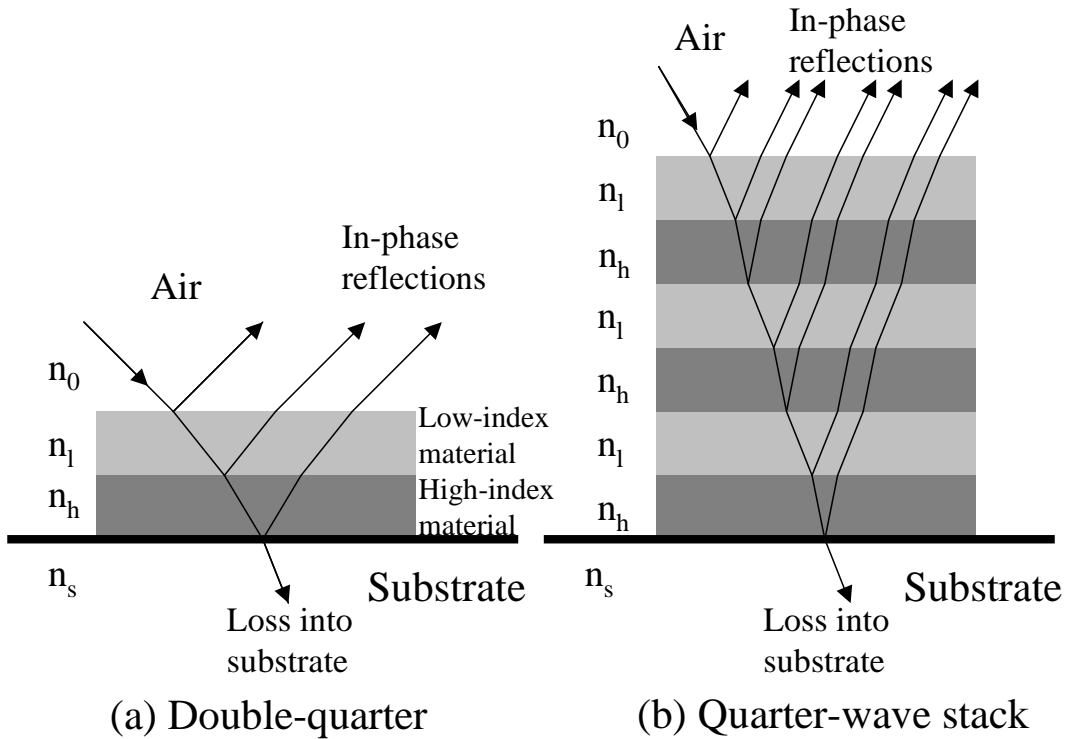


Figure 2.23 Illustration of a basic DBR, after [16].

If each of the layers of material has an optical thickness equal to a quarter of the design wavelength (λ_{design}), the light emerging from the top of a quarter-wave ($\lambda_{design}/4n$) stack is a result of multiple reflections that add in phase to provide significant reflectivity [16]. This effect is most pronounced at the design wavelength and at normal incidence, but is also present at adjacent wavelengths as shown in Figure 2.24.

The range of wavelengths where high reflectivity is present is also affected by the angle away from normal incidence where the phenomenon is observed [33]. The calculation used to produce Figure 2.24 assumes normal incidence.

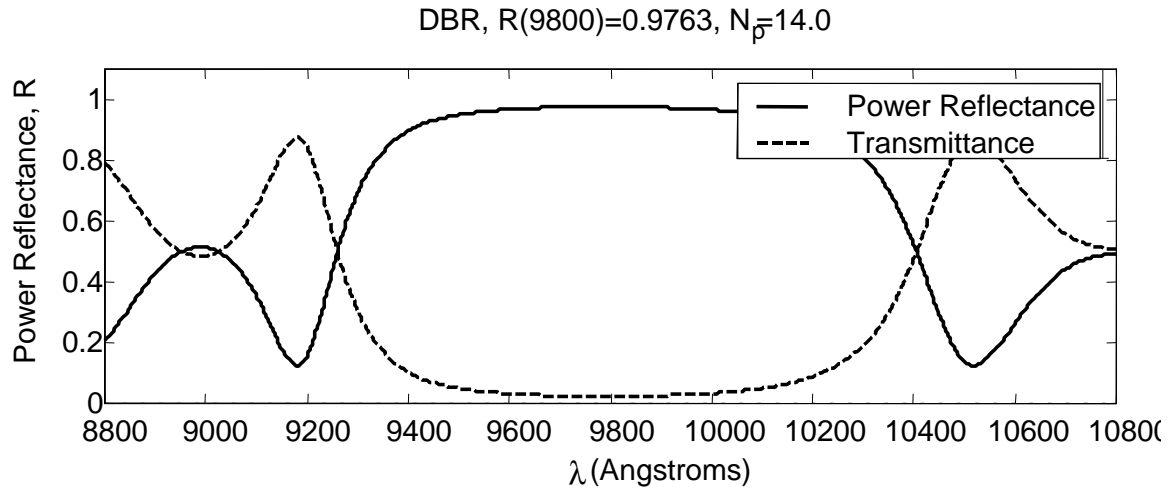


Figure 2.24 Mathematically modelled power reflectance and transmittance versus wavelength at normal incidence for a DBR designed to be 97% reflecting at $\lambda_{design} = 9800 \text{ \AA}$. The high-index layers of the 14 pair quarter-wave stack are composed of $\text{Al}_{0.1}\text{Ga}_{0.9}\text{As}$ ($n = 3.47$, 706 \AA thick) and the low-index layers are composed of $\text{Al}_{0.9}\text{Ga}_{0.1}\text{As}$ ($n = 3.02$, 810 \AA thick) all on a GaAs substrate. This model assumes no absorption, since absorption is negligible over the range shown for these materials [42].

2.10.2 Fabry-Perot Interferometers.

2.10.2.1 Fixed Filter Etalon. A Fabry-Perot filter consists of two parallel reflectors usually separated by a positive integer multiple of $\lambda/2$ [33]. By placing this microcavity between two DBRs, light will be transmitted corresponding to a narrow sharp peak in frequency space, thus the Fabry-Perot interferometer serves as a band-pass filter [42]. The resonant wavelength at normal incidence is governed by Equation 2.10 [52], where the units of measurement for the wavelength are the same as those for the distance between reflectors (usually μm or nm).

$$\lambda_{res} = \frac{2nd}{q} \quad (\text{nm}) \quad (2.10)$$

where

- n Index of refraction of the material filling the cavity
- d = Distance between DBRs (length of microcavity)
- q = Positive integer corresponding to the resonant mode of interest

Filtering behavior at normal incidence is shown in Figure 2.25. This type of structure is commonly fabricated from semiconductor materials [8, 9, 53]. The vertical cavity surface emitting laser (VCSEL) is basically a multi-layer Fabry-Perot etalon. It is composed of two DBRs surrounding a microcavity. The microcavity typically contains active quantum well gain layers that generate light [33].

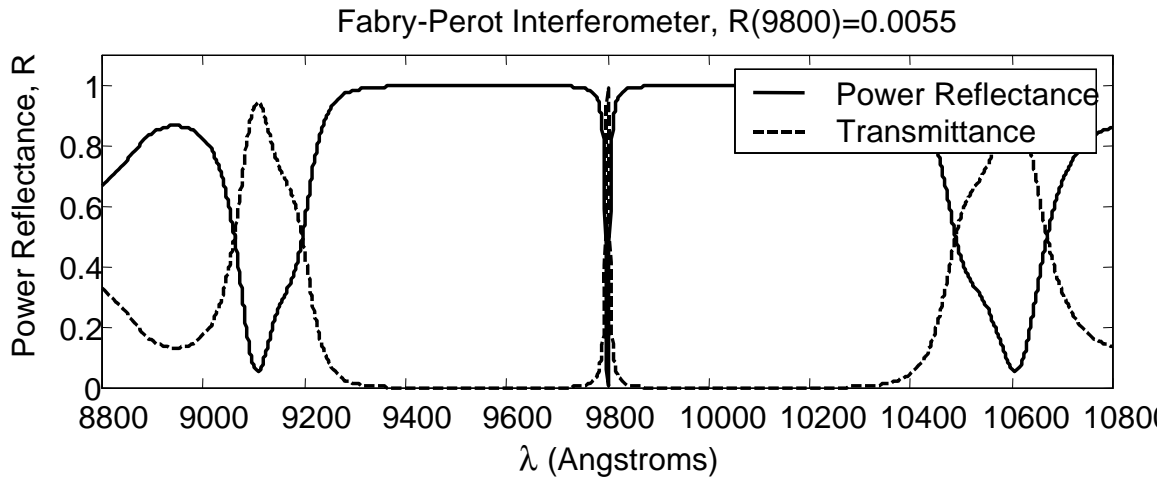


Figure 2.25 Mathematically modelled power reflectance and transmittance versus wavelength for a Fabry-Perot interferometer with $\lambda_{design} = 980$ nm. The compositions and thicknesses of layers are identical to those in Figure 2.24, except that the two DBRs are designed to be 99% reflecting. The microcavity is composed of air and is 4900 Å-thick [42].

2.10.2.2 Tunable Filter. By varying the distance between the two DBRs in a Fabry-Perot interferometer, it is possible to change the fundamental axial wavelength for which the structure is resonant—the equivalent of changing the passband on a filter. This behavior is apparent from Equation 2.10, in which a change in d necessitates a change in λ . A tunable Fabry-Perot filter, laser, or resonant cavity light emitting diode (RCLED) can be fabricated from III-V materials [47]. The techniques refined in my research are intended to enable the production of such devices.

2.11 Zygo New View 5000 Interferometry System

For measuring small deflection distances and obtaining a qualitative sense of surface flatness, I used a Zygo interferometry system. Interferometry systems measure distances by splitting a coherent beam of light, reflecting one portion of the beam off of a mirror a known distance away and reflecting the other off of a sample that needs to be measured. The beams each travel a different distance, which means that when both return to the beam splitter, they are out of phase with one another. Differences in the phase appear as fringe lines. Fringe lines are the manifestation of constructive and destructive interference from the two beams [16]. With a flat sample in place the fringe lines are parallel. These lines shift as the structure moves, but as long as it remains flat, the lines remain parallel. If the surface is not flat, the lines will bend. Sometimes this bending is so severe as to cause circular interference patterns. This phenomenon allows for a qualitative observation of surface flatness. By counting the number of fringe lines that shift over a given surface when the mirror of known distance is being moved, the Zygo system quantifies the height of a structure relative to a substrate or other nearby features.

2.12 Conclusion

There are a great variety of technologies that must converge to create useable MOEMS. The work previously performed in silicon MEMS is important since these structures are the best prototypes for applications in III-V MEMS. In this chapter I have discussed the limitations of silicon MEMS and I have given a justification for the pursuit of research concerning III-V MEMS. I have included information needed to understand how semiconductor and MEMS materials are grown so that they can be processed into useful devices. I also reviewed the basic semiconductor processing and yield enhancement techniques used in my research. Finally, the optical principles behind my devices are discussed. The purpose of this chapter is to allow the reader to

come to a full understanding of how the devices used in my research were fabricated and how they operate.

Because the goal of my research is to investigate processing techniques for MOEMS, an understanding of mechanical MEMS, semiconductor processing techniques, and optical principles is necessary to take this step. The work of previous researchers presented here is the basis for the procedures I report in Chapter III. The material contained in Chapter II shows that the methods presented in Chapter III are based on sound semiconductor processing, MEMS and optical principles that should lead to the successful fabrication of devices.

Bibliography

1. Anguita, J. and Briones, F. “HF/H₂O Vapor Etching of SiO₂ Sacrificial Layer Etching for Large-Area Surface-Micromachined Membranes,” *Sensors and Actuators A, Physical*, 64(3):247–251 (January 1998).
2. Bernhard, W. L. *Optical and Etching Studies of Native Aluminum Oxide Layers for Use in Microcavity Photonic Devices*. Master’s Thesis, Air Force Institute of Technology, Wright-Patterson Air Force Base, OH, March 2001.
3. Bühler, J., Steiner, F.-. P., and Baltes, H. “Silicon Dioxide Sacrificial Layer Etching in Surface Micromachining,” *Journal of Micromechanics and Microengineering*, 7:R1–R13 (1997).
4. Burke, T. M., Brown, S. J., Smith, M. P., Linfield, E. H., Ritchie, D. A., Pepper, M., Tang, K. B. K., Palmer, R. E., and Burroughes, J. H. “Hydrogen Radical Cleaning and Low Energy Electron Stimulated Desorption of Surface Contaminants for MBE Regrowth of GaAs,” *Applied Surface Science*, 123/124:308–312 (January 1998).
5. Burke, T. M., Linfield, E. H., Ritchie, D. A., Pepper, M., and Burroughes, J. H. “Hydrogen Radical Surface Cleaning of GaAs for MBE Regrowth,” *Journal of Crystal Growth*, 175/176(1):416–421 (May 1997).
6. Bustillo, J. M., Howe, R. T., and Muller, R. S. “Surface Micromachining for Microelectromechanical Systems,” *Proceedings of the IEEE*, 86(8):1552–1574 (August 1998).
7. Chang, H.-C., Chang, E. Y., Chung, C.-C., and Kuo, C. T. “Highly Selective GaAs/Al_{0.2}Ga_{0.8}As Wet Etch Process for the Gate Recess of Low-Voltage-Power Pseudomorphic High-Electron-Mobility Transistor,” *Japanese Journal of Applied Physics, Part 1*, 39(8):4699–4703 (2000).
8. Chen, G., Leger, J. R., and Gopinath, A. “Angular Filtering of Spatial Modes in a Vertical-Cavity Surface-Emitting Laser by a FabryPerot Etalon,” *Applied Physics Letters*, 74(8):1069–1071 (February 1999).
9. Chen, P.-L., Lin, K.-C., Chuang, W.-C., Tzeng, Y.-C., Lee, K.-Y., and Lee, W.-Y. “Analysis of a Liquid Crystal FabryPerot Etalon Filter: A Novel Model,” *IEEE Photonics Technology Letters*, 9(4):467–469 (April 1997).
10. Chen, W. D., Xie, X. L., Cui, Y. D., Chen, C. H., and Hsu, C. C. “Microstructure Studies of PdGe/Ge Ohmic Contacts to n-type GaAs Formed by Rapid Thermal Annealing,” *Applied Surface Science*, 100/101:530–533 (July 1996).

11. Choquette, K. D. *The Technology of Selectively Oxidized Vertical-Cavity Lasers*, Chapter 2, 63–107. Optoelectronic Properties of Semiconductors and Superlattices, Gordon and Breach Science Publishers, 1999. Wilmsen, C., Temkin, H., and Coldren, L. A., editors.
12. Eberl, K., Lipinski, M., and Schuler, H. “Atomic layer in situ etching and MBE regrowth,” *Journal of Crystal Growth*, 201/202:568–573 (May 1999).
13. Elbrecht, L., “Surface Micromachining.” Electronic, June 1998.
14. Feld, S. A., Loehr, J. P., Sherriff, R. E., Wiemer, J., and Kaspi, R. “In Situ Optical Monitoring of AlAs Wet Oxidation Using a Novel Low-Temperature Low-Pressure Steam Furnace Design,” *IEEE Photonics Technology Letters*, 10(2):197–199 (1998).
15. Geißelbrecht, W., Pfeiffer, U., Thrunhardt, A., Klitz, U., Gossard, A. C., and Dhler, G. H. “An Optimized Digital Alloy Growth Technique for Accurate Band Gap Engineering,” *Journal of Crystal Growth*, 201/202:163–165 (May 1999).
16. Hecht, E. *Optics* (Third Edition). Reading, Massachusetts: Addison-Wesley, 1998.
17. Hjort, K. “Micromachining in Bulk GaAs,” *Sensors and Materials*, 2(1):1–5 (1990).
18. Hjort, K. “Gallium Arsenide as a Mechanical Material,” *Journal of Micromechanics and Microengineering*, 4(1):1–13 (March 1994).
19. Hjort, K. “Sacrificial Etching of III–V Compounds for Micromechanical Devices,” *Journal of Micromechanics and Microengineering*, 6(4):370–375 (December 1996).
20. Hjort, K., Schweitz, J.-Å., and Hök, B. “Bulk and Surface Micromachining of GaAs Structures,” *Annual International Workshop on Micro-Electro-Mechanical Systems*. Napa Valley, California, February 1990.
21. Hoffman, E., Warneke, B., Kruglick, E., Weigold, J., and Pister, K. S. J. “3D Structures with Piezoresistive Sensors in Standard CMOS,” *Proceedings of the IEEE Micro Electro Mechanical Systems Conference*. January–February 1995.
22. Iizuka, K., Matsumaru, K., Suzuki, T., Takahira, Y., Nishioka, T., and Okamoto, H. “High-Temperature Surface Cleaning of AlGaAs without As Flux for MBE Regrowth,” *Journal of Crystal Growth*, 175/176(1):416–421 (May 1997).
23. Jafri, I. H., Moritz, H. D., Busta, H. H., and Walsh, S., “Supercritical Carbon Dioxide Drying and Cleaning: Application to MEMS Technology.” mstnews: international newsletter on MICROSYSTEMS and MEMS, Electronic, April 1999.

24. Kim, J.-H., Lim, D. H., Kim, K. S., Yang, G. M., Lim, K. Y., and Lee, H. J. "Lateral Wet Oxidation of $\text{Al}_x\text{Ga}_{1-x}\text{As}$ -GaAs Depending on Its Structures," *Applied Physics Letters*, 69(22):3357–3359 (November 1996).
25. Kladitis, P. E. *Self Assembly of Microstructures*. Master's Thesis, Air Force Institute of Technology, Wright-Patterson Air Force Base, OH, December 1997.
26. Koester, D. A., Mahadevan, R., Hardy, B., and Markus, K. W. *MUMPs® Design Handbook, Revision 6.0*. Cronos Integrated Microsystems, 2001. www.memsrus.com/cronos/mumps.pdf.
27. Köhler, U., Guber, A. E., Bier, W., Hecke, M., and Schaller, T. "Fabrication of Microlenses by Combining Silicon Technology, Mechanical Micromachining and Plastic Molding," *Miniaturized Systems with Micro-Optics and Micromechanics*. January-February 1996.
28. Kovacs, G. T. A. *Micromachined Transducers Sourcebook*. Boston: McGraw-Hill, 1998.
29. Kovacs, G. T. A., Maluf, N. I., and Petersen, K. E. "Bulk Micromachining of Silicon," *Proceedings of the IEEE*, 86(8):1536–1551 (August 1998).
30. Lee, Y.-S., Upadhyaya, K., Nordheden, J., and Kao, M.-Y. "Selective Reactive Ion Etching of GaAs/AlAs in BCl_3/SF_6 for gate recess," *Journal of Vacuum Science and Technology, B*, 18(5):2505–2508 (September/October 2000).
31. Loehr, J. P. and Feld, S. A. "Control and Stability of AlAs Wet Oxidation Studied by *in-situ* Optical Monitoring in a Low-Pressure, Low-Temperature Steam Furnace," *Lasers and Electro-Optics Society Annual Meeting*. December 1998.
32. Lott, J. A., "Private Communication." Professor of Electrical Engineering, Air Force Institute of Technology, Department of Electrical and Computer Engineering, Wright-Patterson AFB, OH. 23 February 2002.
33. Lott, J. A., "Course Handouts from OENG 775, Air Force Institute of Technology." Unpublished, Summer 2001.
34. Lott, J. A. "Progress in Red Vertical Cavity Surface Emitting Lasers," *Proceedings 7th International Symposium Nanostructures: Physics and Technology*. St. Petersburg, Russian Federation, 14-18 June 1999.
35. Madou, M. J. *Fundamentals of Microfabrication*. Boca Raton: CRC Press, 1997.
36. Magel, G. A., "Tutorial: Micromachining in Optics." OSA Annual Meeting, October 1996. www.dlp.com/dlp/resources/whitepapers/pdf/micro.pdf.
37. May, G., Mitchell, K., Kerdoncuff, G., Parks, J., Brown, T., and Krawiecki, J., "Metallization." Electronic. <http://www.ece.gatech.edu/research/labs/vc/theory/metalliz.html>.

38. Muessig, H., Hackbarth, T., Brugger, H., Orth, A., Reithmaier, J. P., and Forchel, A. "A Closed UHV Focused Ion Beam Patterning and MBE Regrowth Technique," *Materials Science and Engineering*, *B35*(1-3):208–213 (December 1995).
39. Nagel, D. J. and Zaghloul, M. E. "MEMS: Micro Technology, Mega Impact," *IEEE Circuits and Devices Magazine*, *17*(2):14–25 (March 2001).
40. Naone, R. A. and Coldren, L. A. "Surface Energy Model for the Thickness Dependence of the Lateral Oxidation of AlAs," *Journal of Applied Physics*, *82*(5):2277–2280 (September 1997).
41. Neamen, D. A. *Semiconductor Physics & Devices: Basic Principles* (Second Edition). Chicago: Irwin, 1997.
42. Ochoa, E. M., "oeng775tools: A MATLAB® Toolbox." AFIT/ENG, Wright-Patterson AFB, OH, Unpublished, February 2001.
43. Ochoa, E. M. *Microelectromechanically-Tunable Vertical Cavity Surface Emitting Lasers*. Dissertation Prospectus, Air Force Institute of Technology, Wright-Patterson Air Force Base, OH, August 2001. Unpublished.
44. Petersen, K. E. "Dynamic Micromechanics on Silicon: Techniques and Devices," *IEEE Transactions on Electron Devices*, *ED-25*(10):1241–1250 (October 1978).
45. Saleh, B. E. A. and Teich, M. C. *Fundamentals of Photonics*. Wiley Series in Pure and Applied Optics, New York: John Wiley & Sons, Inc., 1991.
46. Starman, L. A., "Private Communication." Ph. D. Candidate, Air Force Institute of Technology, Department of Electrical and Computer Engineering, Wright-Patterson AFB, OH. 26 November 2001.
47. Strassner, M., Daleiden, J., Chitica, N., Keiper, D., Stalnacke, B., Greek, S., and Hjort, K. "III-V Semiconductor Material for Tunable FabryPerot Filters for Coarse and Dense WDM Systems," *Sensors and Actuators A, Physical*, *85*(1-3):249–255 (August 2000).
48. Sze, S. M. *Semiconductor Devices: Physics and Technology*. New York: John Wiley & Sons, 1985.
49. Tyree, V., Pi, J.-I., Pina, C., Hansford, W., Marshall, J., Gaitan, M., Zaghloul, M., and Novotny, D., "NIST MEMS Library, Section IV B." Electronic, 1993. <http://www.mosis.org/Technical/Designsupport/nist-mems-1.html>.
50. Uenishi, Y., Tanaka, H., and Ukita, H. "Characterization of AlGaAs Microstructure Fabricated by AlGaAs/GaAs Micromachining," *IEEE Transactions on Electron Devices*, *41*(10):1778–1783 (October 1994).
51. Van Nostrand, J. E., "Private Communication." Materials Research Engineer, Air Force Research Laboratory, Materials and Manufacturing Directorate, Wright-Patterson AFB, OH. 25 September 2001.

52. Verheyen, J. T. *Laser Electronics*. Upper Saddle River, New Jersey: Prentice Hall, November 2000.
53. Yoo, Y. S., Kim, J. W., Lee, J. Y., and Hahn, J. W. "High-Resolution Cavity Ringdown Spectroscopy with a Fabry-Perot Etalon at the Cavity Output," *Chemical Physics Letters*, 330(5-6):528–534 (November 2000).
54. Zhang, Z. L. and MacDonald, N. C. "Fabrication of Submicron High-Aspect-Ratio GaAs Actuators," *Journal of Microelectromechanical Systems*, 2(2):66–73 (June 1993).

III. Experimental Procedures

3.1 Introduction

In this chapter, I present the details of the experiments I undertook in order to characterize III-V materials with respect to various etchants and use this knowledge to fabricate MOEMS (see Section 1.3.1). Because my etch studies and applications utilize UV contact mask lithography, I first discuss lithography mask design. With this basis, I discuss the implementation of each of my fabrication studies. Finally, I discuss the fabrication methodology for the tunable Fabry-Perot interferometers and lift-off optical devices that I fabricated with the knowledge I gained from the etch study portion of my work.

3.2 Process Steps

In this section, I discuss three primary fabrication steps that are integral to both my etch studies and to the fabrication of MEM-tunable Fabry-Perot filters and lift-off microcavity light emitting devices.

3.2.1 Metal Deposition. The first step in my processes was the deposition and patterning of a layer of metal. This metal serves to label mask features and provide ohmic contacts for mechanical structures. The metal also protects the edges of structures being studied from sidewall undulations (commonly called “scalloping”) during Reactive Ion Etching (RIE) because RIE does not attack metal as aggressively as it attacks photoresist. The metal deposition step places labels and alignment marks on the wafer, defines the shapes used for the etch studies, and provides contacts for structures that will be actuated later. This lift-off metallization was performed as described in Section 2.6. I performed metal deposition first because lift-off processes perform best before any features have been defined on the surface. For a simple mesa structure, the sample would appear as drawn in Figure 3.1. The

center area represents a portion of the sample set aside for monitoring as described in Section 3.2.2.

3.2.2 DBR Removal. Because I wanted to monitor the progress of the etch or oxidation in some cases, I also designed a step to remove DBR layers so that the underlying sacrificial layer could be more easily observed. As AlAs or $\text{Al}_{0.98}\text{Ga}_{0.02}\text{As}$ oxidizes, its index of refraction changes and the oxidation progress can be monitored by imaging through the $\text{Al}_x\text{Ga}_{1-x}\text{As}$ mechanical layer above it. Although $\text{Al}_x\text{Ga}_{1-x}\text{As}$ compounds are generally transparent to infrared radiation, a DBR designed to be highly reflective at a wavelength of 980 nm will not transmit enough infrared to image the sacrificial layer beneath. For this reason most of the DBR is removed during this step to allow monitoring. A few pairs of the DBR must remain to ensure that the etchant or oxidizing species can react with the sacrificial material only from the sides and not from the top. If the DBRs were completely removed, the etchant or oxidizer would quickly remove the area underneath and any monitoring would be pointless. A sample as it might appear after the DBR removal step is drawn in Figure 3.2.

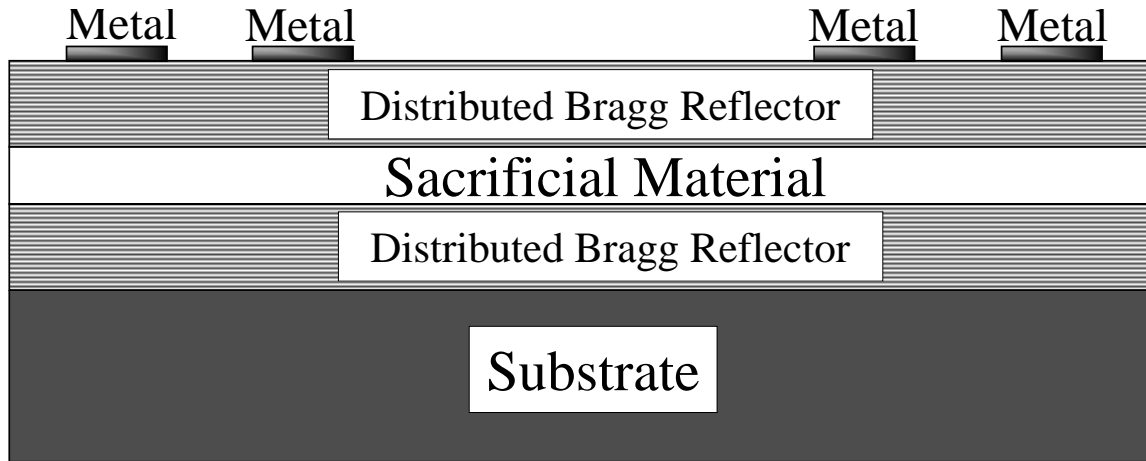


Figure 3.1 Schematic of my process after the metal deposition step.

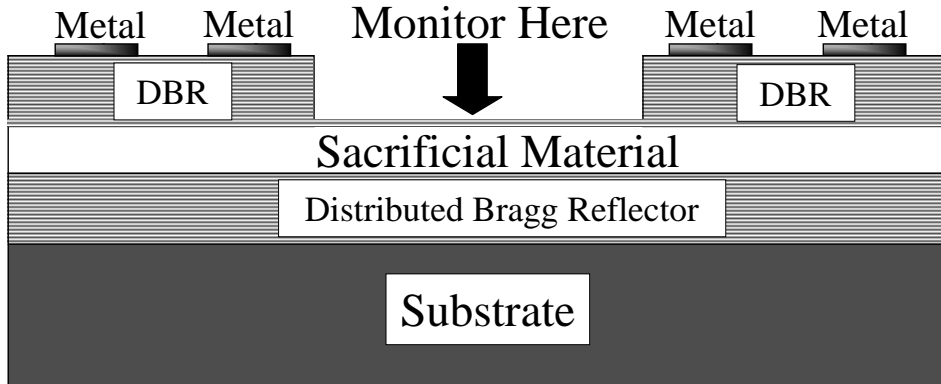


Figure 3.2 Schematic of a Fabry-Perot etalon after DBR removal, prior to mesa definition.

The result depicted in Figure 3.2 is achieved by masking the sample, except for the region to be removed, with photoresist and performing an RIE step. The etch is optically monitored to ensure the correct penetration depth.

3.2.3 Mesa Etch. The final processing step is the definition of features by performing a mesa etch. I accomplish this by masking the shapes of the features with photoresist and performing another RIE step. The etch is again optically monitored to ensure proper penetration. The finished result should look similar to the example shown in Figure 3.3.

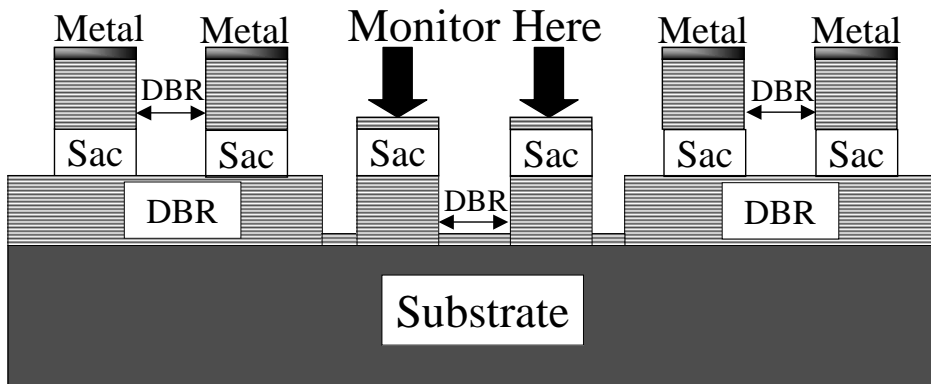


Figure 3.3 Schematic of a study structure after mesa definition and prior to selective oxidation of AlAs or selective etching of GaAs.

3.3 Mask Design

3.3.1 *Structures for Etch Studies.* The basic shape used to determine etch rates and selectivity is a circular mesa. This structure can be used to determine selectivity by observing the squaring of edges that were originally round. This phenomenon is displayed in Figure 3.4

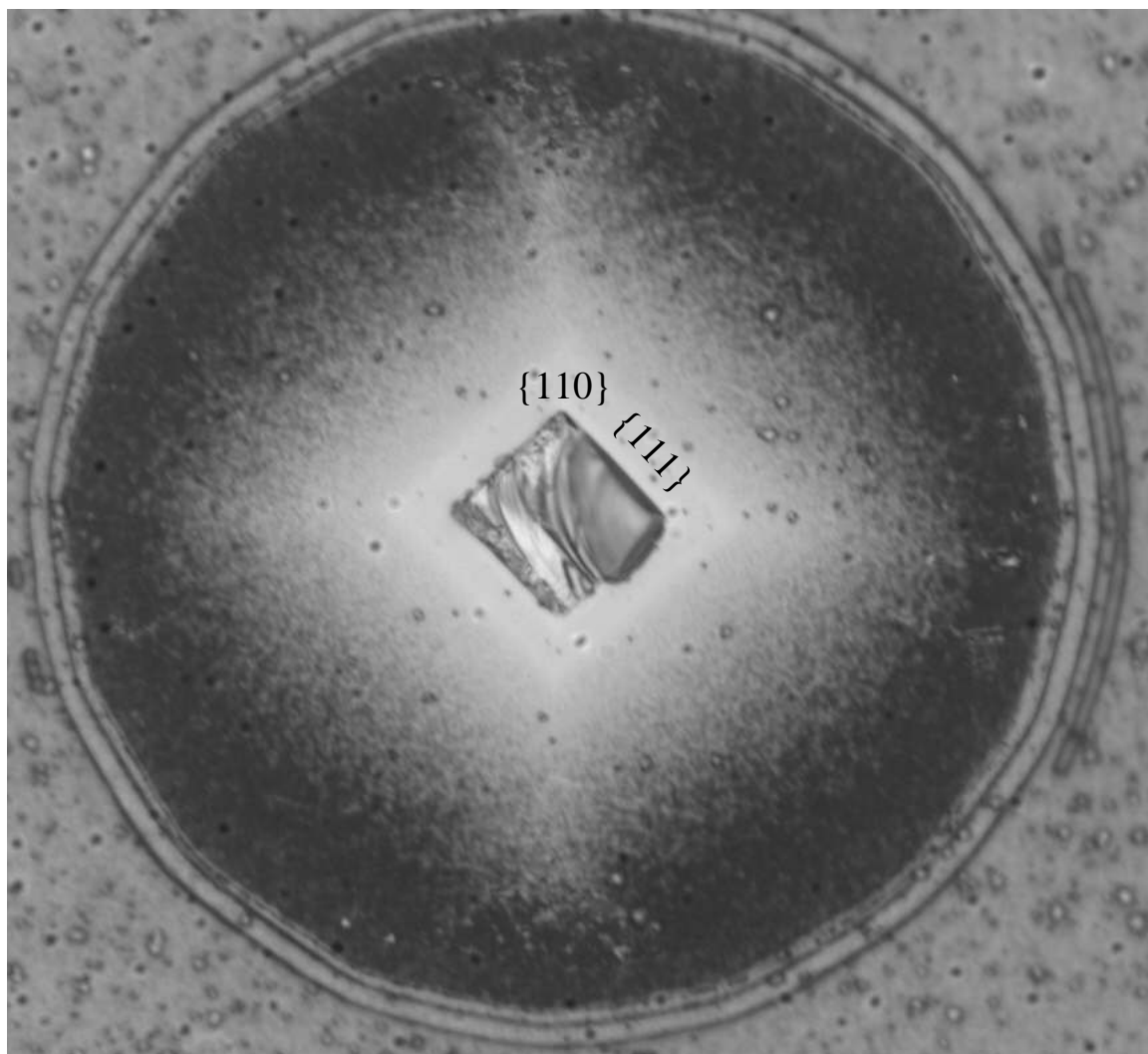


Figure 3.4 Crystal plane selectivity evidenced by the square pattern left after etching from a structure that was initially round. The structural layer was mechanically removed from the top to show this behavior in the sacrificial layer.

A second shape used to determine etch rates and crystal plane selectivity is the square. Squares were also turned at a 45° angle to determine selectivity. The diamonds resulting from turning a square 45° are not, however, aligned with the planes of a zincblende crystal such as GaAs. Therefore, I also placed a rhombus on my mask with two angles of 54.74° to further investigate crystal plane selectivity. This crystal plane aligned rhombus is illustrated in Figure 3.5.

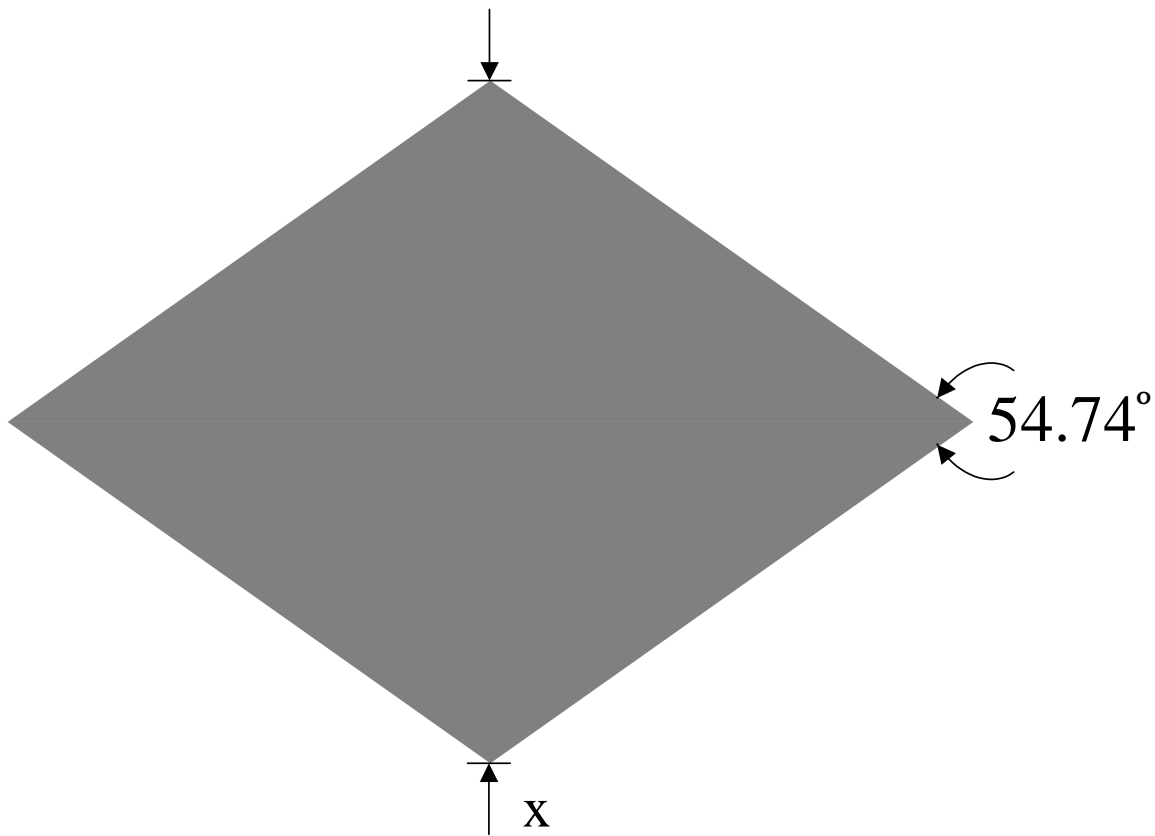


Figure 3.5 Mask pattern aligned to GaAs crystal planes for etch studies. These shapes were placed at several different orientations relative to the wafer to determine which would accelerate etching or oxidation and which would inhibit etching or oxidation.

In order to determine etch rates, it is useful to have structures of several different sizes present on the sample. Dimensions, unless otherwise noted, indicate the diameter of the circles, the length of each side for the squares, and the shortest distance between two vertices for the crystal plane aligned rhombi (top to bottom

distance (x) as shown in Figure 3.5). The following sizes of each structure were used: 1, 2, 3, 4, 5, 6, 7, 8, 9, 10, 12, 14, 16, 18, 20, 22.5, 25, 27.5, 30, 33, 36, 39, 42, 45, 45, 50, 55, 60, 65, 70, 75, 80, 85, 90, 95, 100, 105, 110, 115, 120, 125, 130, 140, 150, 175, and 200 μm . The arrays of each type of structure were arranged together on the mask in groups like the one illustrated in Figure 3.6.

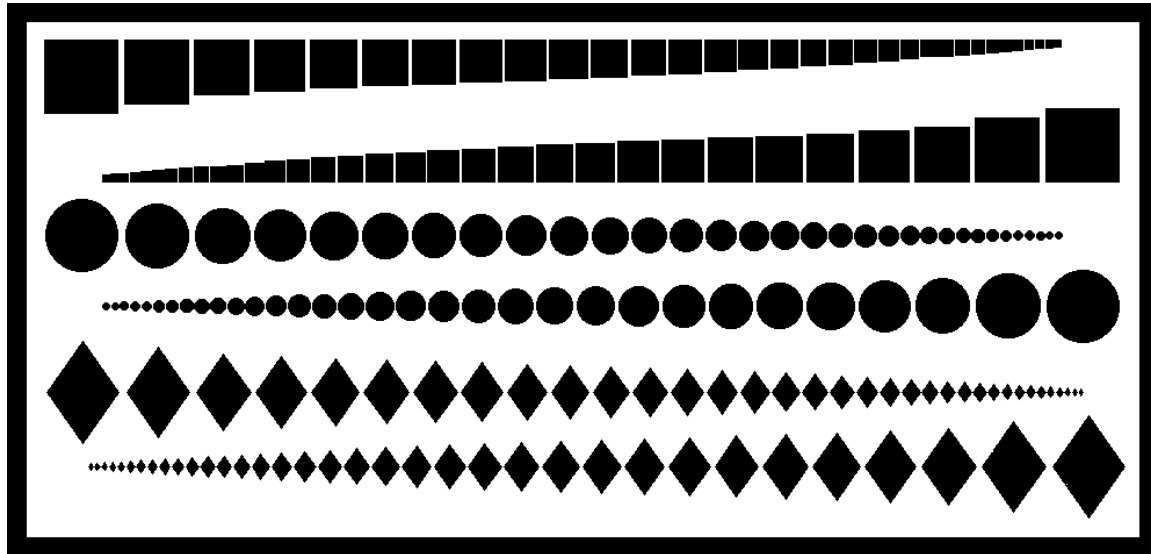


Figure 3.6 The basic mask unit containing two arrays of various sizes of each of the test shapes included in the etch study.

In order to investigate crystal plane selectivity in the various etching methods I proposed, the groups depicted in Figure 3.6 were placed at various angles relative to one another on the mask. The angles relative to the major flat(the (110) plane) are 0° , 90° , 45° , 54.74° , 35.26° (complementary angle to 54.74°), 144.74° , and 125.26° . The layout of this mask is depicted in Figure 3.7. Another feature included in the mask unit shown in Figure 3.7 is a comb resonator (based on [3]) oriented at various angles. The right triangular structures are arrays of beams fixed at both ends with lengths from 200 μm to 900 μm and a uniform width of 10 μm . Both of these structures enable the exploration of structural material properties after the sacrificial layer is removed. Other solid blocks are in place to protect metal labels placed during an earlier step.

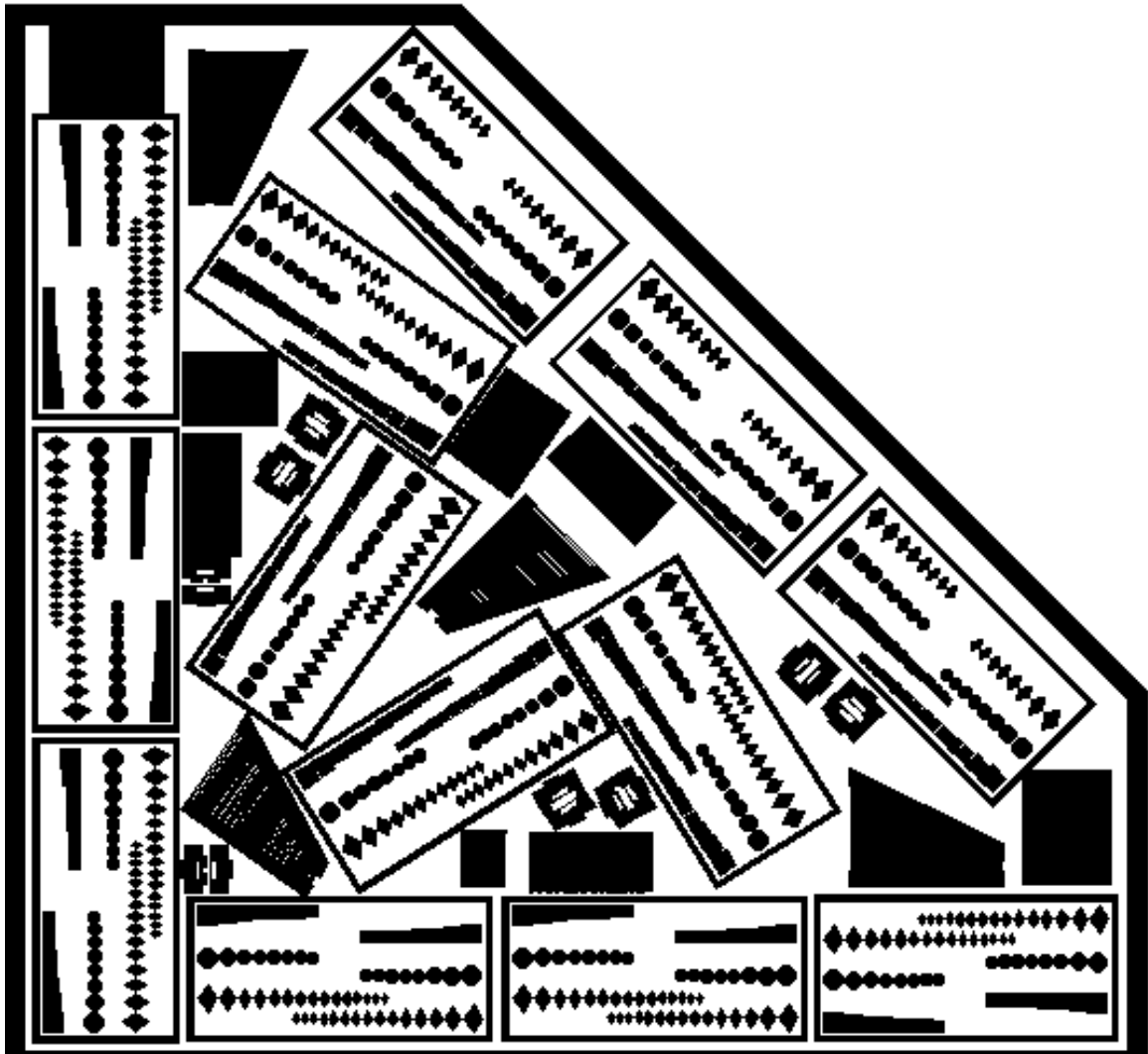


Figure 3.7 Mask reticle for the basic etch studies. Includes features shown in Figure 3.6 arranged at various angles.

3.3.2 Tunable Fabry-Perot Filters. The designs I used to fabricate tunable Fabry-Perot filters were basically composites of the shapes investigated in the etch study. Connecting these shapes with a cantilever yields a structure that can be electrostatically actuated as described in Section 2.2.2. A model of simple circular base with a circular mirror structure is depicted in Figure 3.8. My structures all included a second large pad the same size the structure's base and coated with metal to allow electrical contact without interfering with the cantilever's operation.

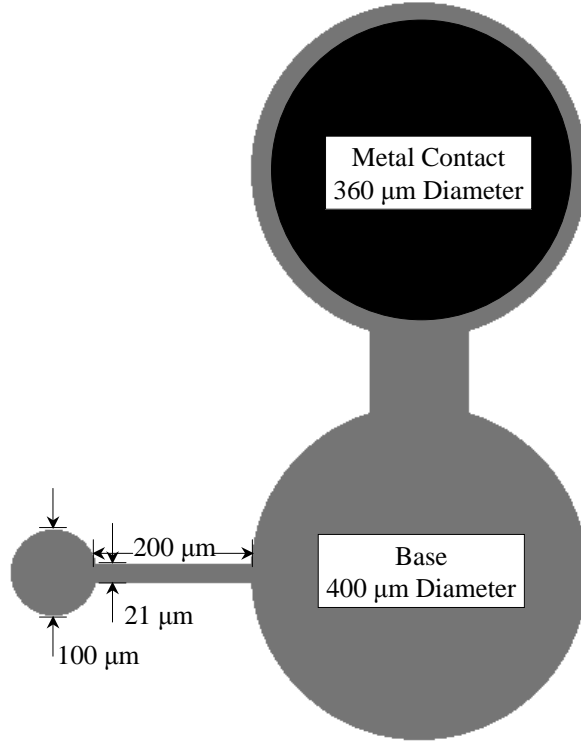


Figure 3.8 Mask layout of one of my basic circle base, circle mirror structures.

The mirror is a circle with a diameter of $100\text{ }\mu\text{m}$ and the base and contacts are circles with diameters of $400\text{ }\mu\text{m}$. I also designed structures where the circles are replaced by squares ($100\text{ }\mu\text{m}$ and $400\text{ }\mu\text{m}$ on a side), diamonds (squares rotated by 45°), and crystal plane aligned rhombi ($100\text{ }\mu\text{m}$ and $400\text{ }\mu\text{m}$ between closest vertices). The cantilevers are all $200\text{ }\mu\text{m}$ long and $21\text{ }\mu\text{m}$ wide, and the bridges between the contacts and bases are all $116\text{ }\mu\text{m}$ wide and $98\text{ }\mu\text{m}$ long. The meaning of these dimensions is obvious for the case where a cantilever or bridge interfaces with

a square, but the measurement is less straightforward when a circle or diamond is considered. The length of the cantilevers is measured as depicted in Figure 3.9 for circles, 45° diamonds, and crystal plane aligned rhombi.

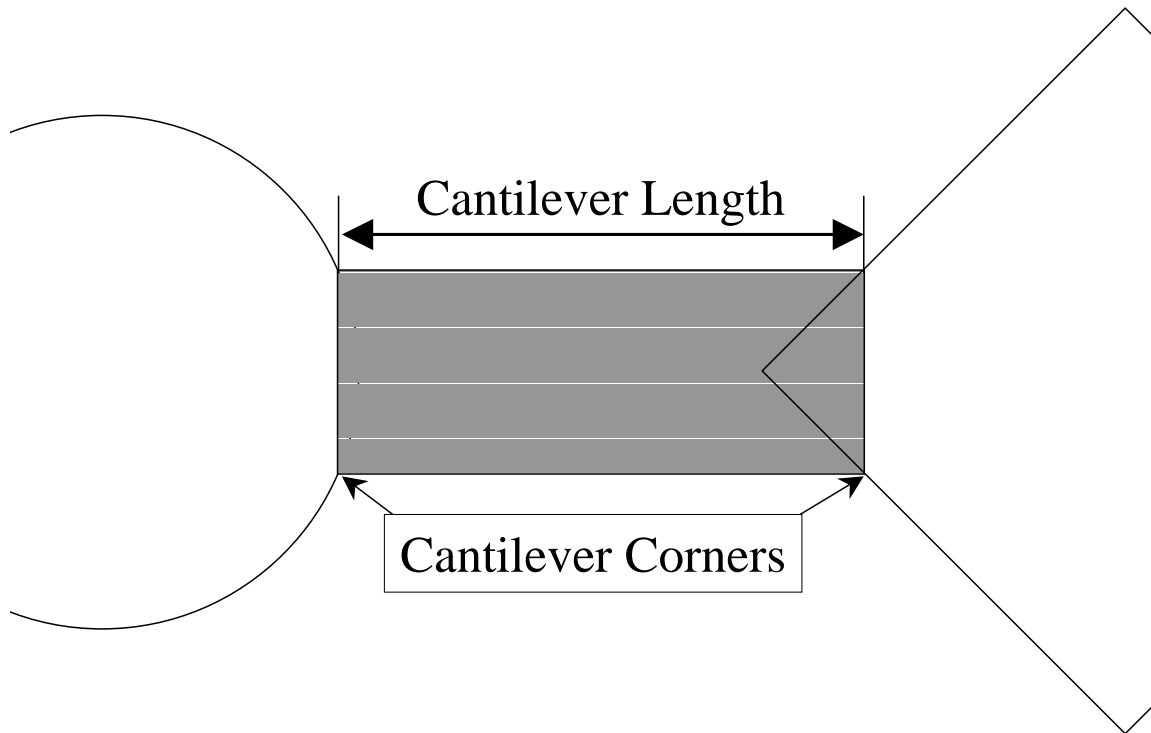


Figure 3.9 The standard used for measuring cantilevers that connect to circles or diamonds. The measurement is taken from the point where both corners of the rectangular cantilever make contact with the edge of the base or mirror.

All possible combinations of bases and mirrors achieved using the simple structures I used for the etch study are listed with a brief comment telling whether or not they were used in Table 3.1. The structures that were not used were omitted because they offer no crystal plane selectivity advantages since the base and the mirror are the same shape or approximately the same shape in the case of the diamond and rhombus combination. The resulting mask group is depicted in Figure 3.10.

Table 3.1 Combinations of base and mirror shapes for studies of MEM-tunable Fabry-Perot interferometers.

Base Shape	Mirror Shape	Used for Investigation
Circle	Circle	Not Used
Circle	Square	Used
Circle	45° Diamond	Used
Circle	Rhombus	Used
Square	Circle	Used
Square	Square	Not Used
Square	45° Diamond	Used
Square	Rhombus	Used
45° Diamond	Circle	Used
45° Diamond	Square	Used
45° Diamond	45° Diamond	Not Used
45° Diamond	Rhombus	Not Used
Rhombus	Circle	Used
Rhombus	Square	Used
Rhombus	45° Diamond	Not Used
Rhombus	Rhombus	Not Used

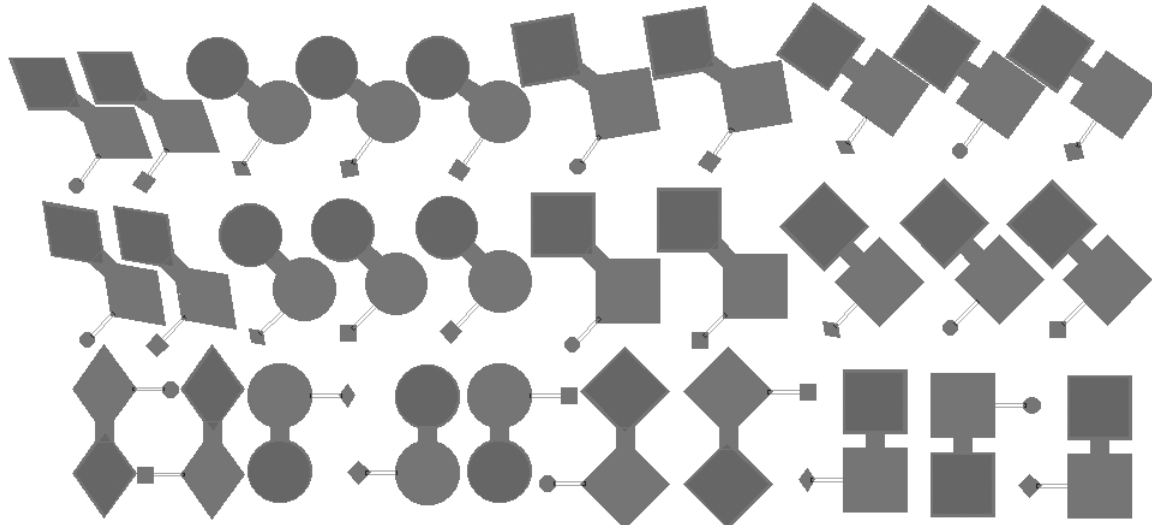


Figure 3.10 Layout of the structures investigated while fabricating a tunable Fabry-Perot filter. The features are placed at angles of 45° and 54.74° relative to the bottom row in an attempt to take advantage of crystal plane selectivity.

The purpose of investigating crystal plane selectivity in the etch or oxidation process is to determine the optimal method to leave as much of the sacrificial material as possible under the base and contact while completely removing it from underneath the mirror and the cantilever. This is the underlying determination of which combinations from Table 3.1 were used. The premise is that if the mirror and the base are the same shape, they will etch at the same rate, so there is no advantage. The arrays of structures shown in Figure 3.10 were also arranged at right angles to each other in order to investigate crystal plane selectivity at complementary angles.

Also included in my mask layout for tunable Fabry-Perot interferometers are piston actuated moveable mirrors. These structures operate using the same principles of electrostatic attraction as the cantilevers. An example layout for a piston mirror is illustrated in Figure 3.11.

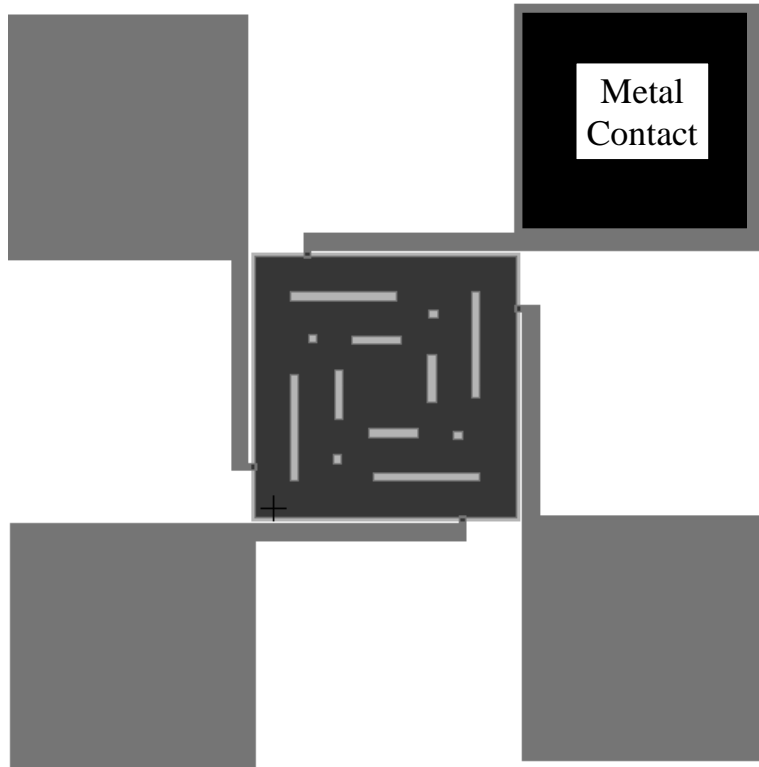


Figure 3.11 Example layout of a piston mirror [5].

Because these piston mirrors are supported on all four sides they move straight up and down instead of forming an angle with the substrate. This mode of operation should yield better performance as an interferometer because the distance between the two DBRs is uniform across their surfaces. The reader should note that the designs for these piston mirrors are not original work, but came from designs fabricated and tested in polysilicon [5].

The mask reticle with cantilever and piston actuated interferometers, etch monitoring dropouts, material property test structures, and a gold standard for use as a reference during optical measurements, is depicted in Figure 3.12.

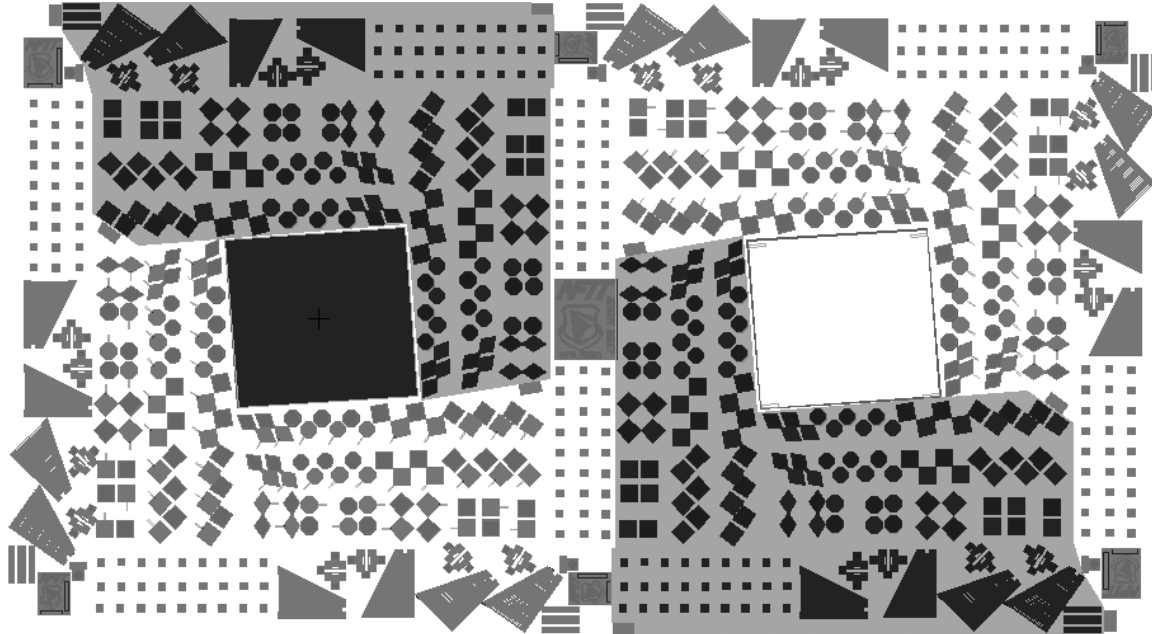


Figure 3.12 Unit of the mask used to define tunable Fabry-Perot interferometer structures. Shaded areas indicate regions where the top DBR will be removed to allow for in-situ monitoring during the selective oxidation of AlAs or $\text{Al}_{0.98}\text{Ga}_{0.02}\text{As}$ sacrificial layers.

3.4 Selective Etch Studies

3.4.1 Etch Study Material. The etch study processes that I attempted were based on the selective removal of GaAs from an $\text{Al}_x\text{Ga}_{1-x}\text{As}$ structure or the removal of AlAs from an $\text{Al}_x\text{Ga}_{1-x}\text{As}$ structure. One first approach to this etch study is to have a sample grown by molecular beam epitaxy (MBE) with a relatively thick layer of the intended sacrificial material between layers of $\text{Al}_x\text{Ga}_{1-x}\text{As}$. This, of course, could be made in the form of a Fabry-Perot etalon, where the sacrificial material comprises the microcavity. An example structure for general selective etching studies is shown in Figure 3.13.

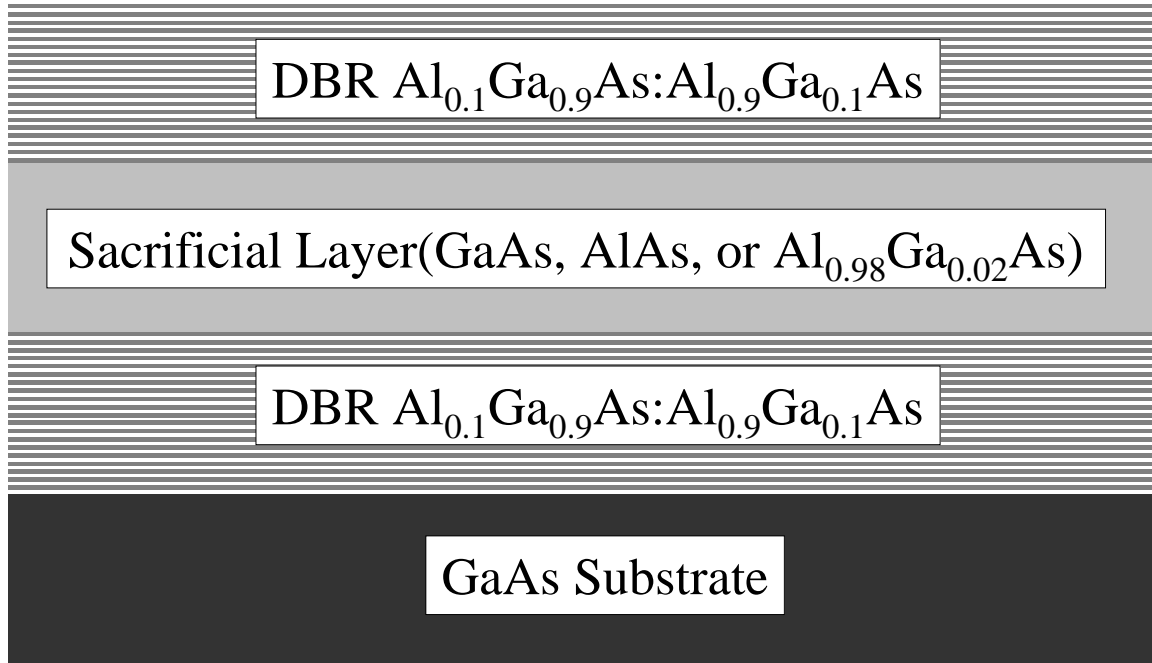


Figure 3.13 Schematic of a general epitaxial growth consisting of a sacrificial layer between two DBRs.

3.4.2 Dry Etch Study Experimental Procedure. The exact details of the procedure I followed are given in Appendix A.1, but a general overview is presented here. Initially, I coated the wafers with a relatively thick positive photoresist (1818 at 2.1 μm) and patterned the resist into arrays of circles. The mask used to create

these circles is not the same mask discussed in Section 3.3.1, rather it is an array of only circles of the following diameters: 1.5, 2, 3, 4, 5, 6, 8, 10, 12, 14, 16, 18, 20, 25, 35, 50, and 100 μm . Some of the mesas from this mask are pictured in Figure 3.14.

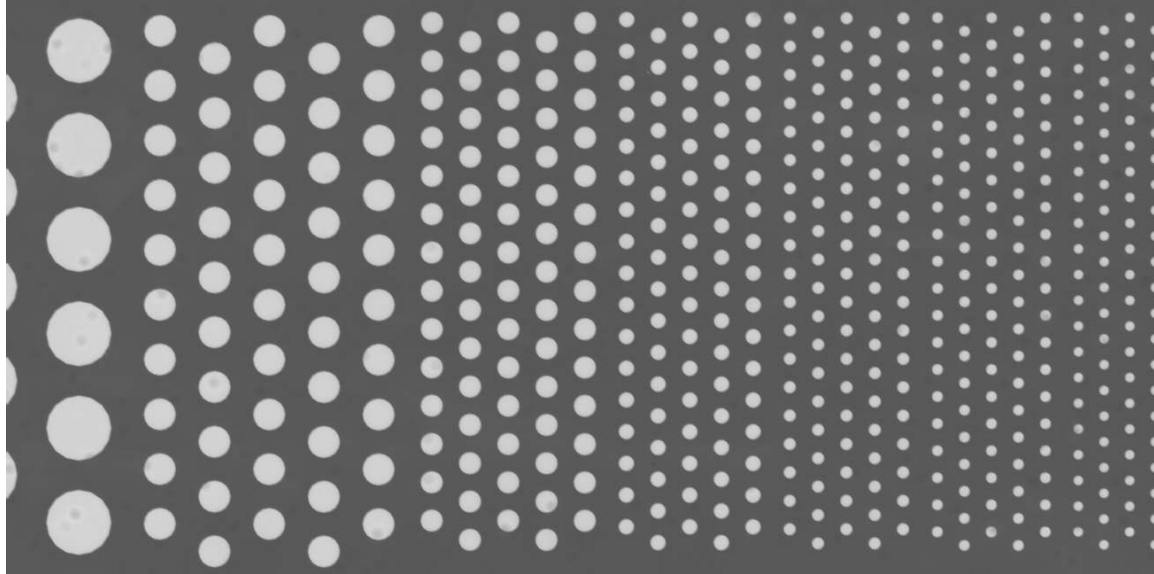


Figure 3.14 Photograph of the mask used to define circular mesas for dry and wet etch studies. Circle sizes shown are 16, 18, 20, 25, 35, 50, and 100 μm .

Following the lithographic patterning, the samples were placed in the inductively coupled plasma (ICP) etcher and etched until the mesas extended through the top DBR and sacrificial layer(s) and slightly into the bottom DBR. The etch depth was controlled by monitoring the reflectance from the samples illuminated with a laser diode operating at 789 nm, and comparing the values with those obtained through previous mathematical modelling of the sample structure [6]. A sample reflectance measurement plot and its corresponding modelled plot are depicted in Figure 3.15.

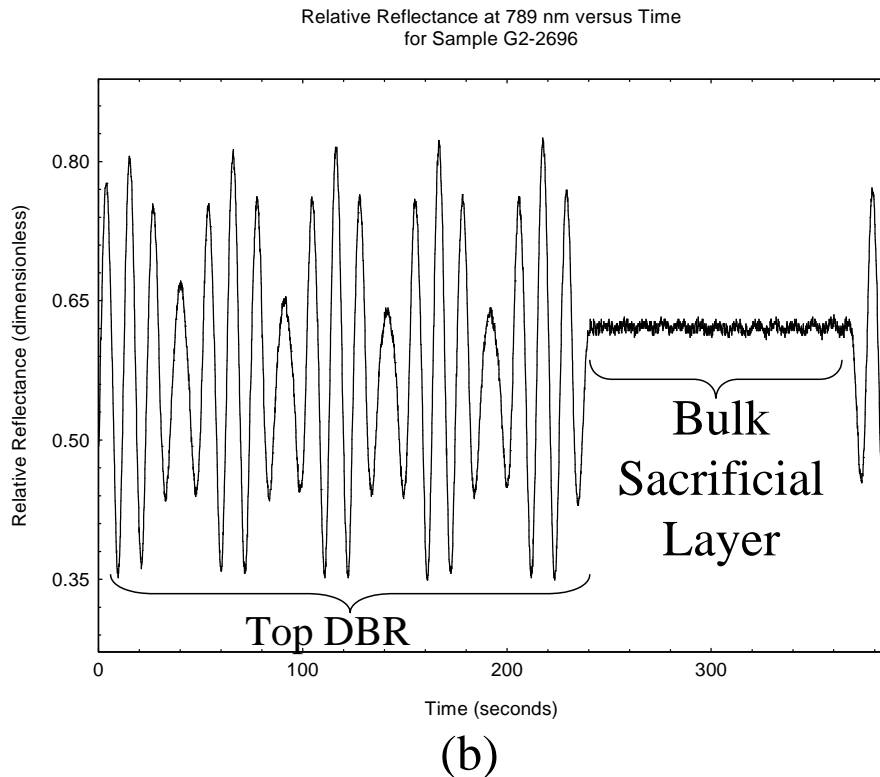
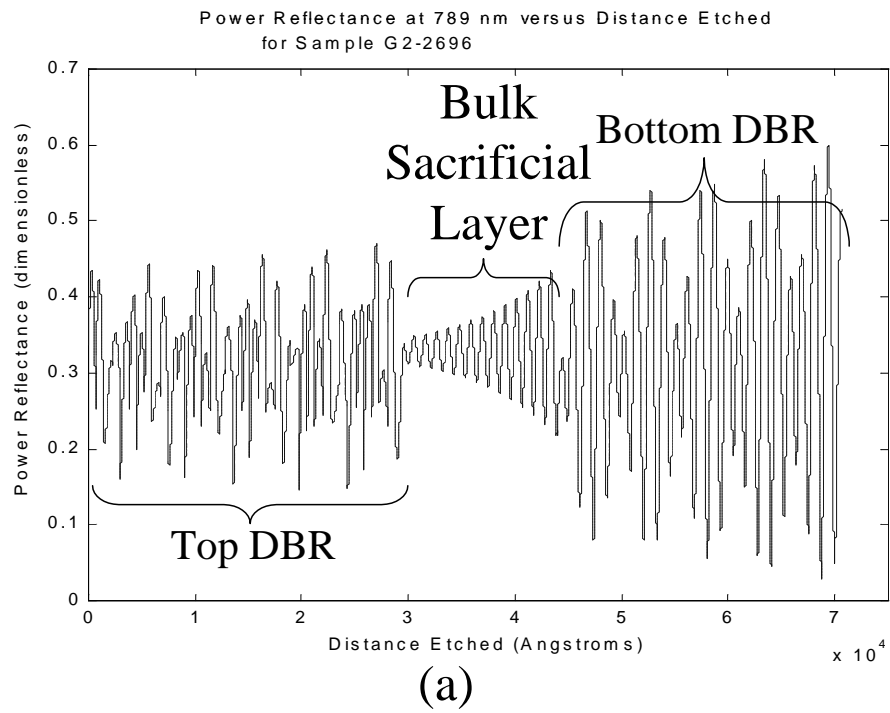


Figure 3.15 Plot of power reflectance at 789 nm as material is etched away. (a) Calculated power reflectance at normal incidence versus distance etched from original top surface. (b) Measured power reflectance versus etch time at near normal incidence. Structural information for the growth referenced in this figure is available in Appendix B.

After defining mesas, the sample was cleaned and prepared for the selective etch. Another layer of photoresist (1818 at 2.1 μm thick) was placed on the sample and patterned with the same mask depicted in Figure 3.14. This ensures that the directional nature of the ensuing etch in the RIE chamber will not damage the top surface of the sample. Immediately prior to the selective etch, the sample was immersed in a solution of hydrochloric acid (HCl):isopropanol at a ratio of 1:10 for 30 seconds. This step removes native oxide that may have formed on the sample and inhibits etching by preventing reactive species from getting to the unoxidized semiconductor beneath it. The sample was then placed in the RIE chamber for ten minutes under the conditions listed in Table 3.2.

Table 3.2 Conditions for the intial dry etch for selective removal of GaAs [7].

RF Power	50 Watts
Chamber Pressure	50 mTorr
BCl_3 Flow Rate	2.5 sccm
SF_6 Flow Rate	7.5 sccm
Temperature	20 °C

The rest of the etch study was planned according to the parameters given in Table 3.3.

3.4.3 Wet Etch Study for Selective GaAs Removal: Experimental Procedure.

The exact process followed during my wet etch study for the selective removal of GaAs is contained in the processing recipe shown in Appendix A.2. The wet etch experiment was conducted using the samples patterned for the dry etch experiment as described in Section 3.4.2. The samples were cleaved into small pieces in order to conserve material. For ease of handling, I mounted these small sample pieces to microscope slides using Crystal Bond 509. Crystal Bond 509 is a thermal wax that melts at approximately 120 °C and hardens at lower temperatures. It is easily removed with acetone and does not damage semiconductor surfaces. After mounting

Table 3.3 Etch parameters for the dry etch study [7].

Order	BCl ₃ Flow (sccm)	SF ₆ Flow (sccm)	RIE Power (Watts)	Pressure (mTorr)	Temp (°C)/ Time(min)
5	2.5	6.5	40	30	20 °C/10 min
7	2.5	6.5	40	70	20 °C/10 min
1	2.5	6.5	60	30	20 °C/10 min
3	2.5	6.5	60	70	20 °C/10 min
6	2.5	8.5	40	30	20 °C/10 min
4	2.5	8.5	40	70	20 °C/10 min
8	2.5	8.5	60	30	20 °C/10 min
2	2.5	8.5	60	70	20 °C/10 min

to microscope slides, I cleaned the samples with acetone, methanol, and isopropanol to ensure removal of the excess crystal bond 509 and any other residues that may have been present. The samples were placed in an oxygen plasma cleaning system with a forward RF power of 200 W and a gas flow rate of 500 sccm at 2 Torr for a period of 12 minutes to ensure complete removal of organic residues. I included this step because of the tendency for photoresist to passivate the sidewalls of mesa structures during reactive ion etching. Finally, I dipped the samples in a solution of buffered oxide etch (BOE):distilled water mixed at a ratio of 1:7 for 60 seconds and gently agitated the solution by moving the dipping basket back and forth. The samples were now ready for etching as described below.

These samples were immersed in a mixture of 0.5 molar (M) C₆H₈O₇:0.5 M K₃C₇H₅O₂:H₂O₂ (30%) at a volume ratio of 10:10:3. I chose these concentrations and ratios based upon the successful transistor fabrication reported by Chang et al. [2]. After the desired etch time had been reached, I placed the sample in a Deionized Water (DIW) rinse tank for three, 30-second cycles to stop the etch. Following this, I dried the samples with nitrogen gas and made my observations.

3.4.4 Oxidation Etch Study: Experimental Procedure. Another scheme for releasing structures is to selectively oxidize a sacrificial layer and then remove that oxide. The details of my study of the conversion of AlAs to Al_xO_y so that it could be selectively removed are contained in Appendix A.3.

The samples were first metallized using the process detailed in Section 2.6. As discussed in Section 3.3.1, the metal was placed in the areas where the shapes under study would eventually be defined. An image of the metallized sample is shown in Figure 3.16.

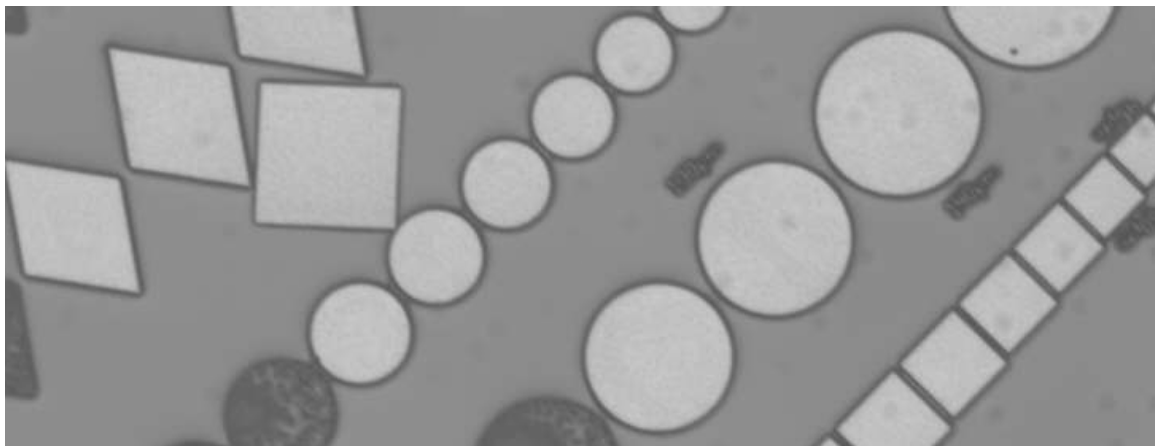


Figure 3.16 Image of metal deposited on etch study structures for the oxidation etch study.

In order to allow for in-situ monitoring of the samples during oxidation, all but 2-4 of the DBR layers above the sacrificial layer were removed in selected areas. I used reactive ion etching for this removal process. Obviously, this procedure would spoil optical devices that rely on a top DBR, so only selected areas were etched in this manner. This step was only necessary for structures with DBRs above the sacrificial layer since bulk AlGaAs is generally transparent to infrared.

Another RIE step was used to define the mesa structures. This etch was allowed to progress well beyond the sacrificial layer. The result was a mesa with

the sacrificial layer exposed on all sides. The shapes of the mesas are depicted in Figure 3.6.

The structures were then oxidized. For the etch study, I performed the oxidation at a temperature of 400 °C and at a pressure of 5 Torr with a DIW vapor flow rate of 500 sccm.

3.5 III-V MOEMS Applications

The etch studies detailed above were undertaken to gather useful data about the selective removal of III-V materials. In this section, I discuss some of the applications made possible by my etch studies. Of particular interest are devices which have properties that are desirable both optically and mechanically.

3.5.1 Tunable Fabry-Perot Interferometer. As discussed in Section 2.10.2, the resonant wavelength of a Fabry-Perot etalon can be tuned by adjusting the distance between the two mirrors. The fabrication details are given in Appendix A.4, but the most important points are included here. Beginning with an epitaxial growth like the one depicted in Figure 3.17, I placed metal contacts on the sample and patterned it using RIE to end up with structures similar to those pictured in Figure 3.18. Only the upper DBR and the sacrificial material were patterned during the RIE step.

After metallization and patterning, I placed the structures immediately into a solution of $C_6H_8O_7:K_3C_7H_5O_2:H_2O_2$ at a ratio of 10:10:3 for a period of 4 hours and 35 minutes. This allowed for selective removal of the GaAs without significant damage to the $Al_xGa_{1-x}As$ DBRs surrounding it. The lower DBR was left in place in order to protect the GaAs substrate from the selective etchant. A released structure is pictured in Figure 3.19.

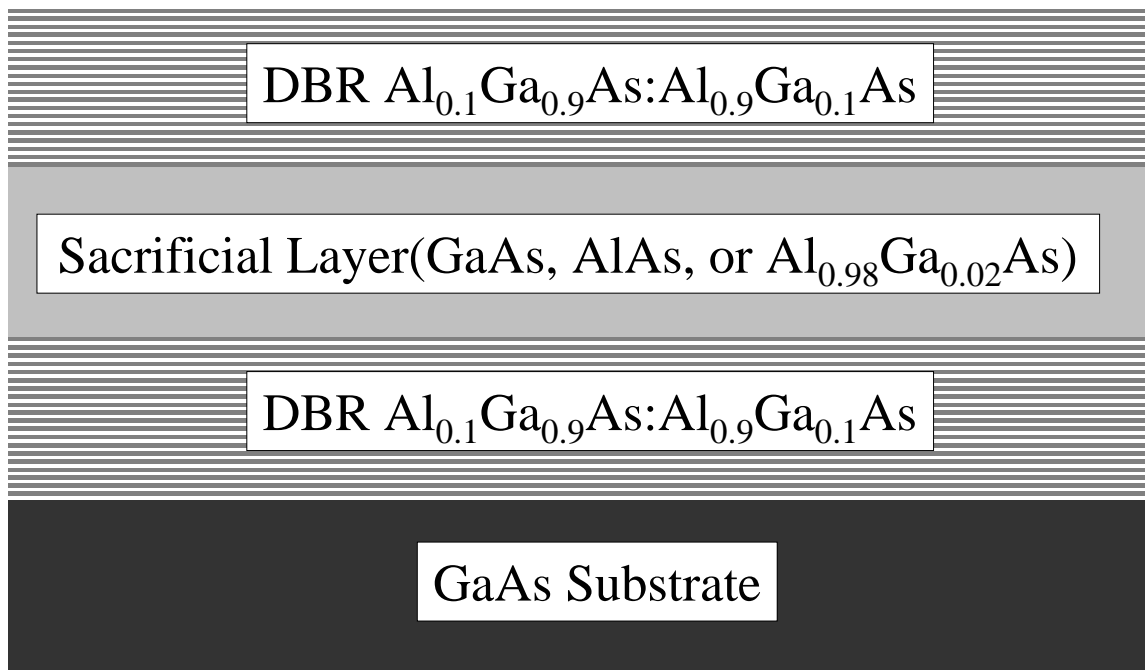


Figure 3.17 Schematic of an epitaxial growth consisting of a sacrificial layer between two DBRs.

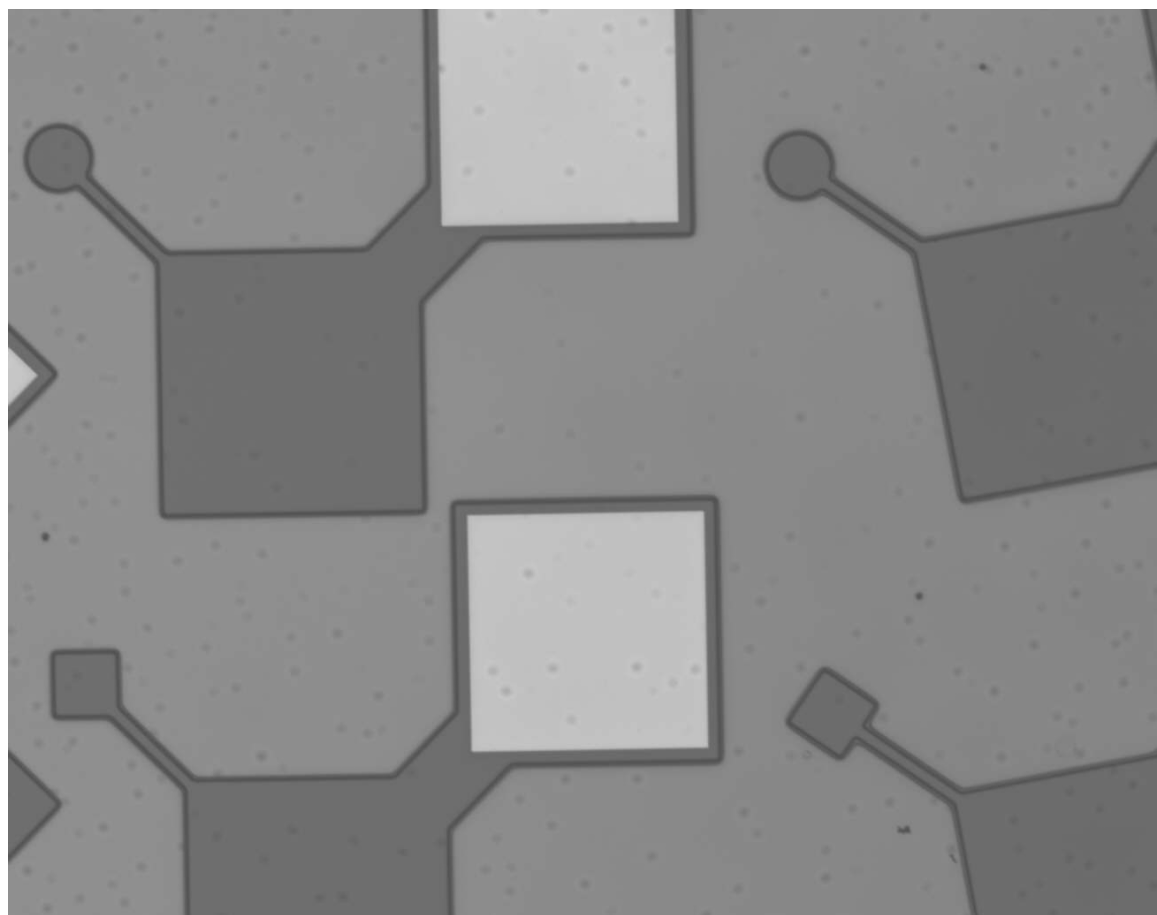


Figure 3.18 Image of tunable Fabry-Perot structures before the sacrificial layer release etch.

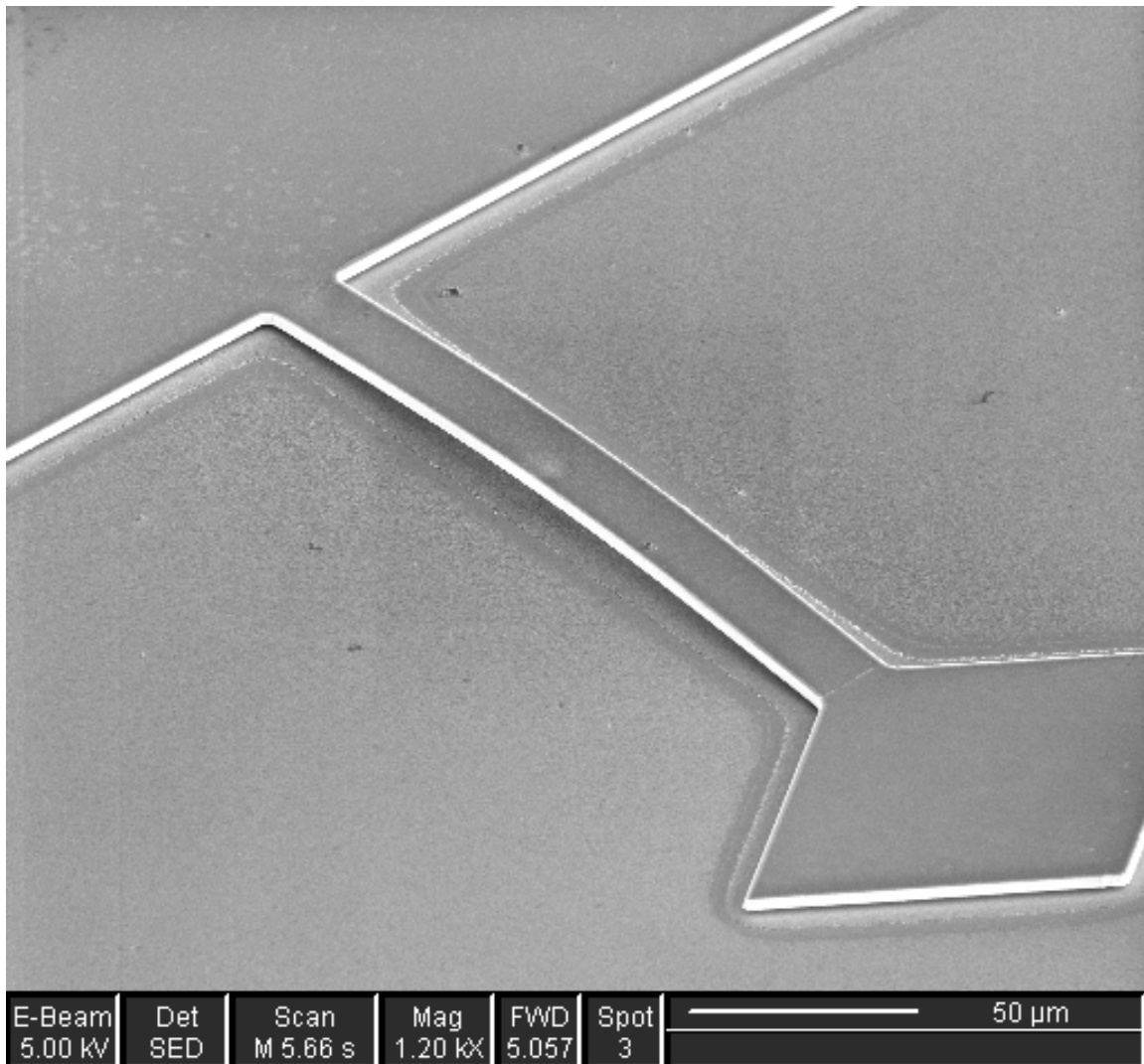


Figure 3.19 Image of a MEM-tunable Fabry-Perot etalon after the release etch. This device was produced using sample G2-2747 (see Appendix B for detailed structure).

I also investigated a second method of of sacrificial layer removal wherein I used a sacrificial layer of $\text{Al}_{0.98}\text{Ga}_{0.02}\text{As}$ converted to $\text{Al}_x\text{Ga}_y\text{O}_z$ by steam oxidation. I selectively removed the oxide using a solution of potassium hydroxide (KOH) 1.0 M in DIW at a ratio of 1:12 [4].

After immersion in the liquid etchant to remove GaAs or $\text{Al}_x\text{Ga}_y\text{O}_z$ the etch was stopped with methanol. The samples then remained immersed in methanol until they could be dried using supercritical CO_2 as described in Section 2.9.3.

3.5.2 Lift-off Optical Devices. Another application of this selective etch technology is the transplantation of optical devices such as VCSELs or RCLEDs. The details of my lift-off process implementation can be found in Appendix A.5. In order to transplant devices, the entire device must be grown on top of a sacrificial layer. An example of such a structure is illustrated in Figure 3.20.

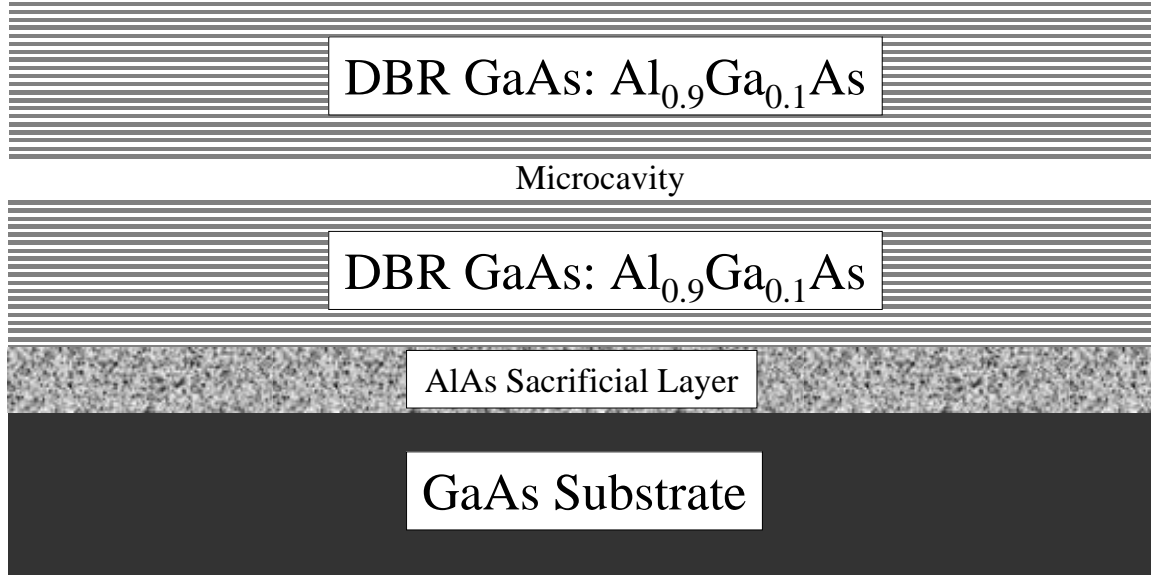


Figure 3.20 Example of an epitaxial growth for the purpose of fabricating lift-off microcavity light-emitting devices.

The material depicted in Figure 3.20 can be grown to emit from the top DBR or the substrate. In order to activate the top-up devices, I needed to remove them from their substrate and place them on a new substrate in the same top-up orientation.

To process the microcavity light-emitting devices, metal is first placed in ring patterns on the top DBRs by lift-off patterning. Next, mesas are formed by RIE, resulting in an array shown for example in Figure 3.21. The mesa definition etch for

a normal VCSEL need only go past the active region in the microcavity, but for these structures the mesa etch was timed to go completely through both DBRs and the sacrificial layer beneath, barely into the substrate. At this point, the top-emitting devices are tested by placing the sample on a grounded metal chuck and using a probe to apply a voltage to the ring contact atop the device.

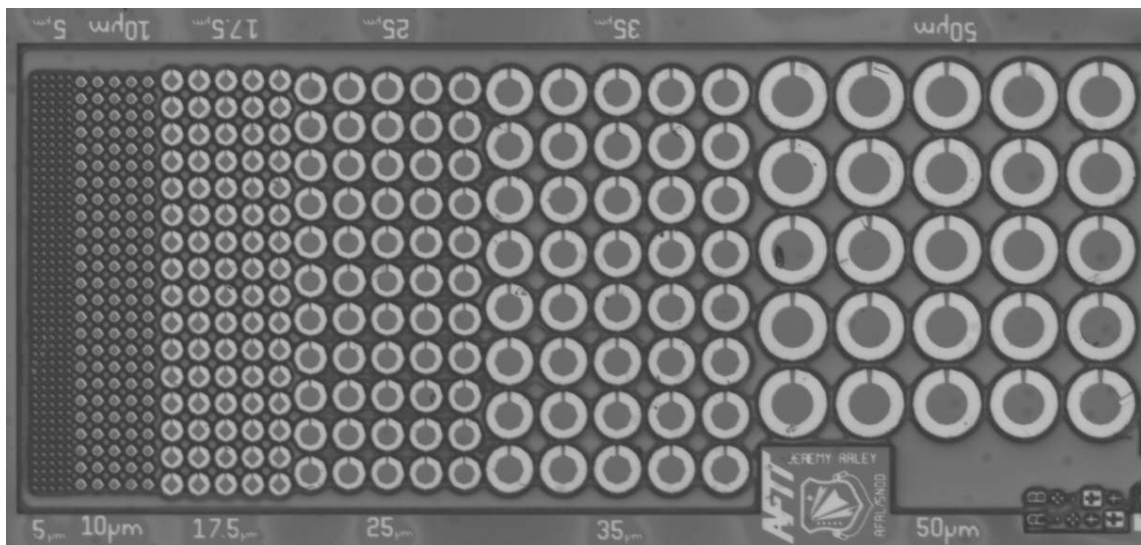


Figure 3.21 An array of optical devices after metal deposition and mesa definition.

I investigated two methods of releasing devices from their native substrates: (1) direct selective etching of AlAs, and (2) oxidation of AlAs followed by oxide removal.

To oxidize the AlAs, I placed the sample depicted in Figure 3.21 in the oxidation system described in Section 2.8. In order to transplant the devices, a metallized, three-inch silicon wafer, was placed in a solution of KOH(1.0 M):DIW 1:12. In order to release the devices, the oxidized sample was held over the acceptor substrate in this solution for a period of 10 minutes with occasional agitation.

For the direct removal of AlAs to release devices, I used hydrofluoric acid:DIW at a 1:1 mixture, as well as a more dilute hydrofluoric acid:isopropyl alcohol(ISP):DIW

1:3:6 mixture [1]. To release the optical devices, I placed the metallized silicon substrate in the etching solution and then held the array of lift-off devices above it for a period of 60 seconds for the HF:DIW 1:1 mixture or 44 minutes for the HF:ISP:DIW 1:3:6 solution.

Following the release etch, the silicon substrate was removed from the etching solution and rinsed in DIW, for both cases. To dry the sample, I placed the silicon wafer on a hot plate at 110°C until there was no longer any water visible. To test the devices that were successfully transplanted, I placed a probe on individual metal contact rings and another probe on the metallized silicon blank.

3.6 Conclusions

This chapter presents the details of the experiments I undertook to study the selective etching of GaAs, AlAs and $\text{Al}_{0.98}\text{Ga}_{0.02}\text{As}$. I also present the fabrication methodology used to make tunable Fabry-Perot filters and lift-off microcavity optical devices. The methods presented here are straightforward. The basic premise of all of my fabrication techniques was to place metal contacts, define a shape using RIE, and then release a structure using a selective etch. While the basic procedure is simple, the details involved in actually performing these tasks in a repeatable manner were quite complex.

Bibliography

1. Blum-Spahn, O., "Private Communication." Research Scientist, Sandia National Laboratories, NM. January 2002.
2. Chang, H.-C., Chang, E. Y., Chung, C.-C., and Kuo, C. T. "Highly Selective GaAs/Al_{0.2}Ga_{0.8}As Wet Etch Process for the Gate Recess of Low-Voltage-Power Pseudomorphic High-Electron-Mobility Transistor," *Japanese Journal of Applied Physics, Part 1*, 39(8):4699–4703 (2000).
3. Hjort, K. "Gallium Arsenide as a Mechanical Material," *Journal of Micromechanics and Microengineering*, 4(1):1–13 (March 1994).
4. Naone, R. L. and Coldren, L. A. "Tapered Air Apertures for Thermally Robust VCL Structures," *IEEE Photonics Technology Letters*, 11(11):1339–1341 (November 1999).
5. Ochoa, E. M., "Private Communication." Ph. D. Candidate, Air Force Institute of Technology, Department of Electrical and Computer Engineering, Wright-Patterson AFB, OH. 2 November 2001.
6. Ochoa, E. M., "oeng775tools: A MATLAB® Toolbox." AFIT/ENG, Wright-Patterson AFB, OH, Unpublished, February 2001.
7. Weston, D., "Private Communication." Air Force Reserve Researcher, Air Force Research Laboratory, Sensors Directorate, Wright-Patterson AFB, OH. 18 September 2001.

IV. Results and Analysis

4.1 Introduction

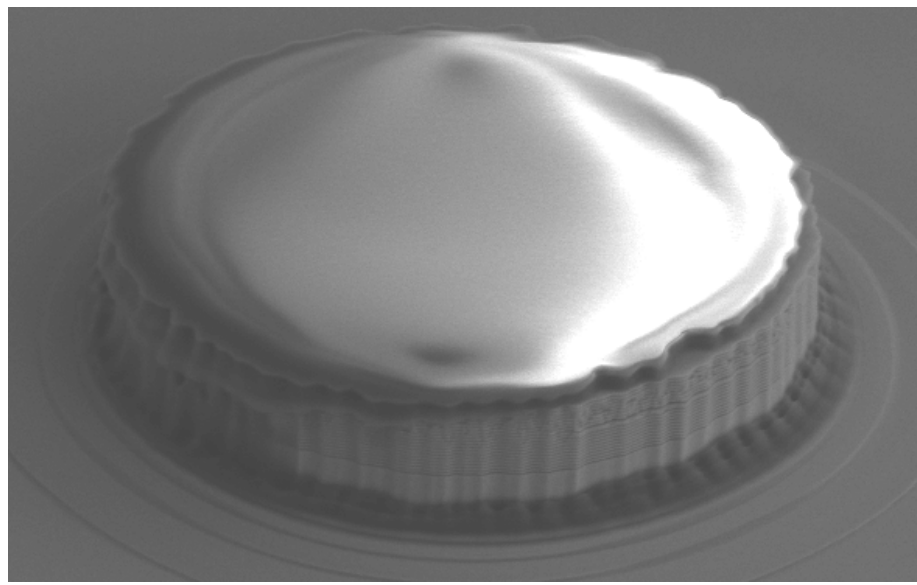
In this chapter, I present the results of the processing work detailed in Chapter III. First, I present results from the dry etch study that was attempted. I then present results from the etch studies I performed using both AlAs converted to Al_xO_y and GaAs as sacrificial layers. Finally, I present the results of my fabrication efforts to produce MEM-tunable Fabry-Perot filters and lift-off light-emitting microcavity devices.

4.2 Dry Etch Study

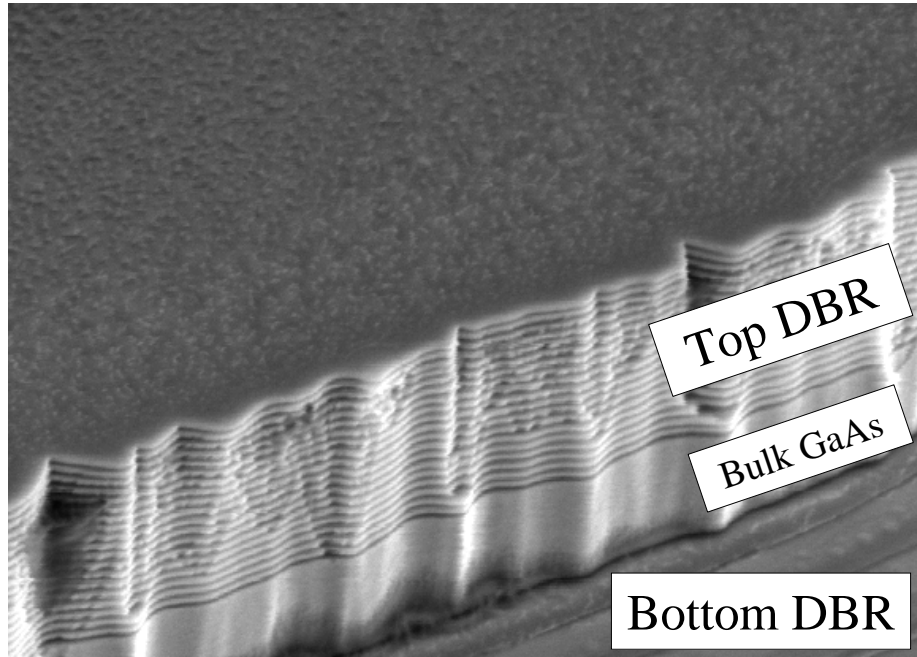
The dry etch study produced no important results. Although others have used the method presented in Section 3.4.2 to selectively remove GaAs from $\text{Al}_x\text{Ga}_{1-x}\text{As}$ epitaxial layers [2], the result of my attempt to characterize this dry etch was that no etching occurred. In Figure 4.1, I show SEM images of a mesa structure before and after the selective etch. This image makes it clear that the bulk sacrificial material between the DBRs has not been affected by the attempted etch. The only conclusion I can draw from this result is that the etch is ineffective given the conditions under which I attempted it.

4.3 Wet Etch Study for Selective GaAs Removal

The selective removal of GaAs using $\text{C}_6\text{H}_8\text{O}_7(0.5 \text{ M}):\text{K}_3\text{C}_7\text{H}_5\text{O}_2(0.5 \text{ M}):\text{H}_2\text{O}_2(30\%)$ 10:10:3 was highly effective. Figure 4.2 shows the results after the selective removal of a bulk GaAs layer placed between two DBRs consisting of alternating layers of $\text{Al}_{0.1}\text{Ga}_{0.9}\text{As}$ and $\text{Al}_{0.9}\text{Ga}_{0.1}\text{As}$. In order to assist in determining how far the etch progressed and the selectivity exhibited, part of the structure was removed using a focused ion beam (FIB) system. The FIB system removes material in an area defined by the operator which produces the milling effect seen in Figure 4.2.

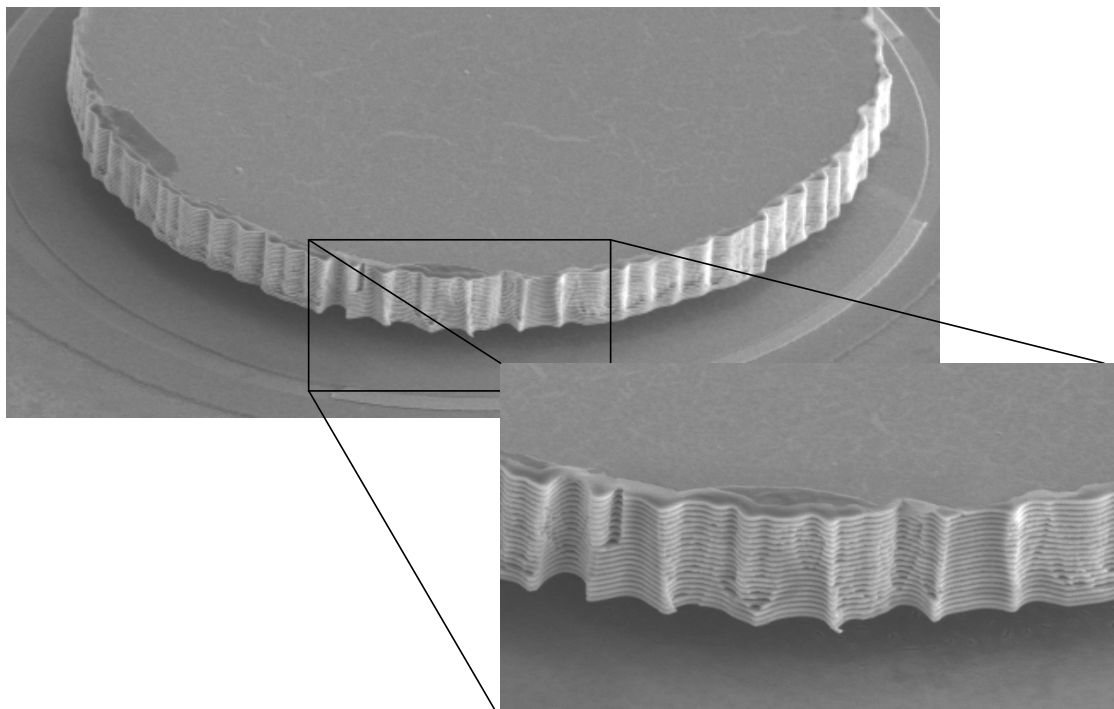


(a)

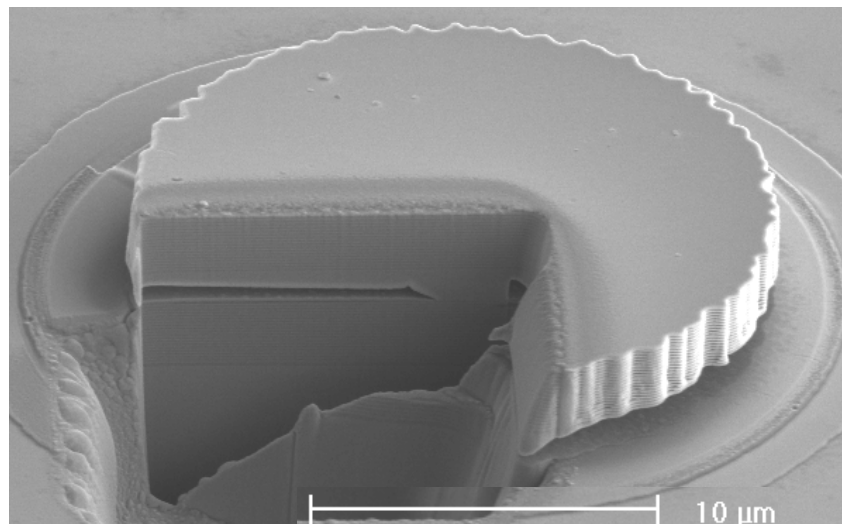


(b)

Figure 4.1 SEM images of test structures after a dry etch. (a) Image taken after initial RIE mesa definition. There is still a layer of photoresist atop the structure to protect it from any directional etching that might happen during the selective dry etch. (b) Image taken after exposure to BCl_3 and SF_6 to selectively remove GaAs. The image is magnified so that it is clear that the GaAs layer (the bulk material visible just above the bottom DBR layers where the mesa etch was stopped) has not been etched.



(a)



(b)

Figure 4.2 Image of a sample processed from wafer G2-2696 where bulk GaAs has been selectively removed from between two DBRs. (a) Missing material is apparent from an angled view of the structure. (b) The structure was milled using a focused ion beam (FIB) system in order to look inside the layers and make the selective removal more apparent. Note that undulating edges were caused by mask degradation during RIE.

4.3.1 Etch Rate Characterization. As stated in Section 3.4.3 and detailed in Appendix A.2, I characterized the etch rate of the $\text{C}_6\text{H}_8\text{O}_7:\text{K}_3\text{C}_7\text{H}_5\text{O}_2:\text{H}_2\text{O}_2$ solution for the removal of GaAs by immersing samples in the solution for a given period of time and then observing what size of circular structure was completely undercut. Complete undercutting was determined by the release of the top portion of the structure. An example of what the sample looks like after this etch is shown in Figure 4.3.

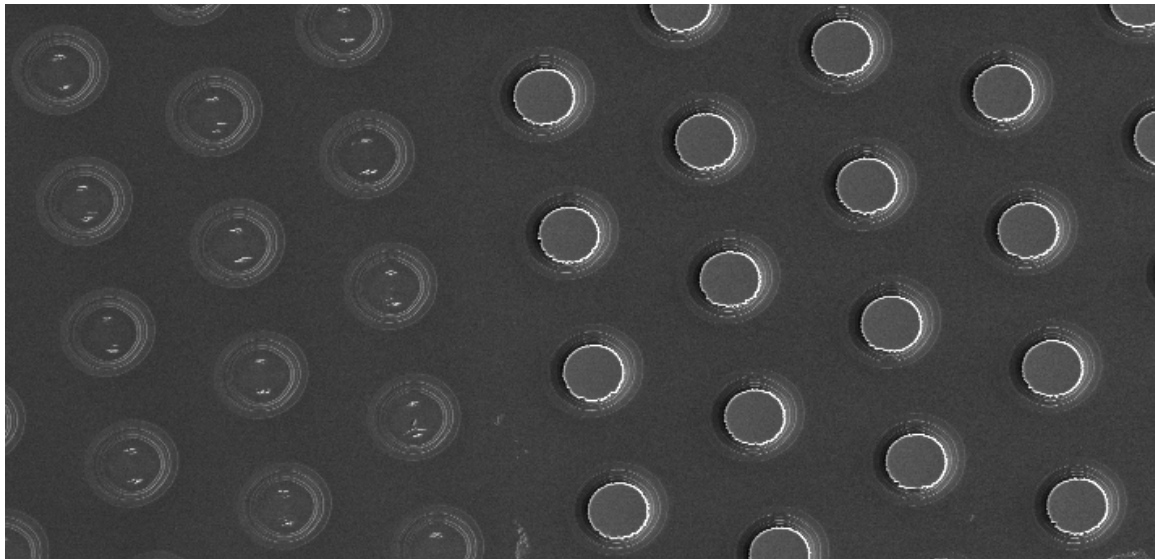


Figure 4.3 SEM image of a wafer where some of the structures have been completely undercut and others that are slightly larger still remain.

By using a microscope to note the size of the largest removed structures, I was able to determine an effective etch rate. Figure 4.4 puts this data in graphical form and gives some idea of the steady state etch rate for this system of etchants and material. Based on the data collected and illustrated in Figure 4.4, I determined the steady-state etch rate to be approximately $1 \mu\text{m}/\text{min}$.

4.3.2 Etch Selectivity Characterization.

4.3.2.1 Selectivity Between Materials. Ideally, I would have used a GaAs sacrificial layer next to a bulk layer of $\text{Al}_{0.1}\text{Ga}_{0.9}\text{As}$ to characterize the “worst-

Etch Progress versus Time in Etching Solution

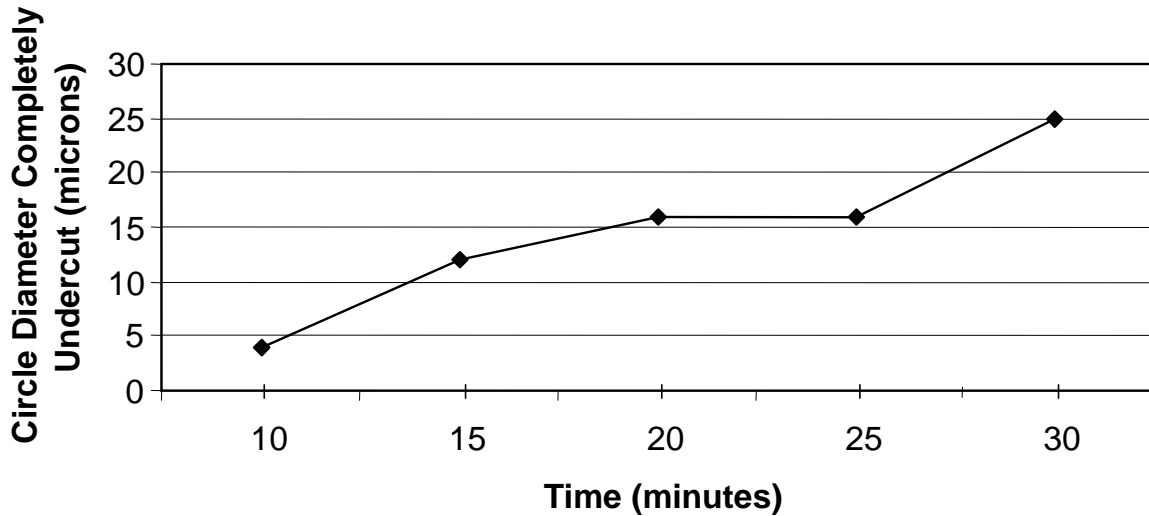


Figure 4.4 Graphical representation of the data collected during experiments to determine the etch rate of $C_6H_8O_7:K_3C_7H_5O_2:H_2O_2$ 10:10:3 on a $1.5 \mu m$ GaAs sacrificial layer.

case" etch selectivity for this etchant. Unfortunately, this combination of material was not available for study, so I characterized selectivity using material where a bulk layer of GaAs was grown between two DBRs consisting of alternating layers of $Al_{0.1}Ga_{0.9}As$ and $Al_{0.9}Ga_{0.1}As$. The layer closest to the GaAs sacrificial layer on both sides was $Al_{0.9}Ga_{0.1}As$ in all cases. To measure the selectivity of the etchant between GaAs and $Al_{0.9}Ga_{0.1}As$, I measured the diameter of the top of the study structures before and after etching and then compared the reduction in size of the upper DBR structure to the amount of GaAs removed. Even at 100x magnification, there was no discernable difference in size between the top DBR before and after etching. For practical purposes, this etch is completely selective to GaAs over $Al_{0.9}Ga_{0.1}As$. Previously reported selectivity for the case of selectively etching GaAs away from an underlying bulk layer of $Al_{0.2}Ga_{0.8}As$ is 3400:1 [1], which is practically complete selectivity for the purposes of fabricating MEMS.

By using a focused ion beam (FIB) to mill into the remaining top layer of a structure, I could make the same determination for the $Al_{0.1}Ga_{0.9}As$ layers based on

how far they were recessed from their adjacent $\text{Al}_{0.9}\text{Ga}_{0.1}\text{As}$ layer. Figure 4.5 shows how this measurement was made. This comparison is not completely valid because of the difference in thickness between the $\text{Al}_{0.1}\text{Ga}_{0.9}\text{As}$ DBR layers, which are each 70.8-nm thick, compared to the much thicker 1.5– μm thick GaAs layer. However, bearing this thickness disparity in mind, this structure shows complete selectivity for practical purposes. I believe that this result is due to the fact that the aluminum containing layers form a compound that inhibits the etch, and the proximity of the $\text{Al}_{0.9}\text{Ga}_{0.1}\text{As}$ to the $\text{Al}_{0.1}\text{Ga}_{0.9}\text{As}$ keeps the etchant from attacking the $\text{Al}_{0.1}\text{Ga}_{0.9}\text{As}$. I do not believe that this result would hold for layers of $\text{Al}_{0.1}\text{Ga}_{0.9}\text{As}$ that are thicker or not in such close proximity to $\text{Al}_{0.9}\text{Ga}_{0.1}\text{As}$.

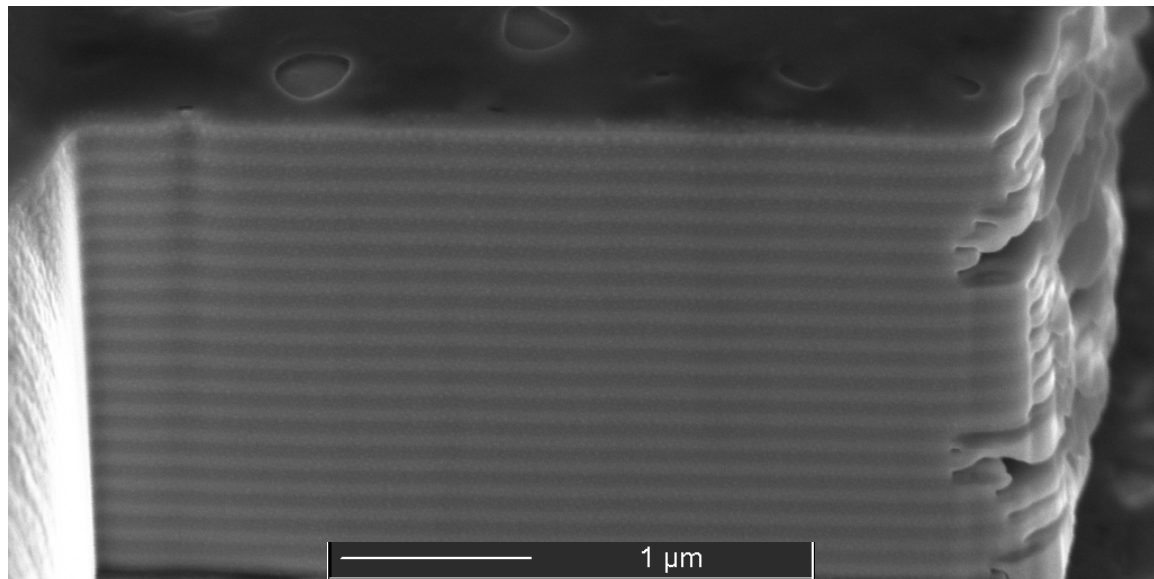


Figure 4.5 Structure where the top DBR has been milled to determine the removal rate of $\text{Al}_{0.1}\text{Ga}_{0.9}\text{As}$.

Another measure of material selectivity in this etch is the smoothness of surfaces left behind after the selective removal of GaAs . Figure 4.6 shows a DBR structure that was completely undercut and migrated across the sample. Even at 200,000x magnification, there was no discernable surface roughness on samples that were etched using this technique. The apparent roughness in some of the images

presented (Figure 4.2 b and Figure 4.9 for example) is due to material scattered by the FIB during milling operations.

Another factor affecting selectivity is agitation. In the experiments in which I agitated the solution during etching, the selectivity was reduced to about 2.5:1 for GaAs over $\text{Al}_{0.9}\text{Ga}_{0.1}\text{As}$. This effect is most likely due to the mechanical removal of hydroxyl groups that would normally protect the aluminum containing layers [1].

Finally, it should be noted that this etch combination had no noticeable effect on metal contacts. The contacts used consisted of a 200 Å-thick titanium adhesion layer beneath a 2550 Å-thick gold contact layer.

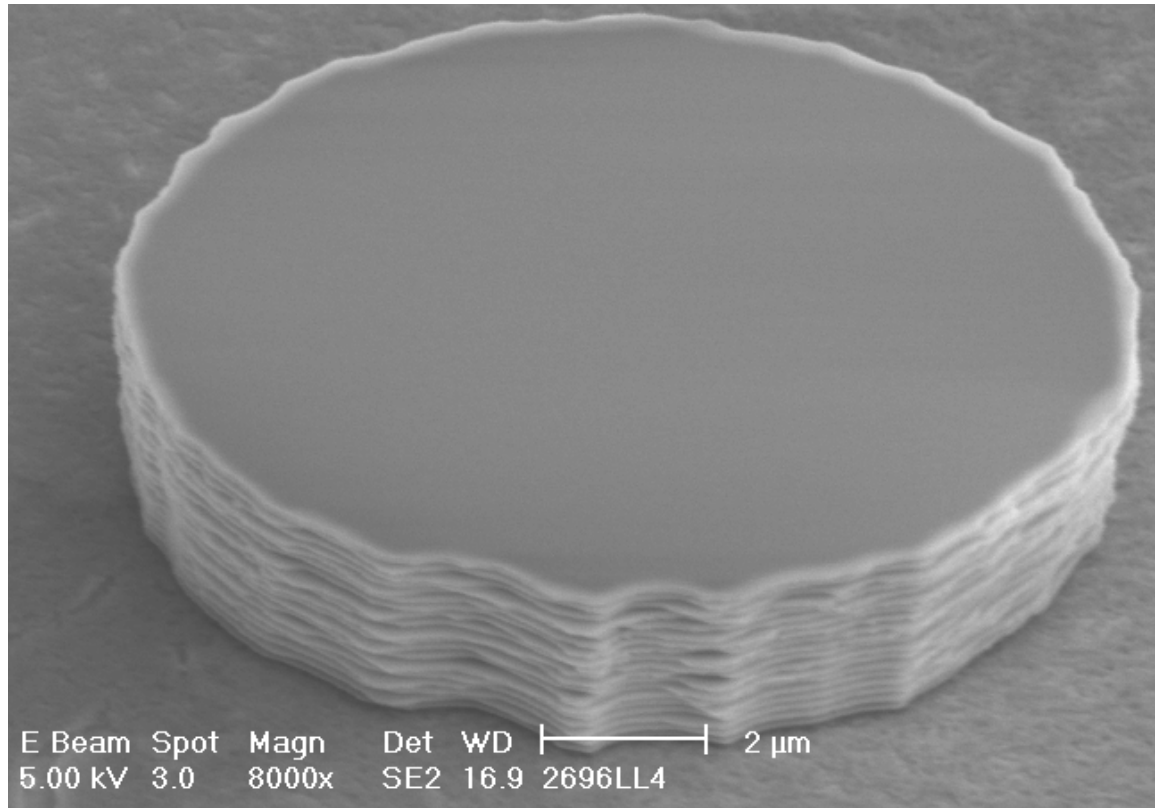


Figure 4.6 Image of an undercut and displaced DBR structure illustrating the smoothness of the top surface after the GaAs is selectively removed.

4.3.2.2 Selectivity Among Crystal Planes. The $\text{C}_6\text{H}_8\text{O}_7:\text{K}_3\text{C}_7\text{H}_5\text{O}_2:\text{H}_2\text{O}_2$ 10:10:3 solution also showed crystal plane selectivity when removing GaAs. The first

evidence of this behavior is the fact that when I performed an etch on material that had been patterned in a circle, the resulting pattern of the sacrificial GaAs was a rhombus aligned along the $\{110\}$ crystal planes. This effect is depicted in Figure 4.7.

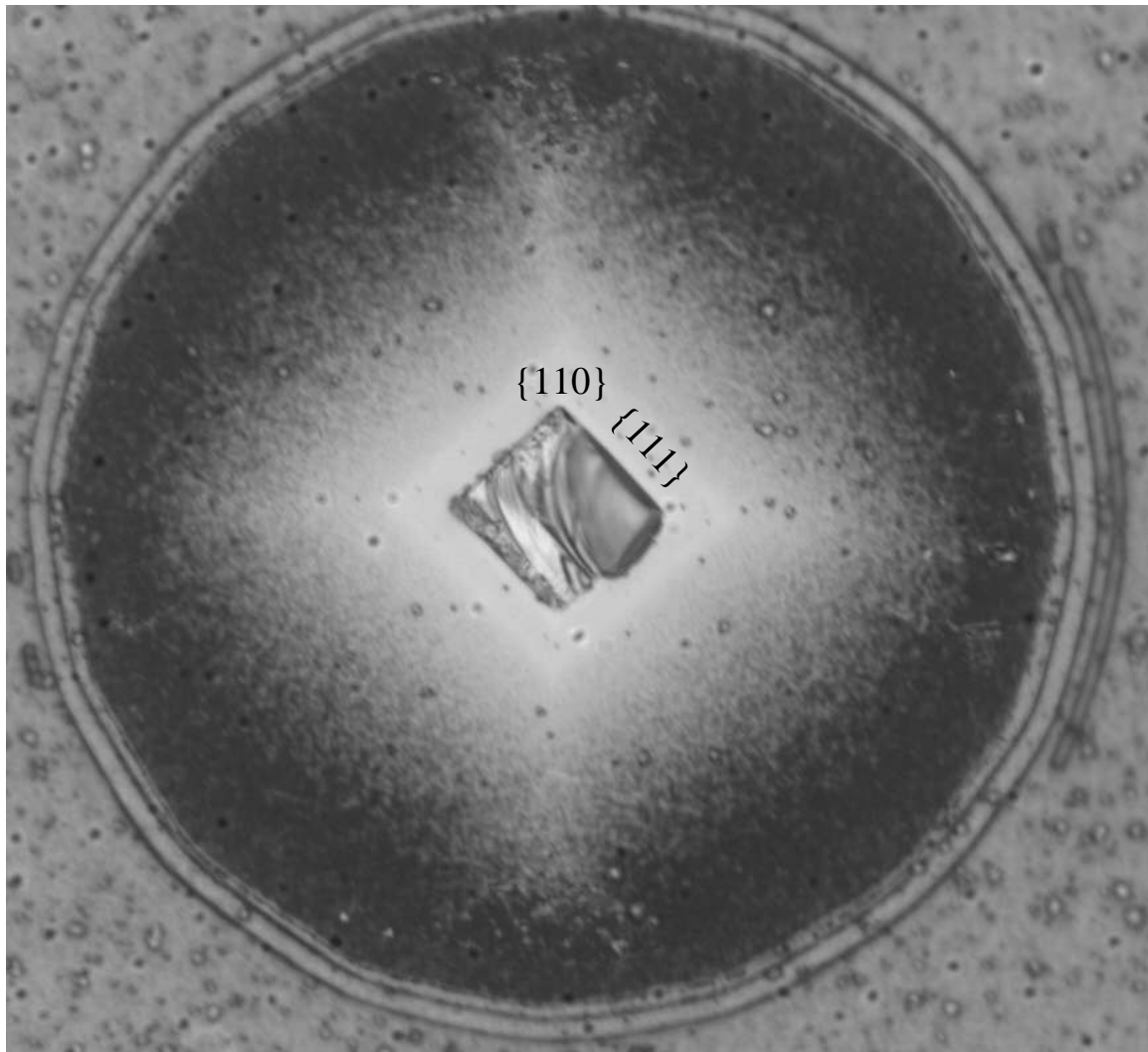


Figure 4.7 Image illustrating crystal plane selectivity by virtue of the fact that the sacrificial GaAs started patterned as a circle and ended up patterned as a diamond.

From Figure 4.7, I could tell that this etchant tends to etch most slowly along the $\{110\}$ planes. I further quantified this by patterning material with the arrays of structures discussed in Section 3.3.1. Such an array is depicted below in Figure 4.8.

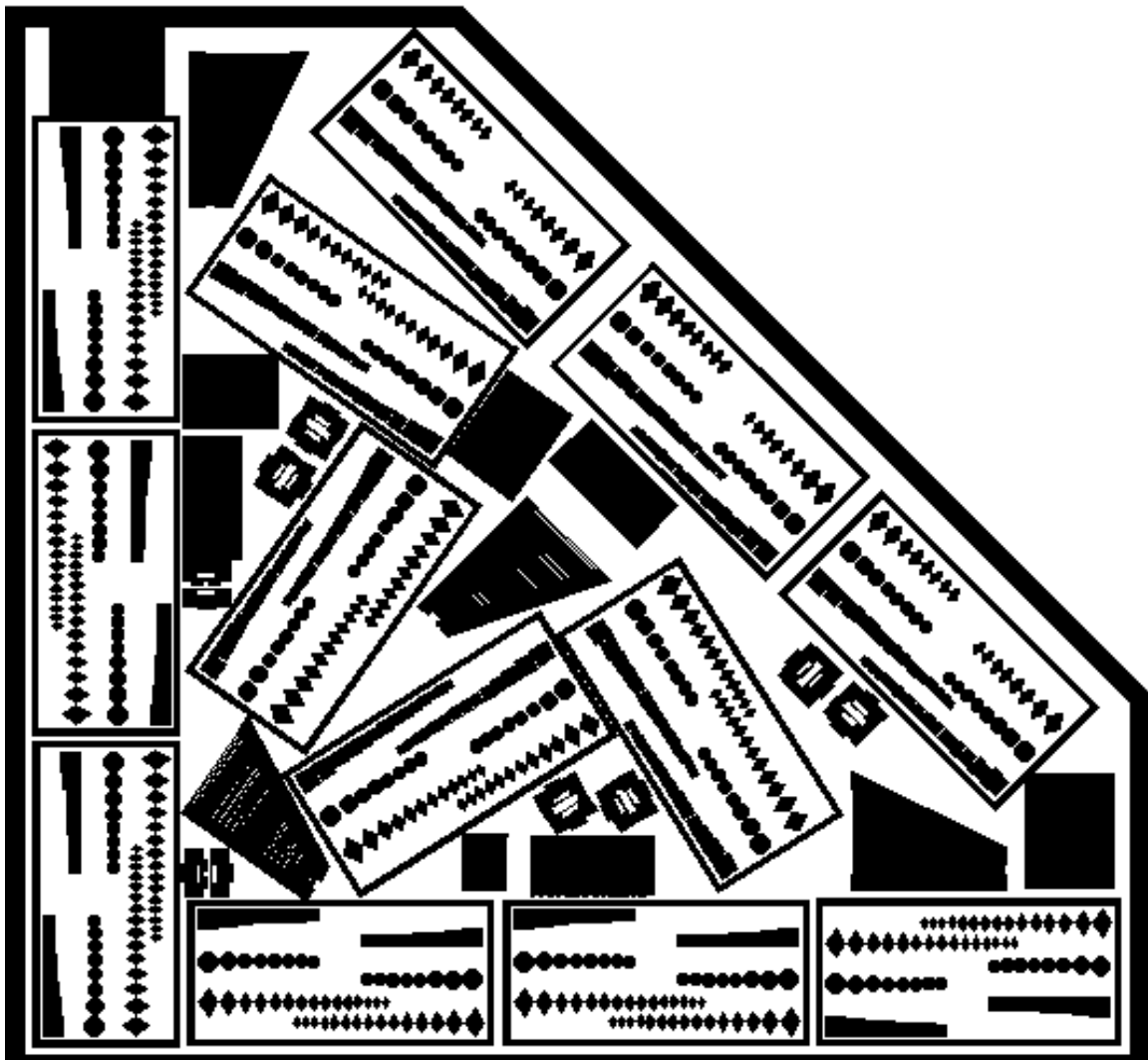


Figure 4.8 Image of an array of structures used to study crystal plane selectivity for GaAs etched with citric acid: $K_3C_7H_5O_2$: H_2O_2 . The structural layer was mechanically removed from the top to show this behavior in the sacrificial layer.

After a period of 55 minutes in the etchant, various sizes of structures had fallen onto the bottom DBR based on their shape and orientation on the wafer. Table 4.1 presents the data concerning how quickly the various shapes and orientations etched relative to one another. The etch rates were again characterized by microscope observation of the maximum feature size removed.

Table 4.1 Data collected for groups of 4 structures from a single sample after 55 minutes in etching solution concerning the etch progress for several shapes at various crystal plane orientations for selective removal of GaAs.

Shape	Angle Relative to Major Flat (110)	Maximum Feature Size Removed (μm)	Rate (μm/min)
Circle	0°	30	0.55
Square	0°	12	0.22
Rhombus	0°	45	0.82
Circle	-35.26°	18	0.33
Square	-35.26°	39	0.71
Rhombus	-35.26°	25	0.45
Circle	35.26°	14	0.25
Square	35.26°	39	0.71
Rhombus	35.26°	9	0.16
Circle	45°	27.5	0.50
Square	45°	45	0.82
Rhombus	45°	14	0.25
Circle	-54.74°	22.5	0.41
Square	-54.74°	40	0.73
Rhombus	-54.74°	16	0.29
Circle	54.74°	30	0.55
Square	54.74°	39	0.71
Rhombus	54.74°	16	0.29
Circle	90°	33	0.60
Square	90°	16	0.29
Rhombus	90°	50	0.91

The data presented in Table 4.1 indicates that the material etches more rapidly along the {111} planes and more slowly along the {110} planes. This data suggests that to optimize my structures for undercutting of the mirror and preservation of

the anchor, a crystal plane aligned rhombus mirror with a square anchor aligned at 0° or 90° to the major flat would work best.

Another interesting consequence of crystal plane selectivity is the tendency of this etch to undercut the middle of some structures before completely removing the material around its edges. This effect is apparent in Figure 4.9 where residual wedges are apparent in a structure that was lifted off and where anchors can be seen on a structure that was not lifted off.

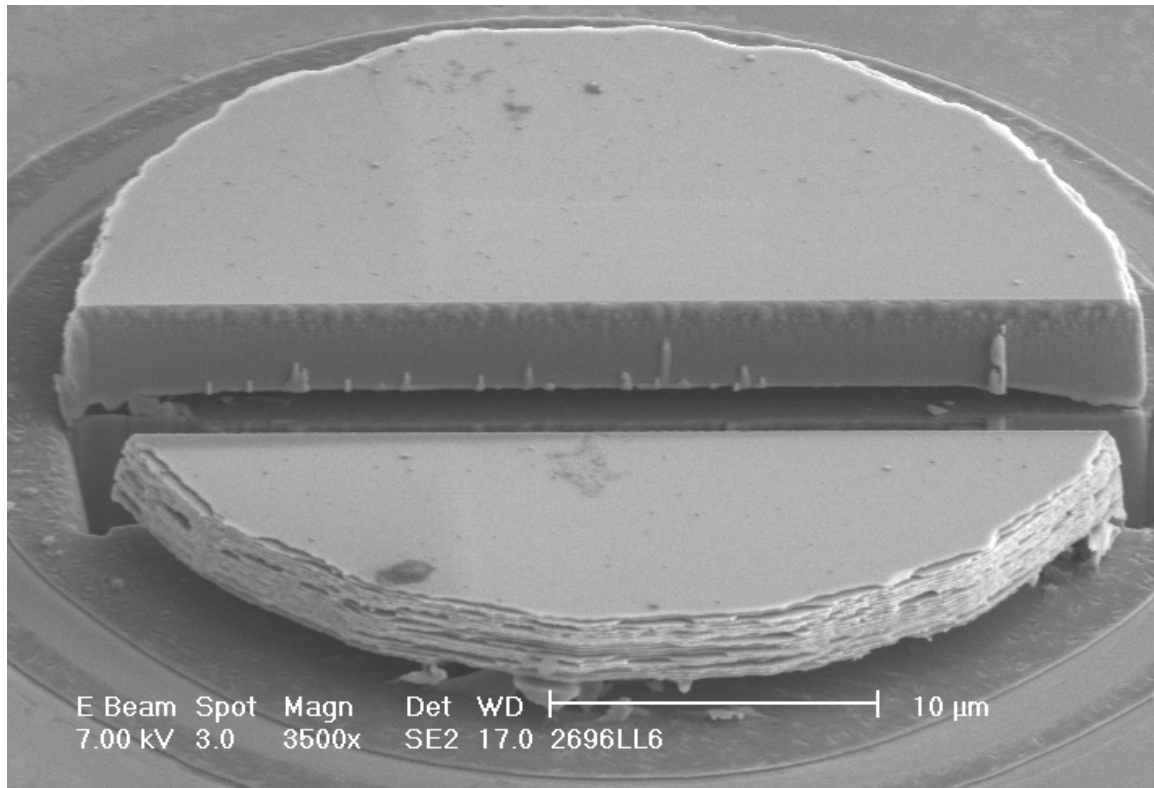


Figure 4.9 Images of structures where the middle was undercut before the edges due to crystal plane selectivity. This structure has been milled with a FIB to show that its edges are attached while its middle is released.

4.4 Oxidation Etch Study

4.4.1 Oxidation Rate and Crystal Plane Selectivity Characterization. For a process such as the one described in Section 3.4.4, where a material is selectively oxidized and then the oxide is removed, the etch progress is equivalent to the oxidation progress. Although oxidation rates for various compositions of $\text{Al}_x\text{Ga}_{1-x}\text{As}$ have been well characterized as discussed in Section 2.8, I found little information about oxidation layers more than 100 nm thick. I characterize oxidation rates for a sacrificial layer that is 329-nm thick. Because oxidation can also be selective with respect to crystal planes, the data collected is presented in Table 4.2 giving etch rates for the various shapes and orientations.

Table 4.2 Data collected for groups of 4 structures from a single sample concerning the oxidation progress of several shapes at various crystal plane orientations for an oxidation layer thickness of 329 nm after 2 hours and 34 minutes in the wet oxidation system. This was accomplished using sample UNM 1152 (see Appendix B for growth plan)

Shape	Angle Relative to Major Flat (110)	Maximum Feature Size Removed (μm)	Rate (μm/min)
Circle	0 °	105	0.68
Square	0 °	95	0.62
Rhombus	0 °	105	0.68
Circle	45 °	105	0.68
Square	45 °	95	0.62
Rhombus	45 °	125	0.81
Circle	90 °	105	0.68
Square	90 °	110	0.71
Rhombus	90 °	115	0.75

This data, along with observations made using infrared to image through the remaining DBR layers in the monitoring areas, indicates that crystal plane selectivity is present in the oxidation process. The rhombus shapes tended to etch the fastest in all circumstances, but this effect was most pronounced when they were turned at a 45° angle relative to the (110) plane. This would indicate that to optimize

my structures, the best layout would be a square anchor with a rhomboid mirror oriented at 45° to the major flat.

4.4.2 Oxidation Etching Material Selectivity. As discussed in Section 2.8, the oxidation rate of $\text{Al}_x\text{Ga}_{1-x}\text{As}$ decreases dramatically as the mole fraction of gallium increases. This selectivity should still be quantified to ensure that other parts of the process, such as the oxide removal, are not causing deterioration of the $\text{Al}_{0.1}\text{Ga}_{0.9}\text{As}$ and $\text{Al}_{0.9}\text{Ga}_{0.1}\text{As}$ comprising the DBR layers surrounding the oxidation layer. This measurement was accomplished in the same manner as the selectivity measurement for the selective wet etching of GaAs described in Section 4.3.2.1. Figure 4.10 shows an image of a structure that was milled away to allow me to determine the selectivity of the oxidation.

The $\text{Al}_{0.1}\text{Ga}_{0.9}\text{As}$ material showed no noticeable oxidation or degradation from the KOH:DIW oxide removal step. Smoothness was verified by attempting to focus on the remaining material at a magnification of 200,000x and finding no features. Any oxide present would have led to dielectric charging and been readily apparent during the SEM observations described above. As before, a direct comparison of etch rates between the relatively thick sacrificial layer and the $\text{Al}_{0.9}\text{Ga}_{0.1}\text{As}$ DBR layers (81-nm thick) is not necessarily valid. Keeping these conditions in mind, the selectivity between the sacrificial layer and the DBR layer most affected by oxidation is 454:1.

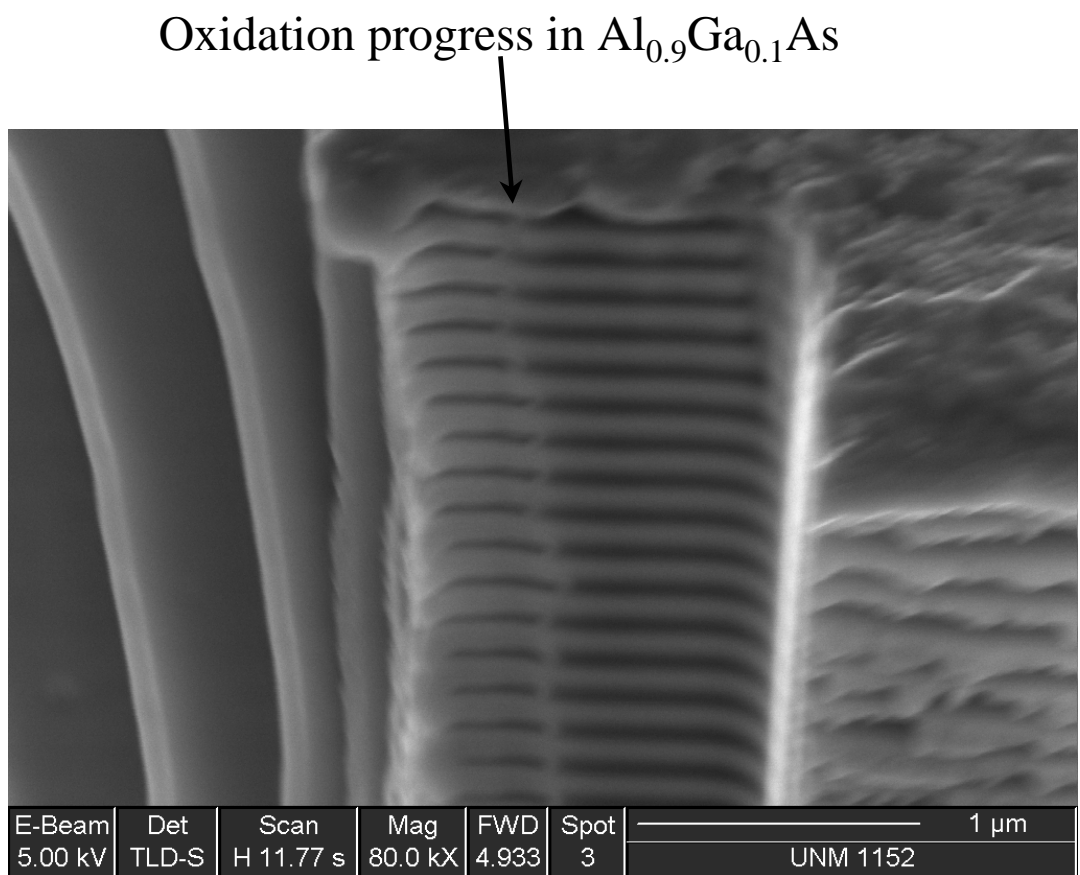


Figure 4.10 SEM image of a DBR structure consisting of alternating layers of $\text{Al}_{0.1}\text{Ga}_{0.9}\text{As}$ and $\text{Al}_{0.9}\text{Ga}_{0.1}\text{As}$ on top of an AlAs sacrificial layer (see UNM 1152 in Appendix B) after oxidation and oxide removal. A portion of the structure has been milled to allow for a determination of selectivity among the layers.

This selectivity also results in a relatively high degree of surface smoothness. Figure 4.11 shows a structure after release and makes it apparent that the surface was not greatly affected.

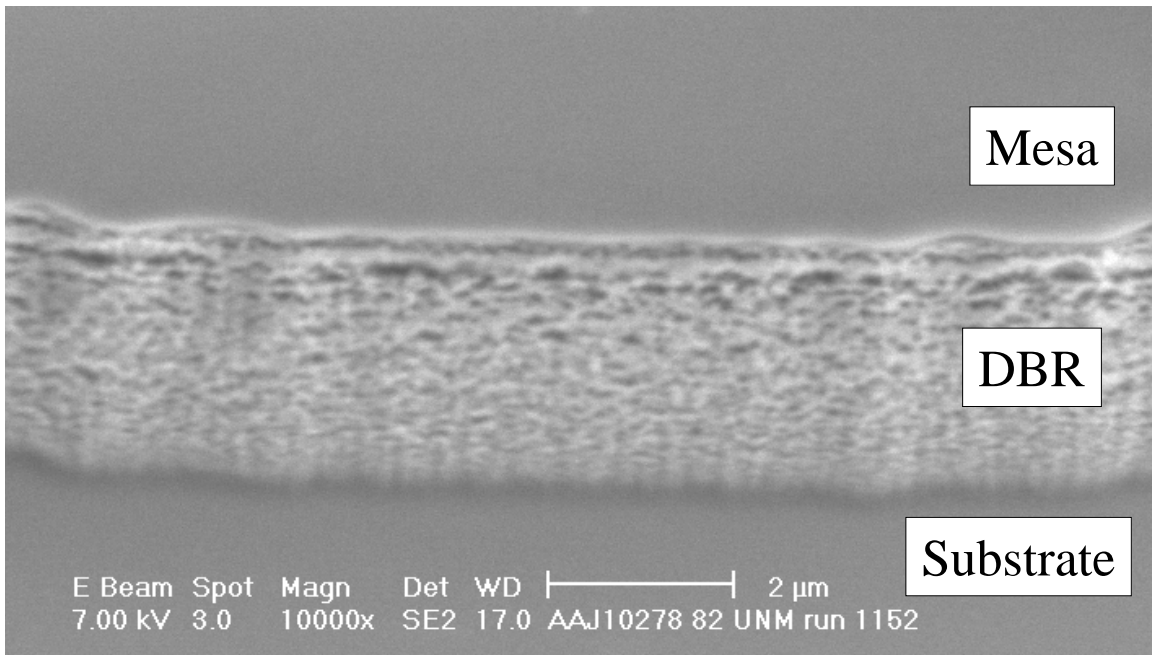


Figure 4.11 Image of a structure released by oxidation and selective oxide removal. This image illustrates the smoothness of the material left behind by this selective removal technique.

Gold contacts did not seem to be impervious to oxide removal. One effect observed is pitting of the gold's surface, as shown in Figure 4.12 a. Another effect attributable to the liquid release and subsequent CO₂ drying is the deformation of structures coated with gold. This deformation, as documented in Figure 4.12 b, caused sharp angles not normally associated with residual stress. Both of these effects were documented only after oxide removal with KOH: they were not present immediately after oxidation.

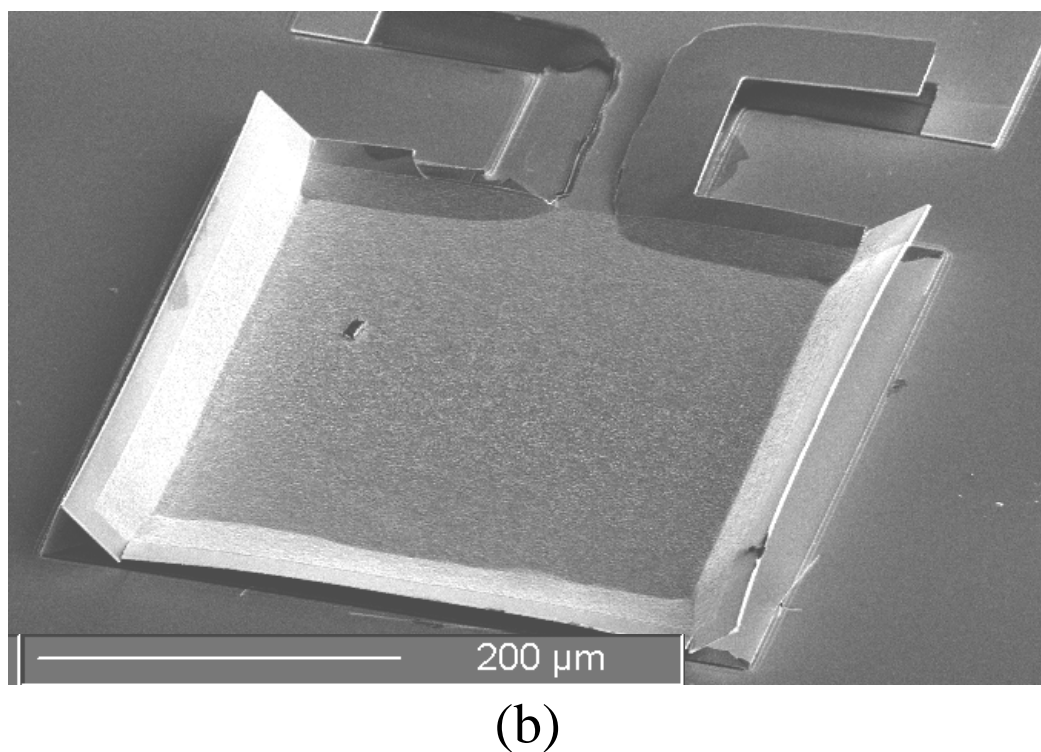
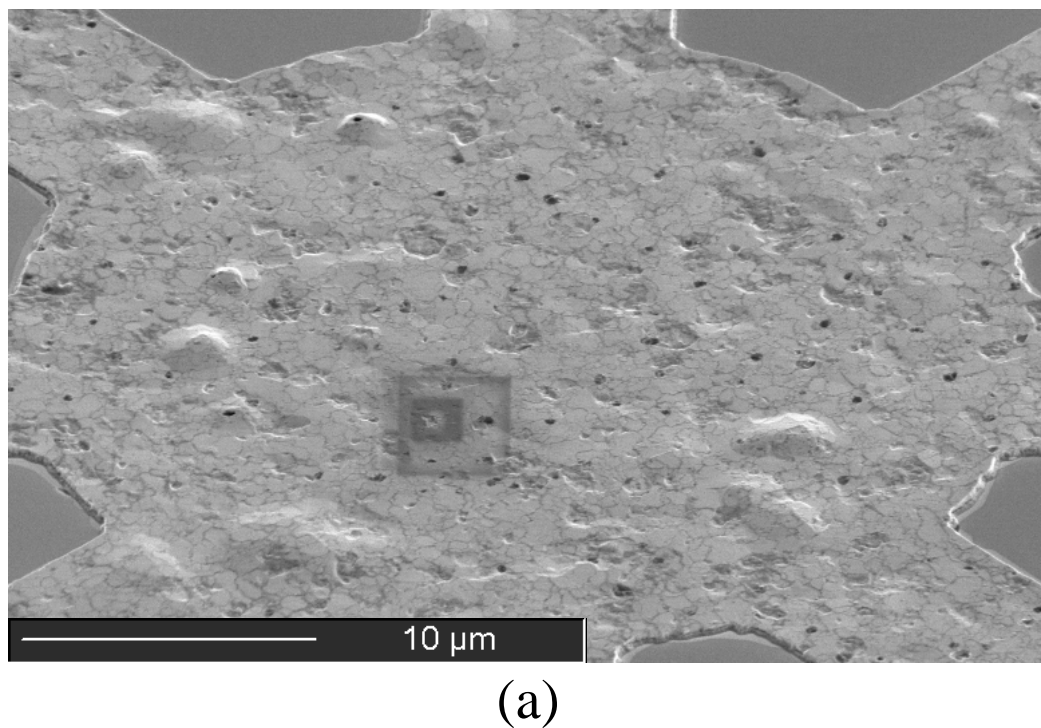


Figure 4.12 Effect of oxidation and oxide removal on gold contacts. (a) Roughness and pitting in the surface of the gold contact. (b) Structure deformation due to wet release and CO_2 drying.

4.5 Applications

4.5.1 Tunable Fabry-Perot Filters with GaAs Sacrificial Layers. As expected, the solution of $C_6H_8O_7:K_3C_7H_5O_2:H_2O_2$ (10:10:3) removed the GaAs sacrificial layers from underneath the mirrors and flexures of my tunable Fabry-Perot filters after remaining immersed in the etching solution for 5 hours and 39 minutes. This amount of time allowed for the apparent release of most of the mirrors and flexures while the much larger anchor and contact pads were not completely undercut.

In order to test the actuation capabilities of these structures, I probed their top contacts and the bottom DBR layer near the mirror I intended to actuate. Applying a reverse bias caused the top mirror to deflect downward. Figure 4.13 charts average values of actuation distance versus applied voltage for these structures. Unfortunately, this system was not modelled because there is little information about modelling superlattice mechanical layers available and time would not permit characterization of these layers on my part. I measured actuation distance using a Zygo New View 5000 interferometry system, which uses light interference patterns to accurately measure small distances.

These devices snapped down to the substrate when approximately 9.5 V was applied across them. For this reason, Figure 4.13 only shows actuation voltages as high as 9.45 V. After snap-down, there is very little movement at the tip of the mirror where I measured deflection, so no further measurements are taken. Fortunately, because the tip of the mirror landed first and the remainder of it did not snap down, these devices did release after the initial snap-down and proved to remain functional.

To probe whether these devices also possess desirable optical characteristics, reflectivity measurements were taken at several actuation voltages. These measurements were taken by reflecting a narrow spot off of one of the mirror structures and into a spectrometer where a diffraction grating separated the light by wavelength. The reflectivity measurements are all normalized to a gold standard. The measure-

Actuation Distance versus Voltage for GaAs Sacrificial Tunable Fabry-Perot Filters (G2-2747)

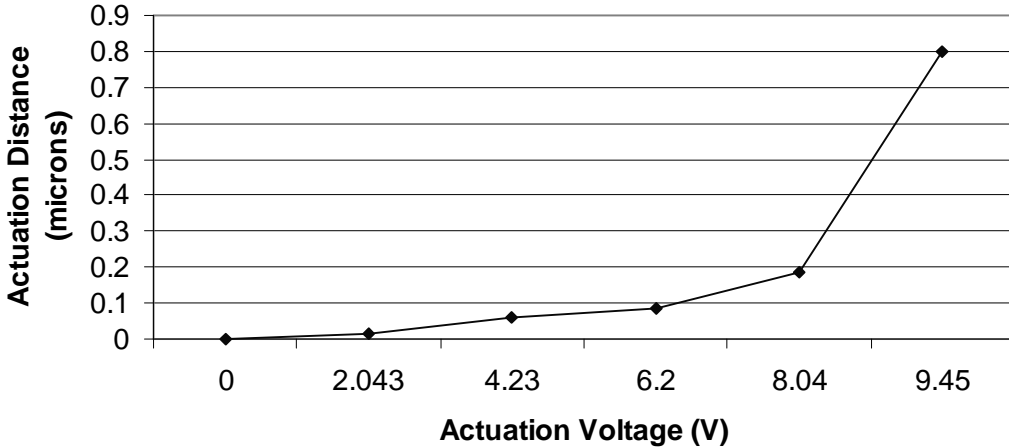


Figure 4.13 Graph of the data collected for actuation voltage versus deflection distance for a cantilever mirror structure with a circular base and circular contact (400 μm and 100 μm -diameter respectively released by selectively removing GaAs.

ments shown in Figure 4.14 do not conform to the expected form for a Fabry-Perot etalon. A plot of the measured and modelled reflectivity for the sample before any processing is also shown in Figure 4.14 to give a sense of the undesirable optical performance seen.

Figure 4.14 a shows that there was some movement of the reflectivity spectrum. If we assume that the difference in the middle reflectivity dip from Figure 4.14 a is a resonance shift of 7.25 nm, the corresponding mirror deflection can be calculated using the following equation [4]:

$$\lambda_{res} = \frac{2nd}{q} \quad (\text{nm}) \quad (4.1)$$

where

n = Index of refraction of the material filling the cavity

d = Distance between DBRs (length of microcavity)

q = Positive integer corresponding to the resonant mode of interest

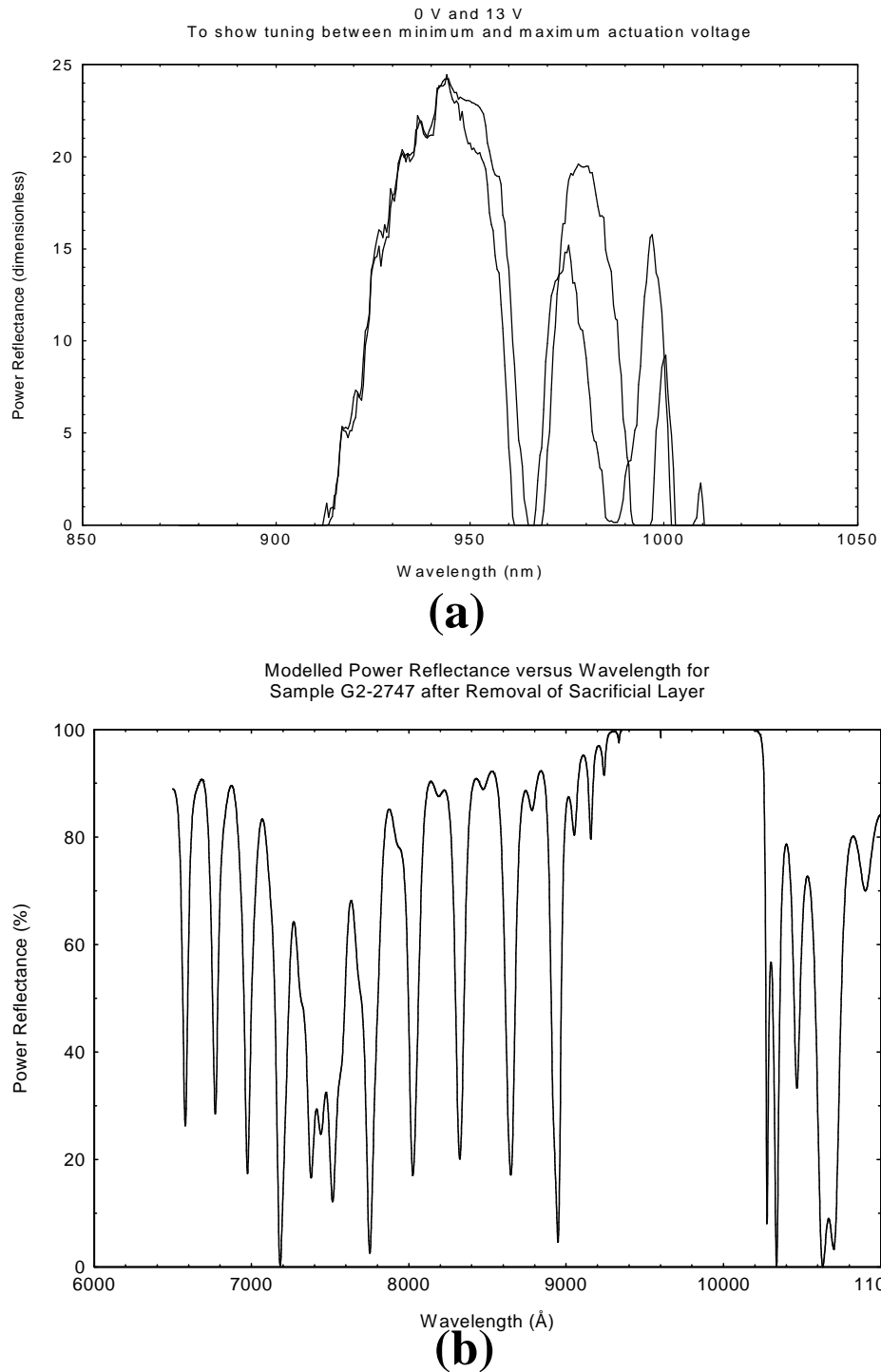


Figure 4.14 (a) Reflectivity plots illustrating the undesirable optical performance of my tunable Fabry-Perot filters. These structures consist of $\text{Al}_{0.1}\text{Ga}_{0.9}\text{As}$ / $\text{Al}_{0.9}\text{Ga}_{0.1}\text{As}$ DBRs surrounding a GaAs sacrificial layer (sample G2-2747). (b) Modelled reflectivity plot from the growth details in Appendix B.7 assuming complete removal of the GaAs sacrificial layer.

Knowing that $n = 1$ for air and that $\lambda_{res} = 994.5\text{ nm}$ at zero volts and that $d \approx 1500\text{ nm}$, it is apparent that $q = 3$ and that in reality $d = 1492\text{ nm}$. Solving Equation 4.1 for Δd yields:

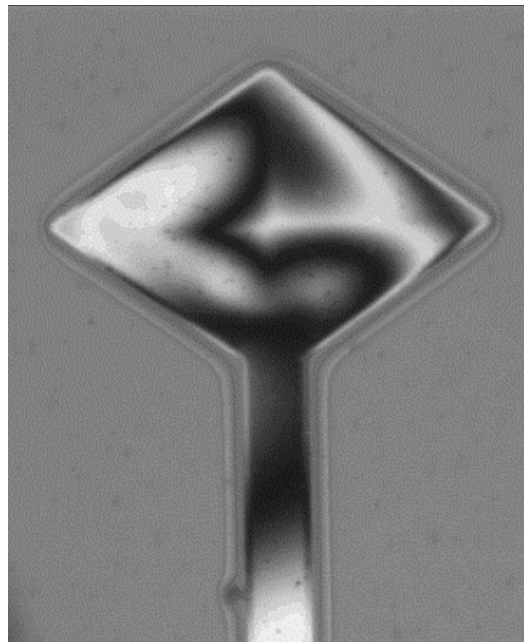
$$\Delta d = \frac{(\lambda_{res_1} - \lambda_{res_2}) \cdot q}{2n} \quad (4.2)$$

Substituting the given values for n , λ_{res} , and q into Equation 4.2 indicates a change in distance between the two mirrors of 10.9 nm. This does not correspond at all with the Zygo interferometry system deflection measurement of 800 nm for this voltage. Suspected reasons for this discrepancy are discussed in Section 5.2.4.1 and Section 5.3.1.2.

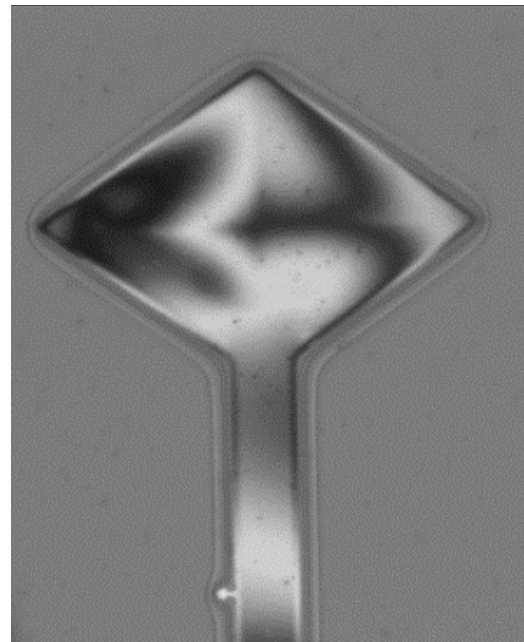
4.5.2 Tunable Fabry-Perot Filters with $Al_{0.98}Ga_{0.02}As$ Sacrificial Layers.

Oxidation and KOH removal of the $Al_xGa_yO_z$ also worked for freeing the structures. An oxidation time of 10 hours and 5 minutes followed by 15 minutes in KOH allowed some of the mirrors and most of the cantilevers to be freed without completely undercutting the anchor posts or contact pads.

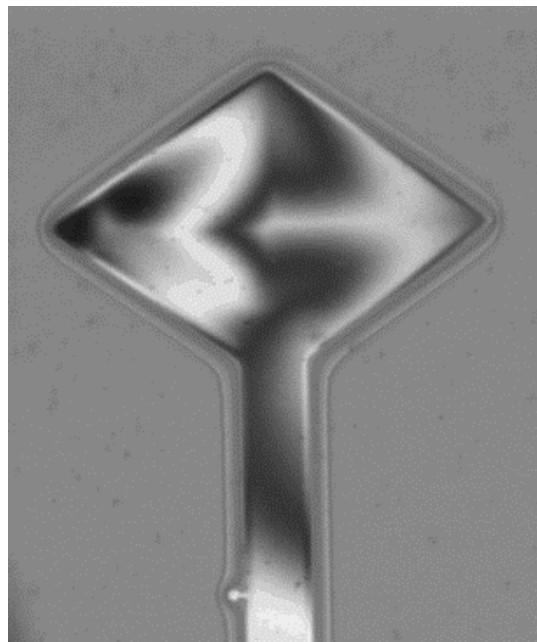
Actuation of these structures could not be measured using the Zygo interferometry system because the stress associated with oxidizing the sacrificial layer deformed the mirrors to the point where the machine would not recognize the fringe lines. A picture showing these irregular fringe lines, as well as how they shifted during actuation, is presented in Figure 4.15. I am certain that these irregular fringe lines are due to surface deformation in the released structure, because immediately before focusing on these structures, I was able to focus on the lower DBR below them and see the expected parallel fringe lines.



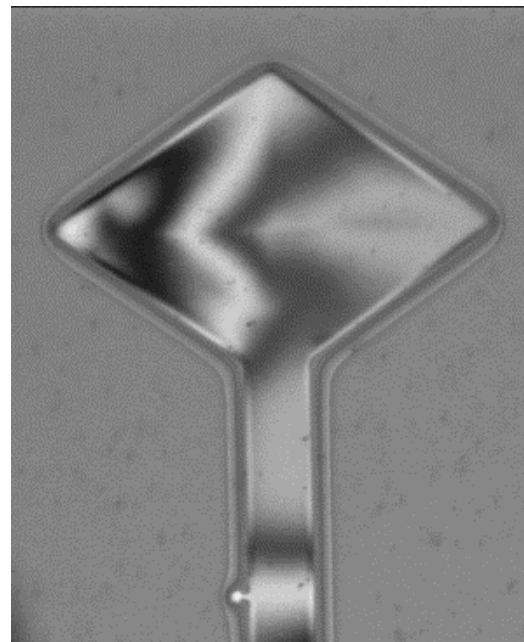
0 V



15 V



30 V



60 V

Figure 4.15 Series of images for varying applied voltages depicting the irregular fringe lines due to mirror deformation during oxidation. The series shows how the lines shift as actuation voltage is increased. These structures are 100 μm measured between their two closest vertices. They were fabricated from growth G2-2738.

The actuation voltage on the tunable Fabry-Perot filters with an $\text{Al}_{0.98}\text{Ga}_{0.02}\text{As}$ sacrificial layer can climb much higher before breakdown occurs than with the GaAs sacrificial structures. This allowed a greater tuning voltage range which afforded me the opportunity to show that the reflectivity plot shifts back toward its original state when I lowered the actuation voltage. The measured reflectivity plots are shown in Figure 4.16 a along with a modelled plot of the released structure in Figure 4.16 b. Again, using the shift of the central peak to attempt to quantify a shift in resonance, I calculated the mirror displacement required to show the apparent tuning. Using Equation 4.1 and Equation 4.2 again, I determined that the amount of actuation distance required for the observed shift in cavity resonance was 4.5 nm. I suspect that the mirror actually deflected much further than this, and suspected causes of this discrepancy and possible solutions are discussed in Section 5.2.4.1 and Section 5.3.1.2.

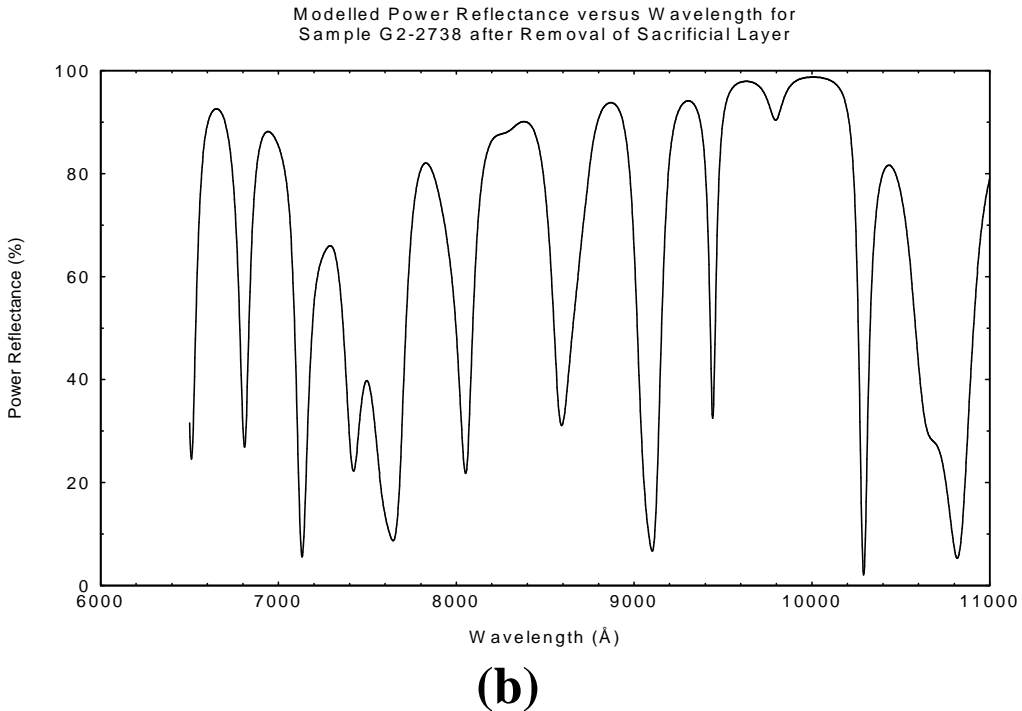
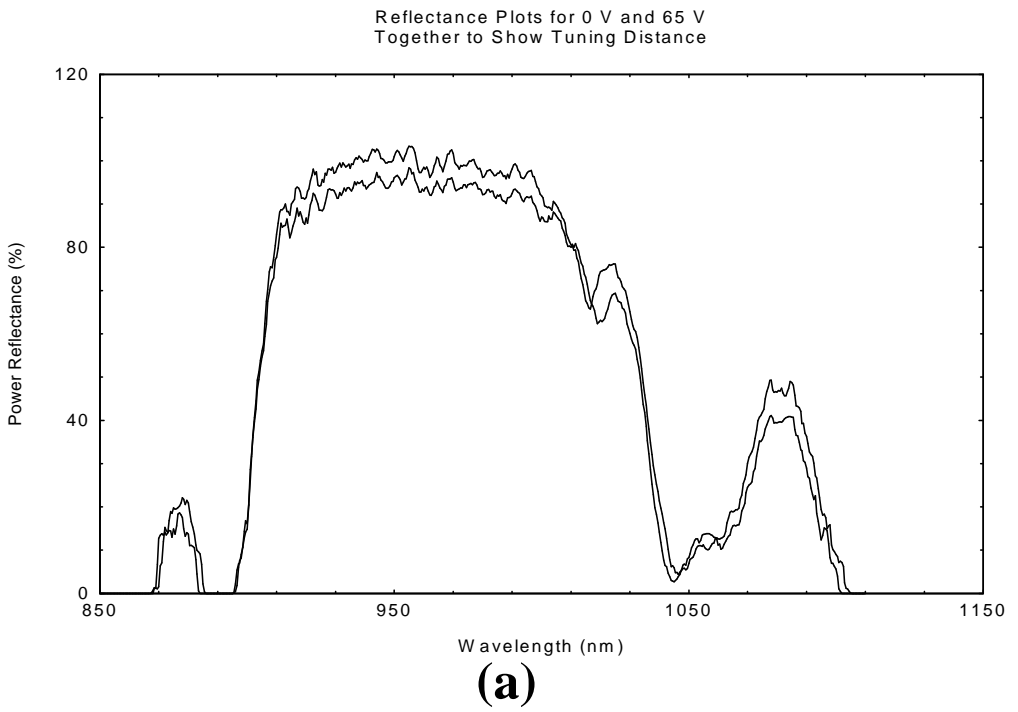


Figure 4.16 (a) Reflectivity plots illustrating the undesirable optical performance of my tunable Fabry-Perot filters. These structures consist of $\text{Al}_{0.1}\text{Ga}_{0.9}\text{As}$ / $\text{Al}_{0.9}\text{Ga}_{0.1}\text{As}$ DBRs surrounding a $\text{Al}_{0.98}\text{Ga}_{0.02}\text{As}$ sacrificial layer (sample G2-2738). (b) Modelled reflectivity plot from the growth details in Appendix B.6 assuming complete removal of the $\text{Al}_{0.98}\text{Ga}_{0.02}\text{As}$ sacrificial layer.

4.5.3 Lift-off Optical Devices.

4.5.3.1 Direct Etching of AlAs. The structures that I attempted to remove with HF:DIW 1:1 were severely attacked before their sacrificial layer could be removed. An image of a structure that was immersed in the HF:DIW solution for 60 seconds is shown in Figure 4.17, and a profile measurement across the center of one of these same structures is reproduced in Figure 4.18. Obviously, since every device on the test die showed this same degradation, this concentration of HF is completely unsuitable for removing devices from a substrate.

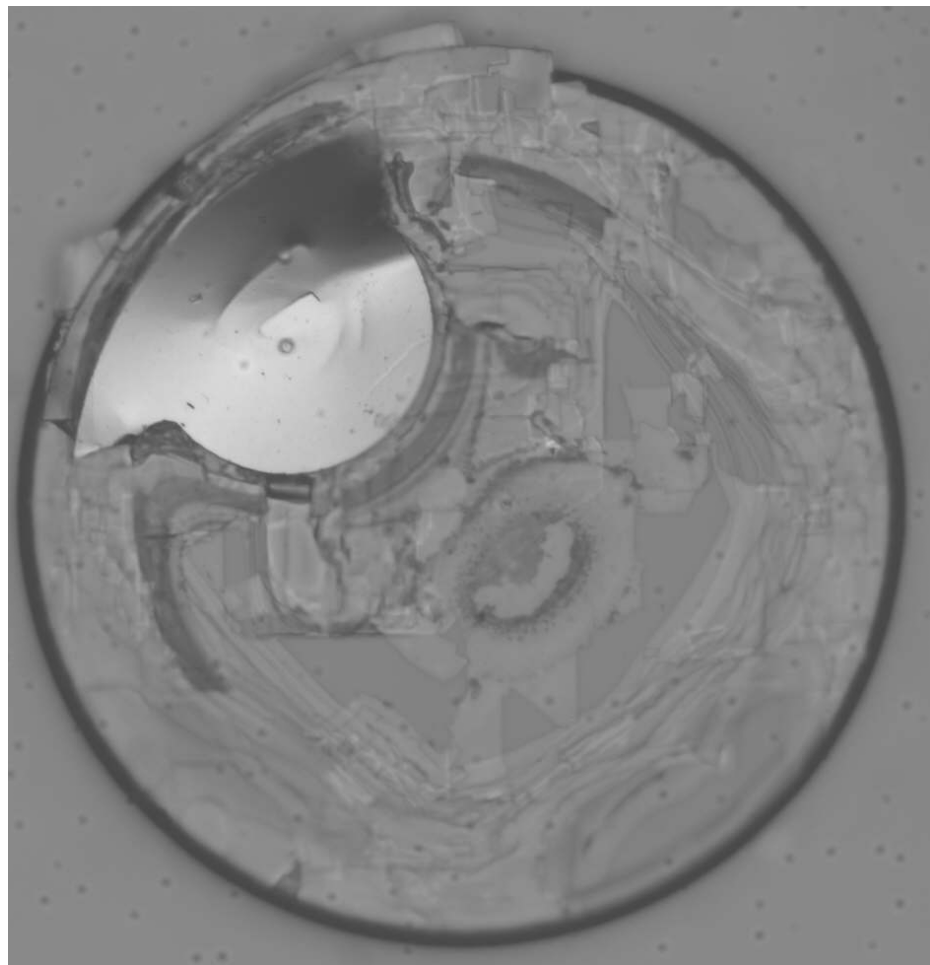


Figure 4.17 Image of a lift-off optical device that I attempted to release with HF:DIW 1:1.

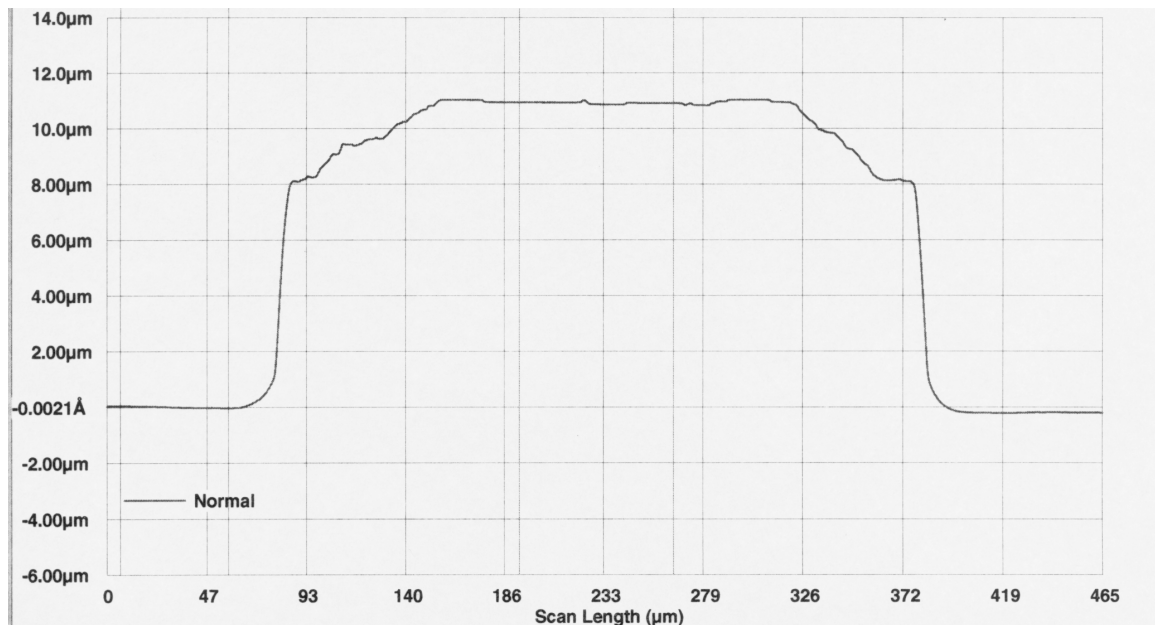


Figure 4.18 Profile obtained using a Tencor profilometer of a lift-off optical device where release was attempted using HF:DIW 1:1.

The other direct-etching method I tried (hydrofluoric acid:isopropyl alcohol:DIW 1:3:6) showed more selectivity, but still etched $\text{Al}_{0.9}\text{Ga}_{0.1}\text{As}$ rather aggressively. Based on an estimated etch rate of $3.3 \mu\text{m}/\text{min}$ [3], I left the sample in this solution for a period of 44 minutes. After this period of time, I found that all of the $\text{Al}_{0.9}\text{Ga}_{0.1}\text{As}$ layers had been removed from between the $\text{Al}_{0.1}\text{Ga}_{0.9}\text{As}$ layers, which left the $\text{Al}_{0.1}\text{Ga}_{0.9}\text{As}$ layers floating freely. Figure 4.19 shows the aftermath of this etch.

This etch also proved unsuitable for the purpose of releasing optical devices with the given composition structure. Furthermore, both of these HF-based etches caused the metal coating of the acceptor substrate to delaminate.

4.5.3.2 Oxidation of AlAs and Removal of Oxide. This scheme worked as planned. Because of the highly selective nature of oxidation and the KOH oxide etchant, the optical devices were left completely intact after oxidation

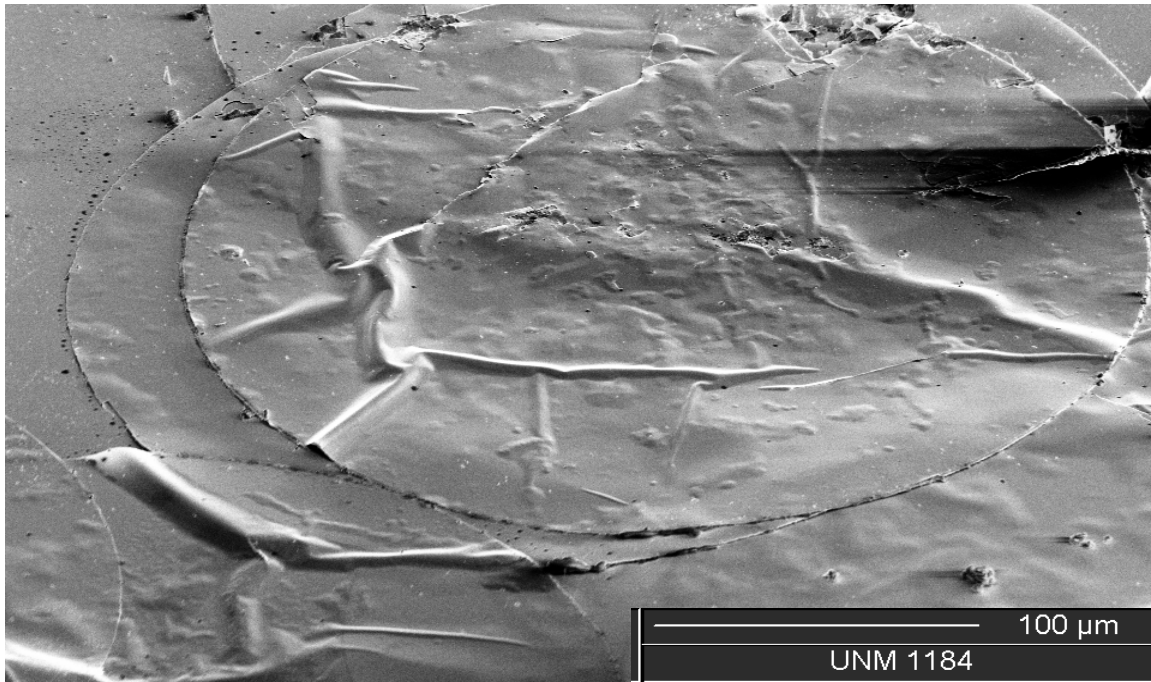


Figure 4.19 SEM image of Al_{0.1}Ga_{0.9}As disks left after an attempt to release an optical device from its substrate using HF:ISP:DIW 1:3:6.

and oxide removal. The devices came off singly and in sheets as shown in Figure 4.20 and did land on the acceptor substrate as planned.

Although yield was not high, some of the structures landed on the acceptor substrate right side up and I was able to probe and characterize them. As the spectra in Figure 4.21 show, these devices behave as resonant-cavity light emitting diodes. Preliminary testing of this wafer also revealed RCLED behavior as illustrated in Figure 4.21. The device measured after transplantation has a different peak emission wavelength than the device measured before release. The reason for this difference is the fact that epitaxial growth thicknesses are not completely uniform across the wafer, which causes the resonant wavelength of the microcavity devices to differ, as shown in Figure 4.22 . Due to the randomness of the fluidic release and settling process, I cannot control which area of a sample the devices I am able to release and test will come from, so the comparison drawn in Figure 4.21 is indirect.

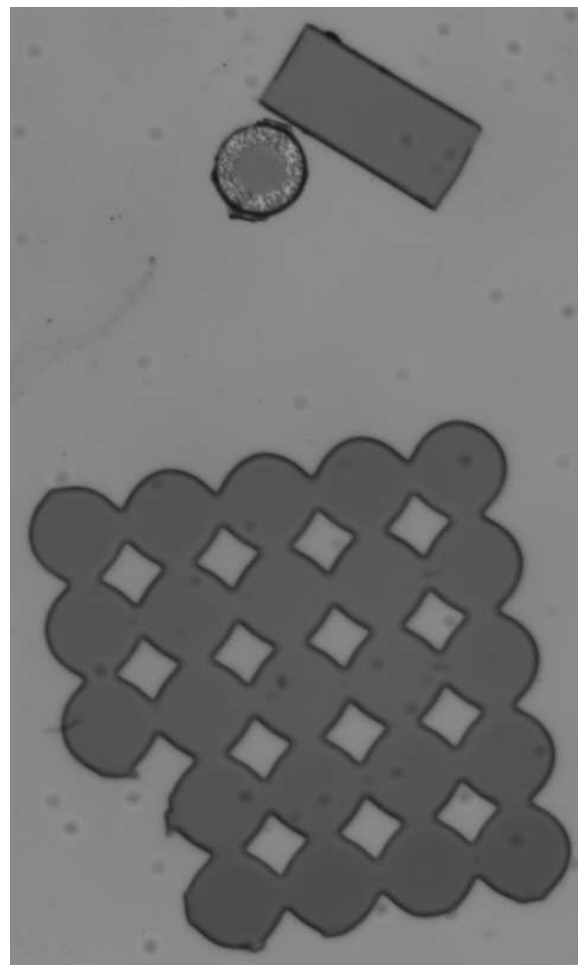
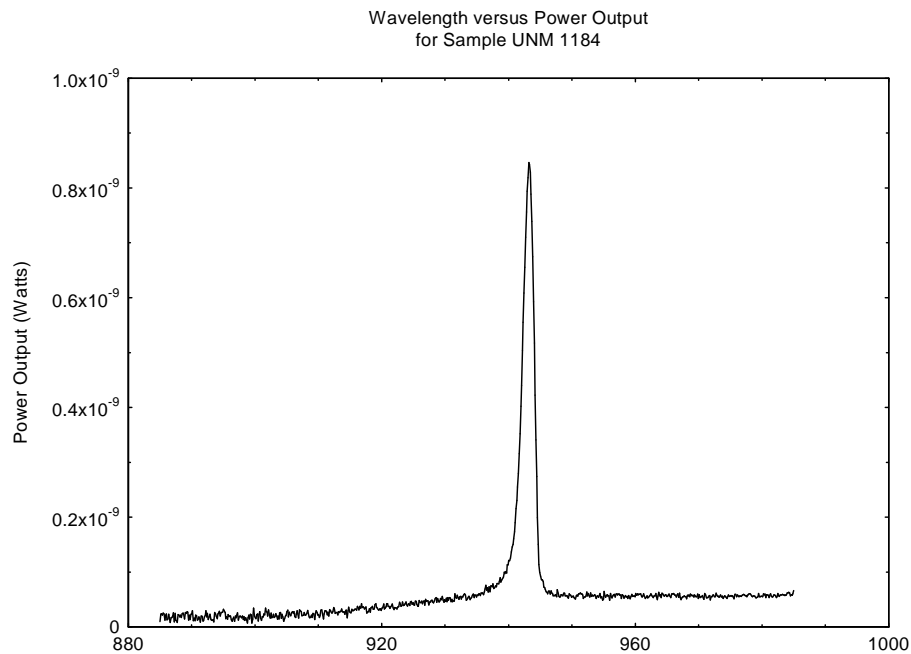
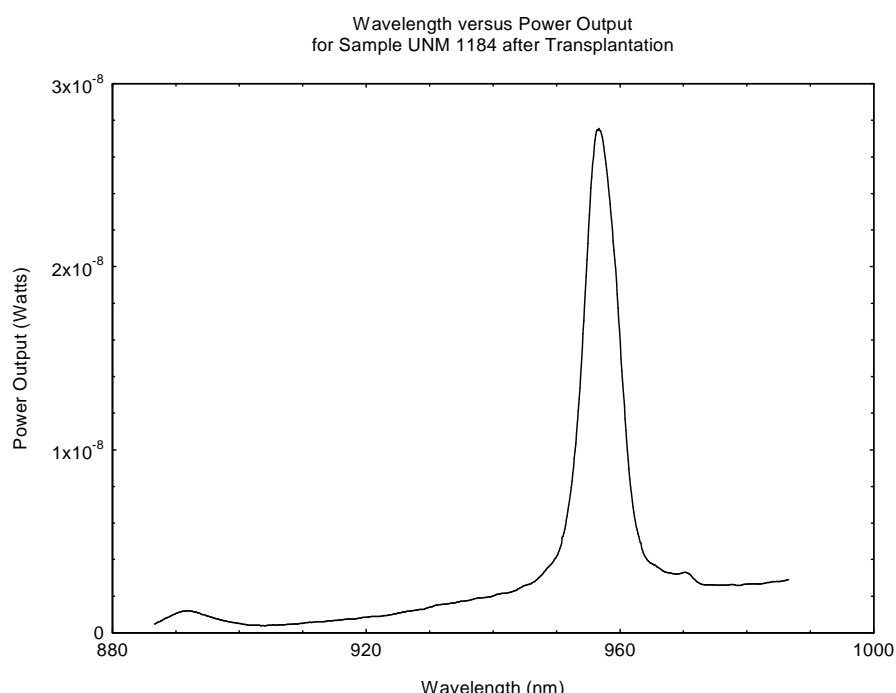


Figure 4.20 Image of microcavity devices on the acceptor substrate after successful, intact removal from their native substrate.



(a)



(b)

Figure 4.21 Electroluminescence spectral profiles of the optical devices used in the microcavity device lift-off study: (a) before release, and (b) after transplantation. These measurements were both taken at a temperature of 300 Kelvins (K) using a continuous current.

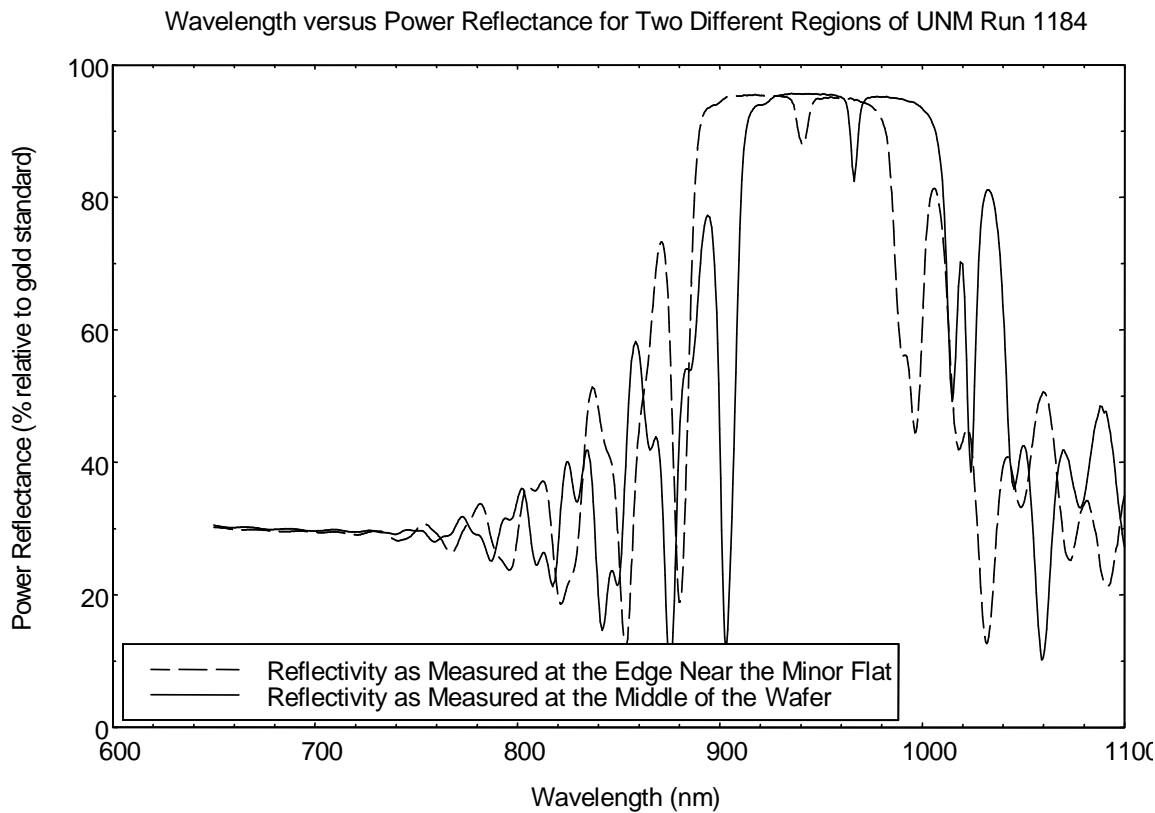


Figure 4.22 Reflectivity plots showing cavity resonance for the middle and edge of sample UNM 1184.

The light power-current-voltage (L-I-V) characteristics of the transplanted RCLEDs were also measured and are shown in Figure 4.23. Because the unreleased structures cannot make good contact to the probe station's bias chuck for the purpose of taking these measurements there is no basis for comparison.

The peak power emission, as measured by the height of the central peak on the spectrometer, occurred at a current of approximately 2.75 mA. For the unreleased devices this peak occurred around 55 mA, which gives a greater sense of the inconsistency of comparison between the released and unreleased devices. The inconsistency is due to the fact that the unreleased structures do not have a backside metal contact: placing the sample directly onto the bias chuck does not form a good, ohmic contact.

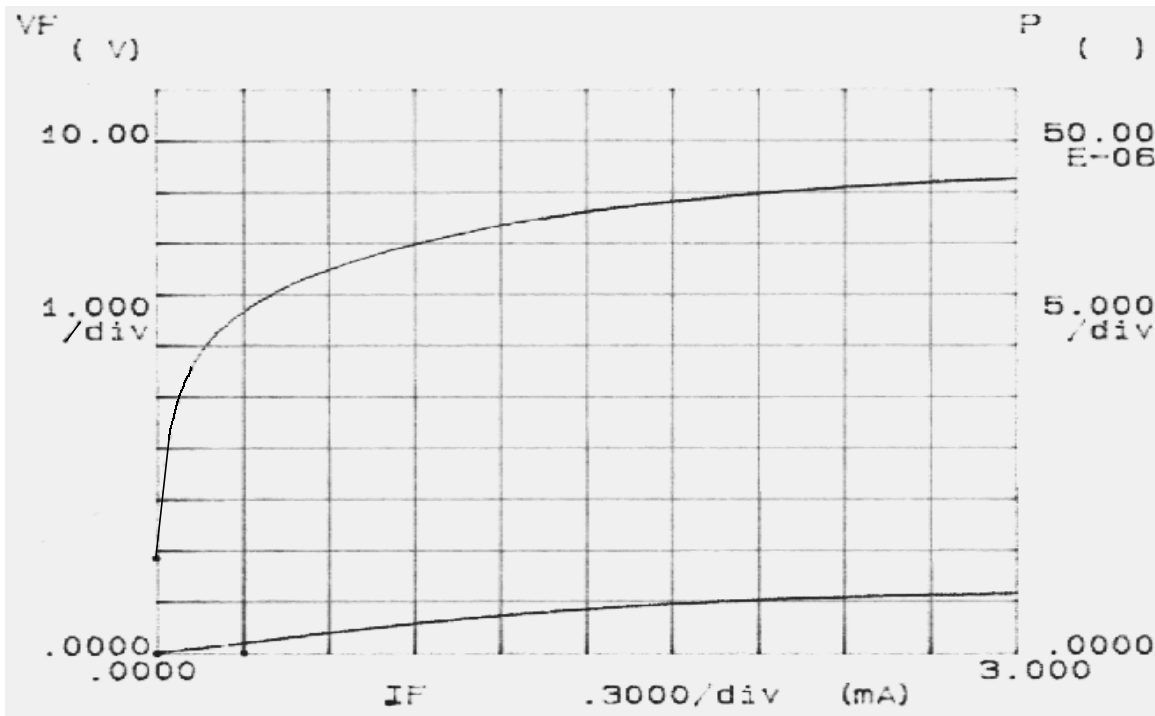


Figure 4.23 L-I-V characteristics of a transplanted RCLED. Luminescence is the upper curve and is measured by the scale on the right. Current is the lower curve and is read according to the scale on the left.

Another result of interest is the fact that I was able to lift off the devices in arrays and that only the largest devices were transplanted. This happened because the mesa definition RIE did not completely penetrate to the sacrificial layer in the tight spaces between devices. This means that when the sacrificial layer was removed, the devices were still attached to each other by a thin segment of their bottom DBRs. A closer view of this attachment is shown in Figure 4.24.

4.6 Conclusion

Although some of my experiments did not achieve the expected results, all of them did have success in one manner or another. The most important result of this work is the confirmation that these semiconductor processing techniques will allow the fabrication of $\text{Al}_x\text{Ga}_{1-x}\text{As}$ MEMS. This was demonstrated through the

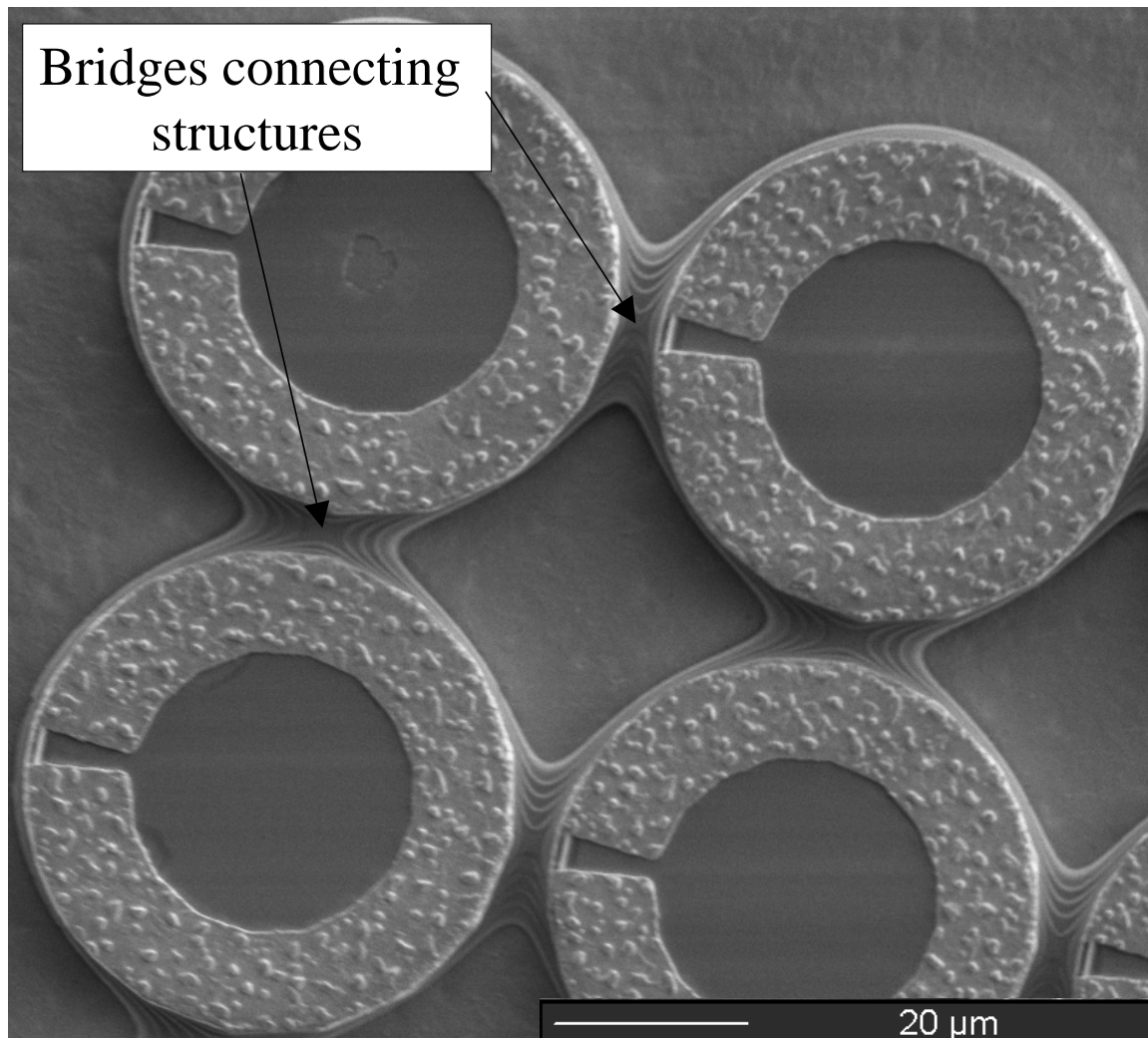


Figure 4.24 SEM image of the thin bridge connecting the RCLED lift-off devices to one another and causing them to transplant in arrays.

applications that I was able to release and actuate. Furthermore, the movement of optical devices from one substrate to another proves the potential of this techniques for the fabrication of $\text{Al}_x\text{Ga}_{1-x}\text{As}$ MOEMS.

Bibliography

1. Chang, H.-C., Chang, E. Y., Chung, C.-C., and Kuo, C. T. “Highly Selective GaAs/Al_{0.2}Ga_{0.8}As Wet Etch Process for the Gate Recess of Low-Voltage-Power Pseudomorphic High-Electron-Mobility Transistor,” *Japanese Journal of Applied Physics, Part 1*, 39(8):4699–4703 (2000).
2. Lee, J. S. “Digital image enhancement and noise filtering by use of local statistics,” *IEEE Trans. Pattern Anal. Machine Intell.*, 165–168 (1980).
3. Ochoa, E. M., “Private Communication.” Ph. D. Candidate, Air Force Institute of Technology, Department of Electrical and Computer Engineering, Wright-Patterson AFB, OH. January 2002.
4. Verheyen, J. T. *Laser Electronics*. Upper Saddle River, New Jersey: Prentice Hall, November 2000.

V. Conclusions

5.1 Introduction

This chapter expounds on the results of Chapter IV to include further analysis of the experiments I undertook and their results. I begin by drawing conclusions from the three etch studies. I then discuss how the lessons learned from these studies are applied to prototype structures as well as how to improve on the methods presented previously. I discuss some of the processing knowledge gained during these experiments with the hope that future researchers can leverage my experience to develop more functional processes. Next, I discuss the contributions that my work has made to the advancement of III-V MOEMS. Finally, some possibilities for future work in this area are presented.

5.2 Concerning Experiments

5.2.1 Dry Etch Study. Since selective etching of GaAs using BCl_3 and SF_6 has been documented in the past [1], I do not construe my failure to accomplish it as an invalidation of the technique. My failure does show that the technique, like most processing steps, is not completely robust. The failure of these gasses to etch are most likely due to a thin residual film left on the sidewalls of the mesa structures during the mesa definition RIE or the subsequent photoresist removal. The BCl_3 and Cl_2 etch chemistry in combination with 1800 series photoreists is used to prevent undercutting during the mesa definition etching by forming a passivation layer along exposed sidewalls. If this passivation layer remains in place during the subsequent attempt to perform an undercutting etch, it may inhibit the selective removal of the sacrificial layer. Another method to investigate dry release might use dielectrics or metals as a mask to eliminate these sidewall passivation effects. A simple experiment whereby the mesa definition is performed by wet etching or where resist is left on the sample until after the undercutting etch would tell whether this

is the case and could lead to further development of this highly advantageous dry release technique.

5.2.2 Wet Etch Study. Removing GaAs from $\text{Al}_x\text{Ga}_{1-x}\text{As}$ structures using $\text{C}_6\text{H}_8\text{O}_7:\text{K}_3\text{C}_7\text{H}_5\text{O}_2:\text{H}_2\text{O}_2$ (10:10:3) proved effective. This technique showed several desirable qualities including a slow, controllable etch rate, high selectivity, smooth surfaces remaining on structural layers, and no pejorative effects on metal contacts. Several other factors that make this a practical method for selective removal of GaAs are its relatively low cost, its safety, and the fact that no special equipment is required.

The main drawback suffered while implementing this technique was its sensitivity to thin residual films on the sidewalls of the structures it was supposed to undercut. In several cases, this thin film completely inhibited etching. To mitigate these problems, I modified my process so that samples went directly from RIE mesa definition to wet undercutting etch without removing the photoresist of the mesa definition mask. I also found that removing the resist with oxygen plasma was an effective means of preventing the film that inhibits etching.

The crystal plane selectivity demonstrated by this etch can be leveraged to provide several advantages. Chief among these is the ability to have the etch undercut structures that should be released more quickly than anchors that should not be released. For example, my cantilever mirror structures could be optimized by having a diamond-shaped mirror on a square base oriented at 0° or 90° to the (110) plane, which is designated by the major flat on the wafer. This purposeful mismatch of crystal plane orientations will slow the etch on the anchor structure causing it to remain more firmly affixed to the substrate while the etch completely undercuts the structures intended for release.

Another exploitation of crystal plane selectivity is the formation of membranes of III-V material. As reported in Section 4.3.2.2, the middle of some structures was

undercut before the edges, which leaves a membrane of DBR material. If this type of structure could be actuated to move this top membrane vertically relative to a fixed bottom DBR, another type of tunable Fabry-Perot filter could be produced. The advantage of a membrane scheme is that devices could be packed onto a substrate much more densely since there are no external supports.

5.2.3 Oxidation Etch Study. Oxidation, even in AlAs with relatively thick oxidation layers, also proceeds at a slow, controlled rate. Its high selectivity, smooth surfaces remaining on structural layers, low cost, and safety all make oxidation an attractive option for release. However, the need for special equipment, and the longer preparation time make it a slightly less attractive option than direct wet etching. The slight incompatibility of my oxide removal process with gold contacts may also present an obstacle for some processes.

One key advantage to oxidation etching is that it seems to be impervious to the thin film formed during RIE or photoresist removal. This could be due to the fact that the high temperature in the oxidation furnace causes the film to crack and allow the water vapor to contact the AlAs or $\text{Al}_{0.98}\text{Ga}_{0.02}\text{As}$. Two other possibilities are that the oxidizing species simply diffuse through the film or that they actually attack and remove the film, and then oxidize the semiconductor oxidation layer. Regardless of the mechanism, this advantage is significant when residual films inhibit other types of etching.

5.2.4 Applications.

5.2.4.1 Tunable Fabry-Perot Filters. Although my tunable Fabry-Perot filters did release and actuate, they did not perform as expected. Mechanically, they showed only about half as much deflection as was expected (800 nm versus 1.5 μm). Optically, they did not show tuning or even fixed Fabry-Perot etalon behavior as was expected. I believe both of these effects are attributable to residual material

left in the air gap after release. Section 5.3.1.2 contains more information on this phenomenon. To correct this situation, I would allow more time in the etchant. Since the anchors and contact pads had plenty of sacrificial material left to secure them, this process improvement would allow for complete release of the devices without removal of the necessary anchors.

Another factor that may have affected the functionality of these structures is the questionable nature of the epitaxial growth conditions. I was informed that the aluminum effusion oven was not maintaining a constant flux rate when the sample (G2-2747) intended for release by removal of GaAs was grown. This would have caused variable indices of refraction in the different layers of the DBRs, which would inhibit predictable cavity resonance. A reflectivity plot taken before any processing was performed on the wafer (Figure 5.1) shows that it does not match the values calculated based on the growth plan (Appendix B.7), nor does it have the single reflectance dip desired from the Fabry-Perot etalon.

While aberrant growth conditions may partially explain why the sample with the GaAs sacrificial layer did not perform as expected, they do not explain why the sample with the $\text{Al}_{0.98}\text{Ga}_{0.02}\text{As}$ sacrificial layer performed poorly. The reflectance plot shown in Figure 5.2 shows that the $\text{Al}_{0.98}\text{Ga}_{0.02}\text{As}$ sacrificial sample did exhibit good optical behavior before any processing. Although the measured data does not match the calculated data, the etalon does show expected Fabry-Perot behavior.

The fact that sample G2-2738 is optically well-behaved indicates that the problem is less likely with the growth than with the post-processing. The most likely culprit for the poor optical performance seen is incomplete release as discussed in Section 5.3.1.2.

5.2.4.2 Lift-Off Optical Devices. The transplantation technology I explored shows great promise as a way to integrate III-V optical devices with other materials. The fact that the transplanted devices did not lase is due to the fact that

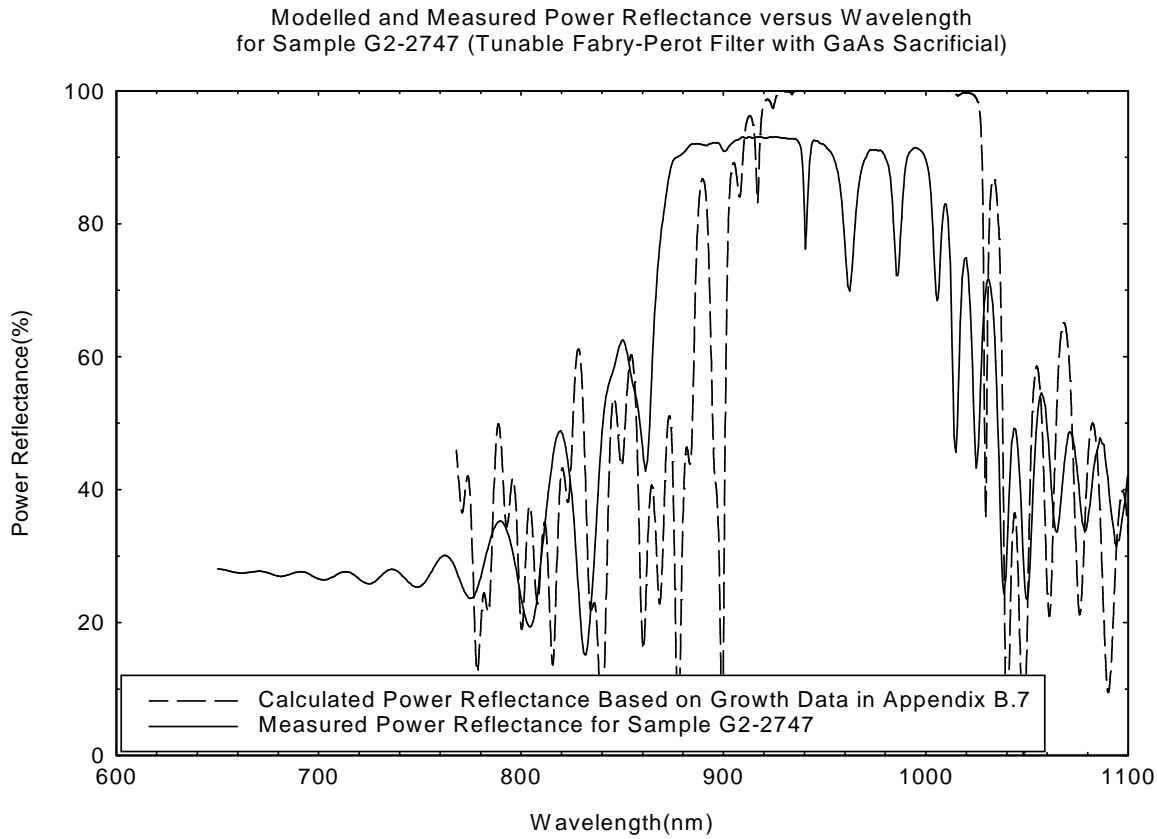


Figure 5.1 Measured and modelled reflectivity plots taken from sample G2-2747 (tunable Fabry-Perot filter with GaAs sacrificial) before any processing was performed.

the gain for the devices is centered at 980 nm, while the cavity resonance is centered around 960 nm. The fact that they maintained RCLED behavior is encouraging because it indicates that a laser device could also be transplanted.

Another important accomplishment in this application is the ability to transplant structures in arrays. Although I discovered this accidentally, I could easily reproduce the effect by monitoring etch progress via reflectivity measurements in a large open area and stopping the etch as soon as the sacrificial layer has been etched away. This would breach the sacrificial layer in the large areas between the devices, but leave a portion of the bottom DBR intact where devices are close together due to the lower concentrations of active etching species in these areas. As a rough es-

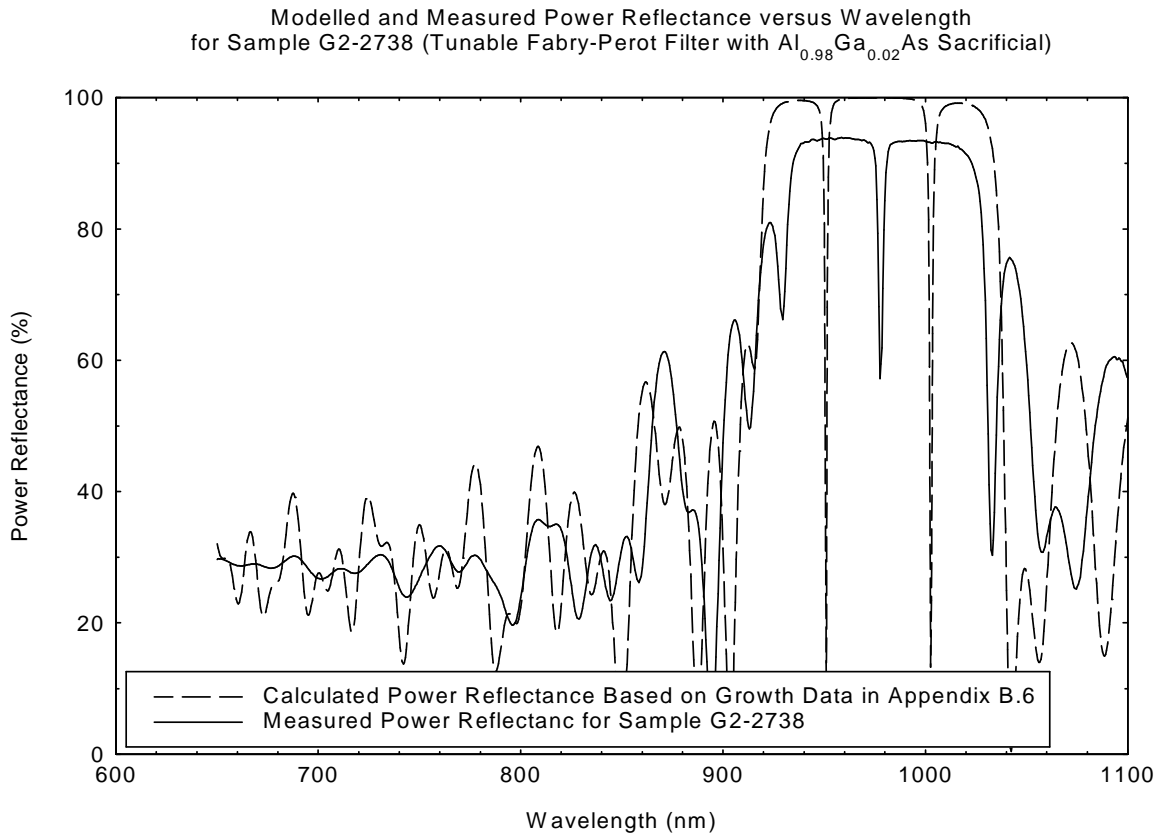


Figure 5.2 Measured and Modelled reflectivity plots taken from sample G2-2738 (tunable Fabry-Perot filter with $\text{Al}_{0.98}\text{Ga}_{0.02}\text{As}$ sacrificial) before any processing was performed.

timate, structures with separation of less than 5 % of their diameter between them seem most prone to remaining connected by their bottom DBRs.

The main failure of this experiment was the inability to transplant smaller devices. Because of the smaller devices' close proximity to one another, the open areas between them did not undergo enough etching to expose the sacrificial layer. To remedy this problem and transplant smaller devices, I would design a mask in which the smaller features were spaced further apart. The devices could still be made to lift off in strings, though, if they were placed close together on one axis and further apart on the other. An example of this improved mask design is given in Figure 5.3.

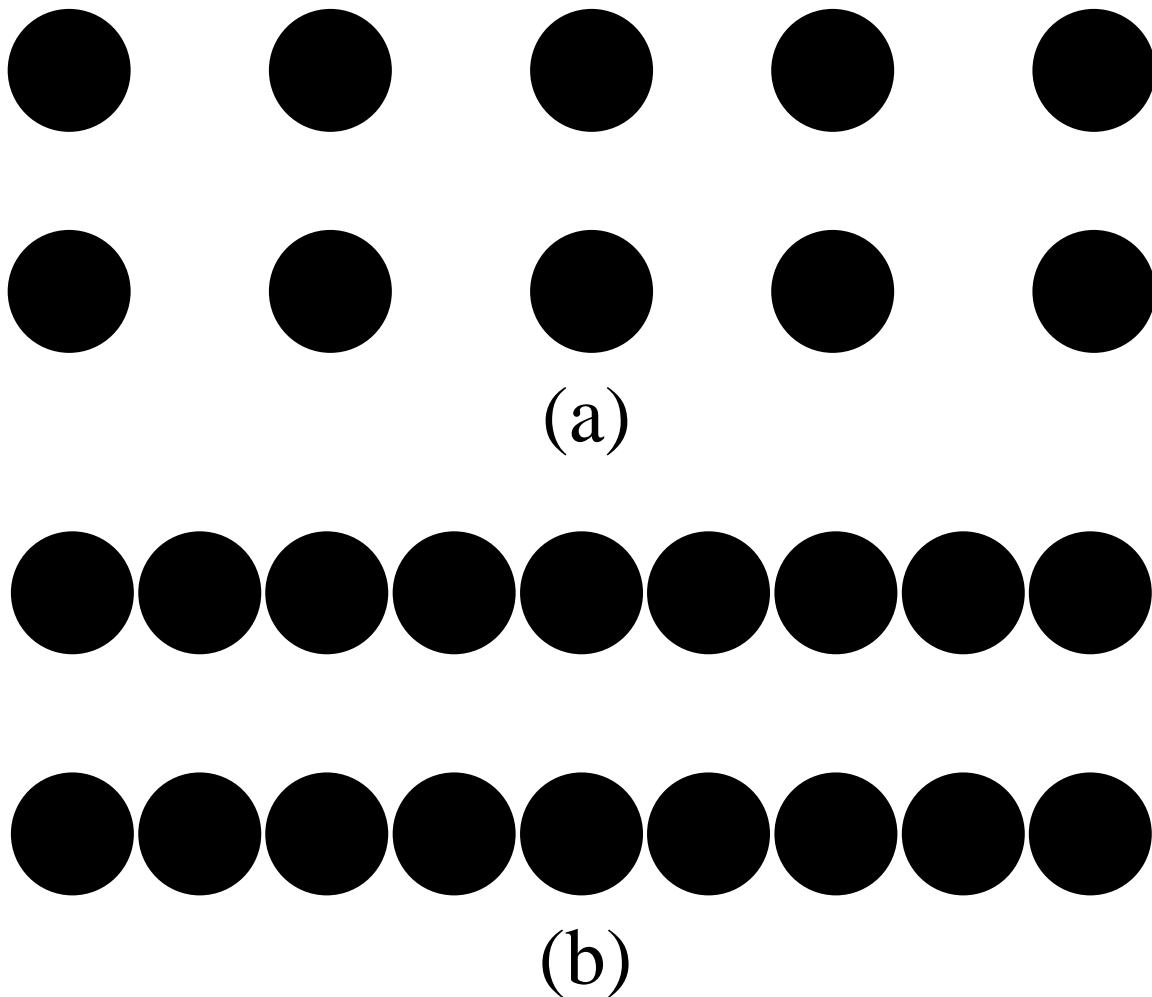


Figure 5.3 A proposed design for a lithography mask that would facilitate better lift-off of small structures both (a) alone and (b) in strings.

Other possibilities related to this study that seem promising are the transplantation of devices using a GaAs sacrificial layer selectively removed by a $\text{C}_6\text{H}_8\text{O}_7$:
 $\text{K}_3\text{C}_7\text{H}_5\text{O}_2:\text{H}_2\text{O}_2$ etching solution. Because of the desirable optical performance of this etch on my previous structures, I have every confidence that this technique would allow the successful transplantation of optical devices from one substrate to another without degradation of their optical properties.

The direct removal of AlAs using HF:ISP:DIW should also work effectively if the DBRs were composed of alternating layers of GaAs and $\text{Al}_{0.5}\text{Ga}_{0.5}\text{As}$, both of

which would be resistant to the HF:ISP:DIW etching solution. The drawback to a VCSEL with DBR layers composed of GaAs and $\text{Al}_{0.5}\text{Ga}_{0.5}\text{As}$ is that the contrast in index of refraction between the two layers would be relatively small. This would cause two consequences: (1) the mirror stacks would have to be extraordinarily thick, and (2) the high-reflectivity band of each DBR would be narrower. The thickness of the stack would cause problems with photoresist mask degradation during the longer RIE that would be required for mesa definition. The narrower reflectivity band should not greatly effect the performance of the device unless it was intended to tune across a range of wavelengths.

5.3 Lessons Learned

5.3.1 Semiconductor Processing.

5.3.1.1 Residual Film Formation. The most important lesson I learned from the processing aspect of my research was that just because a process is mature does not mean that it will be compatible with other processes. This is illustrated most graphically in the thin residual film that coated some of my samples after RIE and photoresist removal. The film is pictured in Figure 5.4. The appearance of this film seemed to indicate a shortcoming in the compatibility between the RIE system that I utilized and wet etching. Fortunately, I was able to find a workable solution that allowed wet etching in spite of the film.

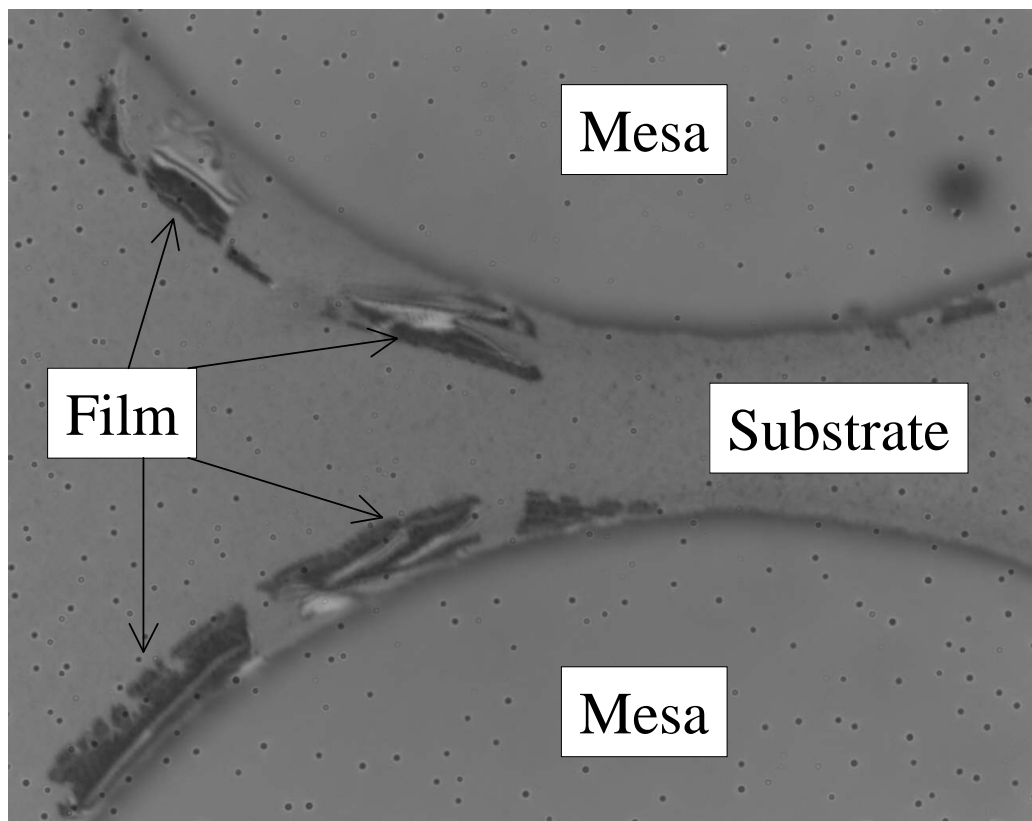


Figure 5.4 Image showing the thin residual film that prevented wet etching after RIE and photoresist removal.

5.3.1.2 Completeness of Release. When a structure is freed by an undercutting etch, this does not mean that all of the sacrificial material has been cleared from beneath it. Figure 5.5 shows a case where a structure has been freed, but material remains in the gap opened by removal of the sacrificial layer.

Incomplete release causes several problems with later attempts to actuate the partially released device. First, the device may not be able to utilize the entire distance of travel for which it was designed. Second, if the residual material is not distributed uniformly, the device can twist during electrostatic actuation. This arises from the fact that electrostatic attraction is stronger in one area of the structure than in others. The consequences of incomplete release on actuation can be seen in Figure 5.6.

A further consequence of incomplete release is interference with optical testing of the devices. The residue shown in Figure 5.5 will obviously scatter light during transmission measurements and inhibit cavity resonance during both transmission and reflection measurements. The presence of this unremoved material alters the optical properties of the cavity in unpredictable ways. As mentioned in Section 5.2.4.1, I believe this incomplete release to be responsible for the fact that resonance shifts were not readily apparent in my tunable Fabry-Perot filters.

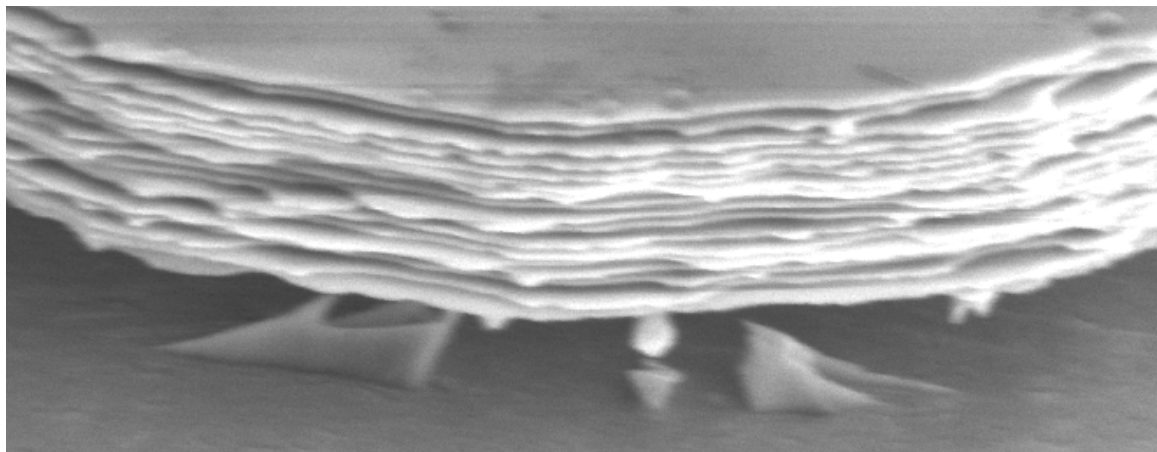
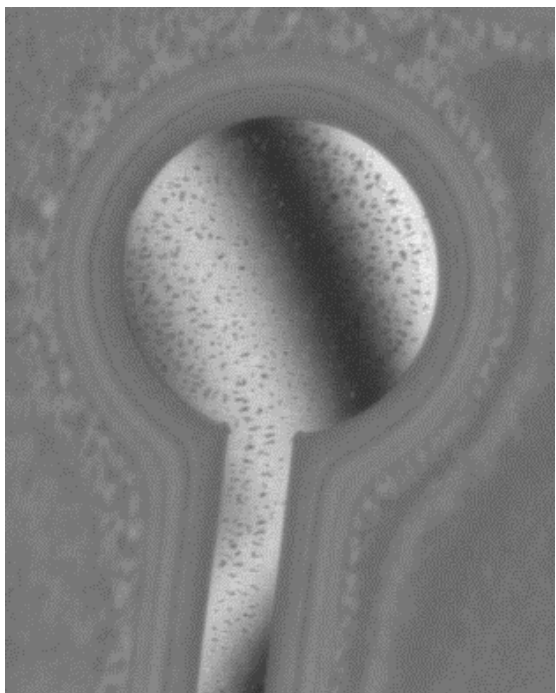
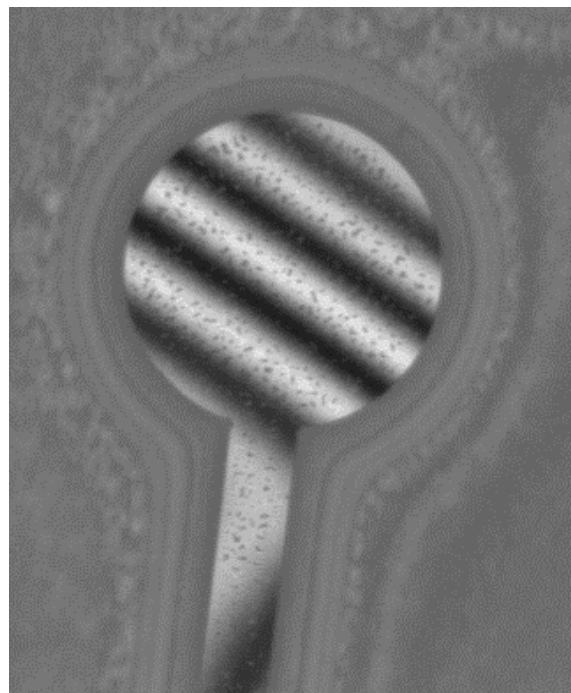


Figure 5.5 SEM images of residual material left behind after a release etch.



(a)



(b)

Figure 5.6 Zygo interferometry system image of a mirror warped during actuation due to incomplete release. (a) Flat mirror with no actuation voltage. (b) Bent mirror with 11 V applied.

5.3.2 Etch Study Mask Design. Determining etch rates by observation of completely remove structures has several shortcomings. It does not account for residual materials left after etching, and there is a greater possibility for false results from fluid mechanical interference while rinsing and drying the sample. To address these problems, I would add bars to the mask that would allow for a mesa definition with a long straight edge. These bars could be oriented at various angles, like my study structures, in order to investigate crystal plane selectivity. After etching, progress can be observed by either cleaving the sample so that the bar is broken near its midpoint or by ion milling into the bar.

5.3.3 Mechanical Structure Mask Design. A second modification to my mask layout that would have been useful is to arrange devices so that they can be packaged. Packaging the devices would have allowed more rapid collection of actuation data than the probing scheme that I used. Packaging would have also reduced the number of structures destroyed by interaction with the probes. This was an improvement that I considered beforehand but did not implement because I wished to have several devices on different orientations relative to the crystal planes in close proximity to one another.

5.4 Contributions

5.4.1 III-V Micromachining. The goal and main accomplishment of the work presented here is to demonstrate the usefulness of two micromachining techniques for III-V materials. These techniques are useful for realizing many III-V MEMS applications, as well as exploiting the desirable optical properties of $\text{Al}_x\text{Ga}_{1-x}\text{As}$. I have verified that these etch techniques are highly selective and that they preserve the optical properties of the material that they do not etch away.

5.4.2 Lift-Off Optical Devices. The work presented in Section 3.5.2 and Section 4.5.3 concerning lift-off optical devices is also valuable in that it provides

one technique that allows the transplantation of optical devices without significant degradation to their quality. Although transplantation was only demonstrated using a sacrificial $\text{AlAs} \Rightarrow \text{Al}_x\text{O}_y$ scheme, my work also suggests another method for removing optical devices by direct etching. GaAs could be selectively removed from beneath an optical device in the same manner used to fabricate my III-V MEMS structures.

5.5 Future Work

5.5.1 Tunable Optical Devices. One direct application of my work is the use of this fabrication technology to fabricate a monolithic tunable VCSEL. The etching methods discussed here could allow a sacrificial layer to be removed near the microcavity of a VCSEL. The resulting air gap could then be adjusted by electrostatic actuation, which would induce tuning in the optical device.

The exploration of lift-off optical devices could facilitate this same sort of tunable optical device. By removing a portion of an active optical device and placing it on an already-fabricated MEMS structure with a reflective surface beneath it, one could create a coupled-cavity device that would also exhibit tuning characteristics.

There is also much room for exploration into the possibilities of transplanted optical devices. By adding optical devices to existing integrated circuits, inter- and intra-chip communication will be improved and allow even greater transistor density on the circuits themselves since less wiring will be required. Transplanting optical devices in arrays will allow for a dense array of communication nodes. If the arrays are developed to a point where each device can be actuated individually, each device could be modulated separately, which would effectively multiply bandwidth available by the number of elements in the array without requiring appreciably more space.

5.5.2 Nano-Electro-Mechanical-Systems. Crystalline MEMS can also be exploited to create ever smaller devices. Because the structures I studied are grown

epitaxially, the thickness of their layers can be controlled very precisely. Coupling this precise thickness control with the exact lateral patterning control of electron beam or extreme ultraviolet lithography could yield nanometer-scale mechanical structures. The crystalline nature of the material is more important at this scale, since grain boundaries would cause problems for polycrystalline materials and strength and predictability are concerns for amorphous materials. Key to the development of nano-electro-mechanical-systems is the high-selectivity of the etchants used. As shown previously, even completely exposed thin DBR layers were not attacked by the etch used to remove $\text{Al}_x\text{Ga}_{1-x}\text{As}$ of higher aluminum content (see Figure 4.19). The high selectivity of the GaAs removal etch presented and of oxidation also enable this, though stress due to oxidation may be a concern.

5.5.3 Lift-Off Optical Devices. As discussed in Section 5.4.2, several alternative methods of transplanting optical devices are already apparent. Investigation of these techniques will lead to a greater choice in processing methodology for these types of devices. Having several proven processing techniques at their disposal will give designers and engineers greater flexibility to exploit the possibilities of lift-off optical devices.

To enable direct removal of an AlAs sacrificial layer from beneath an optical device, a new type of DBR structure with lower aluminum content must be designed. Several aspects of this DBR design bear further study. First, the consequences of using GaAs and $\text{Al}_{0.5}\text{Ga}_{0.5}\text{As}$ for the alternating layers need to be studied from both an optical and a processing standpoint. Second, other materials should be investigated for possible growth analogous to the $\text{Al}_x\text{Ga}_{1-x}\text{As}$ system. This could include other III-V materials, II-VI materials, amorphous films, or plastic films. These materials could be studied to find a suitable crystal lattice match or thin film spin-on method, then the optical properties modelled to demonstrate performance, and finally the processing issues investigated. The mechanical properties of these materials could also be investigated to provide a basis of knowledge for modelling.

5.6 Conclusion

The work I presented in this thesis is intended to help develop a basic technology for the fabrication of III-V MOEMS. These systems are important because they have much of the functionality of silicon MEMS, but also allow better interaction with and control of light. At present, the majority of computer and voice communications use light pulses to send data. The use of tiny, tunable devices to facilitate a more efficient use of conventional glass fiber transmission media, already in place, is of prime importance. This work was intended to support the development of a tunable VCSEL which, as discussed in Section 1.1.1, will allow for wavelength division multiplexing that makes more efficient use of current communication infrastructure. This application is of concern to the Air Force and the Department of Defense because information superiority is a core competency that the military must maintain to enable successful operations. In addition to information superiority, these devices will enable smaller, faster, lighter, and less expensive communications aboard weapons systems, as well as facilitating applications like portable spectroscopy that will enhance force protection.

Bibliography

1. Lee, Y.-S., Upadhyaya, K., Nordheden, J., and Kao, M.-Y. “Selective Reactive Ion Etching of GaAs/AlAs in BCl_3/SF_6 for gate recess,” *Journal of Vacuum Science and Technology, B*, 18(5):2505–2508 (September/October 2000).

Appendix A. Processing Recipes

A.1 Dry Etch Study Processing Recipe

Dry Etch Study		
24 February 2002		Piece ID: G2-2696, G2-2718, and G2-2722
Init.	Process	Notes
Before Entering the Clean Room		
Identify Wafers Model RIE (Reflectivity for Mesa Etch) Request that RIE system be "baked out"		
Initial Processing for All Samples		
1)	Prepare Wafer Surface Spin clean wafer with acetone, methanol, isopropyl alcohol, and DIW 30 seconds each @ 500 rpm N ₂ blow dry 2 minute hot plate bake (HPB) @ 110° C (<i>removes accumulated H₂O</i>) Cool	
2)	1818 Resist Spin On 2 min HPB @ 110° C Set photoresist spinner ramp rate = 200; spin = 4000 rpm Flood wafer with 1818 Spin 30 seconds @ 4000 rpm 1:15 minute HPB @ 110° C Cool	
3)	Edge Bead Removal Flood expose edge bead mask for 2 min (2mw/cm ²) Develop for 60 seconds using 351 developer Swab off corners and edges w/ Acetone DI rinse, N2 dry	
4)	Mesa Contact Mask Expose mesa contact mask for 2 min (2mw/cm ²) Develop for 30 seconds using 351 developer DI rinse, N2 dry Microscope inspect to ensure alignment Clean mask using acetone wipe and N ₂ dry	
5)	Step Height Profile Prior to Mesa RIE etch Measure step height using TENCOR profilometer	Step Height: _____
7)	Mesa RIE Etch Set up reflectance monitoring equipment on ICP etcher PC – double click on RIE Reflectance Change time interval to 0.1 (seconds) Etch 3-4 HL pairs past Microcavity using reflectance data Clean wafer and sapphire holder using acetone swabs	
8)	Post RIE Step Height Measurement (w/ 1818 resist) Measure step height using TENCOR profilometer	Step Height: _____
9)	1818 Resist Removal Remove remaining 1818 resist using acetone spray, acetone rinse, methanol rinse, isopropanol rinse, and N ₂ dry Microscope inspect	

Dry Etch Study

24 February 2002

Piece ID: G2-2696, G2-2718, and G2-2722

Init.	Process	Notes
	10) Post RIE Step Height Measurement (after 1818 resist removal) Measure step height using TENCOR profilometer	Step Height: _____
	Begin Preliminary Etch Study	
	11) Cleave wafers into quarters Use wafer cleaver to cut wafer into quarters Keep track of crystal plane orientation Clean wafer pieces Spin clean wafer with acetone, methanol, isopropyl alcohol, and DIW 30 seconds each @ 500 rpm N ₂ blow dry 2 minute hot plate bake (HPB) @ 100° C (<i>removes accumulated H₂O</i>) Cool Clean back side with acetone rub	
	12) 1818 Resist Spin On 2 min HPB @ 110° C Set photoresist spinner ramp rate = 200; spin = 4000 rpm Flood wafer with 1818 Spin 30 seconds @ 4000 rpm 1:15 minute HPB @ 110° C Cool	
	13) Edge Bead Removal Flood expose edge bead mask for 2 min (2mw/cm ²) Develop for 60 seconds using 351 developer Swab off corners and edges w/ Acetone DI rinse, N2 dry	
	14) Mesa Contact Mask Expose mesa contact mask (same as previous) for 2 min (2mw/cm ²) Develop for 30 seconds using 351 developer DI rinse, N2 dry Microscope inspect to ensure alignment Clean mask using acetone wipe and N ₂ dry	
	15) Step Height Profile Prior to Preliminary RIE Selective etch Measure step height using TENCOR profilometer	Step Height: _____
	16) Characterize Structure Before GaAs Etch Take SEM image and measurements of mesas before etching Ensure photoresist is covering mesas properly (good alignment)	
	17) Perform Center Point (Preliminary) RIE Remove native oxide immediately before etching <ul style="list-style-type: none"> ■ Mix solution of 1:10 HCl:isopropanol ■ Immerse in solution for 30 seconds ■ Rinse in isopropanol for 60 seconds ■ N₂ Blow dry Oxide removal must take place less than 60 minutes before etch	

Dry Etch Study

24 February 2002

Piece ID: G2-2696, G2-
2718, and G2-2722

Init.	Process	Notes
	<p>Perform preliminary RIE selective etch using</p> <ul style="list-style-type: none"> ■ 50 W RIE ■ 0 W ICP ■ 50 mT pressure ■ 2.5 sccm BCl_3 (May need to be 3 based on machine input specs) ■ 7.5 sccm SF_6 (May need to be 8 based on machine input specs) ■ 20 °C ■ 10 minutes 	
	<p>18) Step Height Profile After to Preliminary RIE selective etch Measure step height using TENCOR profilometer</p>	Step Height: _____
	<p>19) 1818 Resist Removal Remove remaining 1818 resist using acetone spray, methanol rinse, isopropanol rinse, and N₂ dry Microscope inspect</p>	
	<p>20) Step Height Profile After 1818 Resist Removal Measure step height using TENCOR profilometer</p>	Step Height: _____
	<p>21) Observe Lateral Etching Using SEM Measure selectivity if possible <ul style="list-style-type: none"> ○ Measure lateral of bottom layer of top DBR (right next to sacrificial layer) vs. lateral of sacrificial GaAs ○ Measure vertical of exposed bottom DBR vs. lateral of sacrificial GaAs ○ Measure vertical into bottom of top DBR vs. lateral of sacrificial GaAs Look for some GaAs etching, but not total removal <ul style="list-style-type: none"> ○ If results not reasonable contact Lt Col Weston for redefinition of experimental parameters ○ With new parameters, perform steps 12-23 with another sample If preliminary etch looks good, then continue</p>	
	Dry Etch Study	
	<p>22) 1818 Resist Spin On 2 min HPB @ 110° C Set photoresist spinner ramp rate = 200; spin = 4000 rpm Flood wafer with 1818 Spin 30 seconds @ 4000 rpm 1:15 minute HPB @ 110° C Cool</p>	
	<p>23) Edge Bead Removal Flood expose edge bead mask for 2 min (2mw/cm²) Develop for 60 seconds using 351 developer Swab off corners and edges w/ Acetone DI rinse, N2 dry</p>	
	<p>24) Mesa Contact Mask Expose mesa contact mask (same as previous) for 2 min (2mw/cm²) Develop for 30 seconds using 351 developer DI rinse, N2 dry Microscope inspect to ensure alignment</p>	

Dry Etch Study

24 February 2002

Piece ID: G2-2696, G2-2718, and G2-2722

Init.	Process	Notes																																																												
	Clean mask using acetone wipe and N ₂ dry																																																													
	25) Step Height Profile Prior to RIE Selective etch Measure step height using TENCOR profilometer	Step Height: _____																																																												
	26) Perform Experimental RIEs Remove native oxide immediately before each etch <ul style="list-style-type: none"> ■ Mix solution of 1:10 HCl:ethanol ■ Immerse in solution for 30 seconds ■ Rinse in ethanol for 60 seconds ■ N₂ Blow dry Oxide removal must be performed less than 60 minutes before etching Etch sample using the following parameters in the order given <table border="1"> <thead> <tr> <th>Order</th><th>BCL₃ Flow (sccm)</th><th>SF₆ Flow (sccm)</th><th>RIE Power (W)</th><th>Pressure (mT)</th><th>Temp (°C)/Time (min)</th></tr> </thead> <tbody> <tr><td>5</td><td>2.5</td><td>6.5</td><td>40</td><td>30</td><td>20 °C/10 min</td></tr> <tr><td>7</td><td>2.5</td><td>6.5</td><td>40</td><td>70</td><td>20 °C/10 min</td></tr> <tr><td>1</td><td>2.5</td><td>6.5</td><td>60</td><td>30</td><td>20 °C/10 min</td></tr> <tr><td>3</td><td>2.5</td><td>6.5</td><td>60</td><td>70</td><td>20 °C/10 min</td></tr> <tr><td>6</td><td>2.5</td><td>8.5</td><td>40</td><td>30</td><td>20 °C/10 min</td></tr> <tr><td>4</td><td>2.5</td><td>8.5</td><td>40</td><td>70</td><td>20 °C/10 min</td></tr> <tr><td>8</td><td>2.5</td><td>8.5</td><td>60</td><td>30</td><td>20 °C/10 min</td></tr> <tr><td>2</td><td>2.5</td><td>8.5</td><td>60</td><td>70</td><td>20 °C/10 min</td></tr> <tr><td>9</td><td>2.5</td><td>7.5</td><td>50</td><td>50</td><td>20 °C/10 min</td></tr> </tbody> </table> Samples should be etched in rapid succession and all within one day if possible <ul style="list-style-type: none"> ○ If not possible, another preliminary sample should be processed before restarting the etch study to ensure consistency 	Order	BCL ₃ Flow (sccm)	SF ₆ Flow (sccm)	RIE Power (W)	Pressure (mT)	Temp (°C)/Time (min)	5	2.5	6.5	40	30	20 °C/10 min	7	2.5	6.5	40	70	20 °C/10 min	1	2.5	6.5	60	30	20 °C/10 min	3	2.5	6.5	60	70	20 °C/10 min	6	2.5	8.5	40	30	20 °C/10 min	4	2.5	8.5	40	70	20 °C/10 min	8	2.5	8.5	60	30	20 °C/10 min	2	2.5	8.5	60	70	20 °C/10 min	9	2.5	7.5	50	50	20 °C/10 min	
Order	BCL ₃ Flow (sccm)	SF ₆ Flow (sccm)	RIE Power (W)	Pressure (mT)	Temp (°C)/Time (min)																																																									
5	2.5	6.5	40	30	20 °C/10 min																																																									
7	2.5	6.5	40	70	20 °C/10 min																																																									
1	2.5	6.5	60	30	20 °C/10 min																																																									
3	2.5	6.5	60	70	20 °C/10 min																																																									
6	2.5	8.5	40	30	20 °C/10 min																																																									
4	2.5	8.5	40	70	20 °C/10 min																																																									
8	2.5	8.5	60	30	20 °C/10 min																																																									
2	2.5	8.5	60	70	20 °C/10 min																																																									
9	2.5	7.5	50	50	20 °C/10 min																																																									
	27) Step Height Profile After to Preliminary RIE selective etch Measure step height using TENCOR profilometer	Step Height: _____																																																												
	28) 1818 Resist Removal Remove remaining 1818 resist using acetone spray, acetone rinse, methanol rinse, isopropanol rinse, and N ₂ dry Microscope inspect																																																													
	29) Step Height Profile After 1818 Resist Removal Measure step height using TENCOR profilometer (see diagram)																																																													
	30) Observe Lateral Etching Using SEM Measure selectivity if possible <ul style="list-style-type: none"> ○ Measure lateral of top structure vs. lateral of sacrificial GaAs ○ Measure vertical of exposed bottom DBR vs. lateral of sacrificial GaAs ○ Measure vertical into bottom of top DBR vs. lateral of sacrificial GaAs 																																																													

A.2 Wet Etch Study for Selective GaAs Removal Processing Recipe

Wet Etch Study—GaAs Sacrificial				
24 February 2002		Piece ID: G2-2696, G2-2718, or G2-2722		
Date Time	Init.	Process	Notes	
		Before Starting Etch Study		
		Using samples already mesa etched for dry etch study, so no pre-processing is necessary		
		Begin Etch Study		
		1) Cleave wafers into small pieces Use wafer cleaver to cut wafer into desired size of study piece Keep track of crystal plane orientation Clean wafer pieces 2 minute hot plate bake (HPB) @ 110° C (<i>removes accumulated H₂O</i>) Cool Clean back side with acetone rub		
		2) Mount samples to microscope slide <ul style="list-style-type: none"> ○ Place slide on hot plate heated to > 130 °C ○ Rub crystal bond 509 onto slide—allow enough to melt on to completely surround the sample ○ Place sample onto melted crystal bond ○ Remove slide and sample from hot plate and allow to cool 		
		3) Clean sample to remove excess crystal bond Spin clean wafer with acetone, methanol, and isopropyl alcohol for 30 seconds each @ 500 rpm N ₂ blow dry		
		4) Measure out dry chemicals <ul style="list-style-type: none"> ○ Citric Acid (C₆H₈O₇)—place 0.961 g into petri dish ○ Tripotassium Citrate (K₃C₆H₅O₇)—place 1.622 g into same petri dish ○ Cover dish and set aside 		
		5) Clean sample with O₂ Plasma <ul style="list-style-type: none"> ○ Place sample in barrel etcher for 12 minutes ○ Power should be set to 200 W 		
		6) Complete mixture of etching solution <ul style="list-style-type: none"> ○ While sample is in the oxygen asher, add 20 mL of water and 3 mL of hydrogen peroxide (H₂O₂ 30%) ○ Agitate solution until all salts are completely dissolved ○ Place petri dish containing solution on a hot plate set for 25 °C 		
		7) Remove oxide immediately prior to etch experiment Dip 60 seconds in BOE:DIW 1:7, gently agitate by swinging the dipping basket back and forth Rinse 3, 30 second cycles in DIW rinse tank N ₂ blow dry		
		8) Place sample in etching solution <ul style="list-style-type: none"> ○ Immerse the mounted sample in to the solution prepared before ○ Start timing when liquid covers the semiconductor surface (solution has a tendency to bead up around the sample) ○ Immediately cover dish with foil to keep light out 		

Wet Etch Study—GaAs Sacrificial

25 February 2002		Piece ID: G2-2696, G2-2718, or G2-2722
Date Time	Init.	Process
		9) Stop Etch o When time has expired, place the mounted sample into a dipping basket and place in DI rinse tank for 3, 30 second cycles
		End

A.3 Oxidation Etch Study Processing Recipe

Oxidation Etch Study		Piece ID: UNM Run 1152
Init.	Process	Notes
	Before Entering the Clean Room	
	Model RIE (Reflectivity for Mesa Etch)	
	Metalization	
	1) Prepare Wafer Surface Cleave wafer and use one quarter for study Spin clean wafer with acetone, methanol, isopropyl alcohol, and DIW 30 seconds each @ 500 rpm N ₂ blow dry 2 minute hot plate bake (HPB) @ 110° C (<i>removes accumulated H₂O</i>) Cool	
	2) XP LOR 3A Coat Set spinner ramp rate = 200 ; spin 4000 rpm Coat sample with XP LOR 3A Spin 30 seconds @ 4K rpm 2 minute HPB @ 170° C Cool	
	3) 1805 Coat Set photoresist spinner ramp rate = 200; spin = 4000 rpm Flood wafer with 1805 Spin 30 seconds @ 4000 rpm 1:15 minute HPB @ 110° C Cool	
	4) Edge Bead Removal Flood expose edge bead mask for 2 min (2mw/cm ²) Develop for 30 seconds using LDD26W developer DI rinse, N ₂ dry	
	5) Metalization Contact Mask Expose mesa contact mask for 17.5 sec (2mw/cm ² , 405 nm) Spin develop for 75 seconds at 1000 RPM using LDD26W developer DI rinse for 30 sec, N ₂ dry Microscope inspect to ensure alignment Clean mask using acetone wipe and N ₂ dry	
	6) Clean to ensure no photoresist in metal contact areas 1 cycle in oxygen ash (4 minutes at 200 W)	
	7) Place metalization order Deposit 200 Å Ti, 1330 Å Au	
	8) Remove oxide immediately prior to metal deposition Dip 30 seconds in BOE:DIW 1:7 Rinse 3, 30 second cycles in DIW rinse tank Thoroughly N ₂ blow dry	
	9) Metal Lift Off Acetone Spray lift off (as necessary, no more than 30 sec at a time) Methanol, Isopropanol rinse, 30 seconds each N ₂ dry	

Oxidation Etch Study

24 February 2002

Piece ID:

UNM Run 1152

Init.	Process	Notes
	10) XPLOR 3A Removal Immerse sample in 1165 stripper heated to 90 –100 °C for 5 minutes DI rinse, 3, 30 second cycles in rinse tank N ₂ dry	
	“Lap” DBR Layer for In-Situ Monitoring	
	11) 1818 Resist Spin On 2 min HPB @ 110° C Set photoresist spinner ramp rate = 200; spin = 4000 rpm Flood wafer with 1818 Spin 30 seconds @ 4000 rpm 1:15 minute HPB @ 110° C Cool	
	12) Edge Bead Removal Flood expose edge bead mask for 2 min (2mw/cm ²) Develop for 30 seconds using LDD26W developer DI rinse, N2 dry	
	13) “Lapping” contact mask Use alignment marks and drop-out to ensure alignment with metal Expose lapping contact mask for 2 min (2mw/cm ² , 405 nm) Develop for 30 seconds using 351 developer DI rinse for 30 sec, N2 dry Microscope inspect to ensure alignment Clean mask using acetone wipe and N ₂ dry	
	14) Step Height Profile Prior to “Lapping” RIE Measure step height using TENCOR profilometer (see diagram)	Step Height: _____
	15) “Lapping” RIE Etch Set up reflectance monitoring equipment on ICP etcher PC – double click on RIE Reflectance Change time interval to .1 (seconds) Mount sample on sapphire holder using diffusion pump oil (<i>use a SMALL amount of oil, otherwise it will contaminate wafer surface!</i>) Etch to ~2 HL pairs before bulk AlAs layer—end at a reflectivity valley Clean wafer and sapphire holder using isopropanol swabs	Time: _____
	16) Post RIE Step Height Measurement (w/ 1818 resist) Measure step height using TENCOR profilometer	Step Height: _____
	17) 1818 Resist Removal Remove remaining 1818 resist using acetone spray, methanol rinse, isopropanol rinse, and N ₂ dry, 30 seconds each Microscope inspect Clean further in oxygen asher if necessary	
	18) Step Height Profile After 1818 Resist Removal Measure step height using TENCOR profilometer (see diagram)	Step Height: _____

Oxidation Etch Study

24 February 2002

Piece ID:

UNM Run 1152

Init.	Process	Notes
Define Study Structures		
	19) 1818 Resist Spin On Clean with 30 second spin rinse of acetone, methanol, isopropanol, N ₂ dry if necessary (long time elapsed since step 16 or ashler used) 2 min HPB @ 110° C Set photoresist spinner ramp rate = 200; spin = 4000 rpm Flood wafer with 1818 Spin 30 seconds @ 4000 rpm 1:15 minute HPB @ 110° C Cool	
	20) Edge Bead Removal Flood expose edge bead mask for 2 min (2mw/cm ²) Develop for 30 seconds using LDD26W developer DI rinse, N2 dry	
	21) Mesa Contact Mask Use alignment marks and drop-out to ensure alignment with metal Expose mesa contact mask for 2 min (2mw/cm ²) Develop for 30 seconds using 351 developer DI rinse, N2 dry Microscope inspect to ensure alignment Clean mask using acetone wipe and N ₂ dry	
	22) Step Height Profile Prior to Mesa RIE Measure step height using TENCOR profilometer	Step Height: _____
	23) Mesa RIE Etch Set up reflectance monitoring equipment on ICP etcher PC – double click on RIE Reflectance Change time interval to .1 (seconds) Mount sample on sapphire holder using diffusion pump oil (<i>use a SMALL amount of oil, otherwise it will contaminate wafer surface!</i>) Etch through bulk AlAs layer Clean wafer and sapphire holder using isopropanol swabs	
	24) Post RIE Step Height Measurement (w/ 1818 resist) Measure step height using TENCOR profilometer	Step Height: _____
	25) 1818 Resist Removal Remove remaining 1818 resist using acetone spray, methanol rinse, isopropanol rinse, and N ₂ dry Microscope inspect Clean further in oxygen ashler if necessary	
	26) Step Height Profile After 1818 Resist Removal Measure step height using TENCOR profilometer (see diagram)	
Oxidize		
	27) Set up oxidation system Ensure water bottle is full of fresh DIW Set for oxidation at desired temperature (400 °C preliminarily) Set flow parameters according to operating instruction	

Oxidation Etch Study

24 February 2002

Piece ID:

UNM Run 1152

Init.	Process	Notes
	Place sample on heated chuck Note time when water vapor flow is begun	
28)	Observe Oxidation Position microscope objective over "lapped" area of sample with structures Note times when each size of each structure type is "pinched off"	
29)	Halt Oxidation When the desired oxidation progress has been achieved <ul style="list-style-type: none"> ○ Shut-off water vapor valve ○ Shut down system according to instructions—don't forget to turn off the Nitrogen Dewar Remove sample from chamber after it has cooled below 100 °C	
30)	Remove Oxide Dip sample in BOE:DIW 1:1 for 30 seconds Rinse 3, 30 second cycles in DIW rinse tank N ₂ blow dry	
31)	Observe Lateral Etching Using Optical Microscope and SEM Measure selectivity <ul style="list-style-type: none"> ○ Measure lateral of top structure vs. lateral of sacrificial GaAs ○ Measure vertical of exposed bottom DBR vs. lateral of sacrificial GaAs ○ Measure vertical into bottom of top DBR vs. lateral of sacrificial GaAs Check for viability of release process Look for effects of residual stress due to growth and/or oxidation	

A.4 Fabrication of Tunable Fabry-Perot Interferometers

Tunable Fabry-Perot Filters		
24 February 2002		Piece ID: G2-2747 (GaAs Sac) and G2-2738 ($\text{Al}_{0.98}\text{Ga}_{0.02}\text{As}$ Sac)
Init.	Process	Notes
	Metalization	
	1) Prepare Wafer Surface Cleave wafer and use one quarter for study Spin clean wafer with acetone, methanol, and isopropyl alcohol, 30 seconds each @ 500 rpm N ₂ blow dry 2 minute hot plate bake (HPB) @ 110° C (<i>removes accumulated H₂O</i>) Cool	
	2) XP LOR 3A Coat Set spinner ramp rate = 200 ; spin 4000 rpm Coat sample with XP LOR 3A Spin 30 seconds @ 4K rpm 2 minute HPB @ 170° C Cool	
	3) 1805 Coat Set photoresist spinner ramp rate = 200; spin = 4000 rpm Flood wafer with 1805 Spin 30 seconds @ 4000 rpm 1:15 minute HPB @ 110° C Cool	
	4) Edge Bead Removal Flood expose edge bead mask for 2 min (2mw/cm ²) Spin develop (500 rpm) for 30 seconds using LDD26W developer DI rinse, N2 dry	
	5) Metalization Contact Mask Expose ring contact mask for 17.5 sec (2mw/cm ² , 405 nm) Spin develop for 75 seconds at 1000 RPM using LDD26W developer DI rinse for 30 sec, N2 dry Microscope inspect to ensure alignment good development Clean mask using mask cleaner, DI Water, and N ₂ dry	
	6) Step Height Profile Prior to Metal Deposition Measure step height in several places using TENCOR profilometer	Step Height: _____
	7) Clean to ensure no photoresist in metal contact areas 1 cycle(4 min, 200 W) in oxygen asher Put silicon blank in chamber as well	
	8) Place metalization order o 200 Å Ti, 2550 Å Au	
	9) Remove oxide immediately prior to metal deposition Dip 30 seconds in BOE:DIW 1:7 Rinse 3 cycles in DIW rinse tank, N ₂ blow dry	
	10) Metal Lift Off Acetone Spray lift off (as necessary, no more than 30 sec at a time) Methanol, Isopropanol rinse, 30 seconds each N ₂ dry Microscope inspect and repeat as necessary to remove metal	

Tunable Fabry-Perot Filters

24 February 2002

Piece ID: G2-2747 (GaAs Sac)
and G2-2738 (Al_{0.98}Ga_{0.02}As Sac)

Init.	Process	Notes
	11) XPLOR 3A Removal Submerge wafer for 5 minutes in 1165 Stripper heated to 90 °C – 100 °C Rinse 3 cycles in DI rinse tank N ₂ dry	
	12) Step Height Profile after Metal Deposition Measure step height at several locations using TENCOR profilometer	Step Height: _____
	Mesa Etch Structures	
	13) 1818 Resist Spin On 2 min HPB @ 110° C (to drive off water) Set photoresist spinner ramp rate = 200; spin = 4000 rpm Flood wafer with 1818 Spin 30 seconds @ 4000 rpm 1:15 minute HPB @ 110° C Cool	
	14) Edge Bead Removal Flood expose edge bead mask for 2 min (2mw/cm ²) Develop for 30 seconds using LDD26W developer DI rinse, N2 dry	
	15) Mesa Contact Mask Use alignment marks and drop-out to ensure alignment with metal Expose mesa contact mask for 2 min (2mw/cm ² , 405 nm) Develop for 30 seconds using 351 developer DI rinse for 30 sec, N2 dry Microscope inspect to ensure alignment	
	16) Step Height Profile Prior to Mesa RIE Etch Measure step height as several locations using TENCOR profilometer	Step Height: _____
	17) Mesa RIE Etch Mount sample on sapphire holder using diffusion pump oil (<i>use a SMALL amount of oil, otherwise it will contaminate wafer surface!</i>) Etch 3-4 HL pairs past sacrificial layer using reflectance data Clean wafer and sapphire holder using isopropanol swabs	
	Wet Release for GaAs Sacrificial	
	18a) Measure out dry chemicals o Citric Acid (C ₆ H ₈ O ₇)—place 0.961 g into petri dish o Tripotassium Citrate (K ₃ C ₆ H ₅ O ₇)—place 1.622 g into same petri dish o Cover dish and set aside	Step Height: _____
	19a) Clean sample with O₂ Plasma o Place sample in barrel etcher for 40 minutes o Power should be set to 200 W, O ₂ flow to 500 sccm	
	20a) Complete mixture of etching solution o While sample is in the oxygen ash, add 20 mL of water and 3 mL of hydrogen peroxide (H ₂ O ₂ 30%) o Agitate solution until all salts are completely dissolved o Place petri dish containing solution on a hot plate set for 25 °C	Step Height: _____

Tunable Fabry-Perot Filters

24 February 2002

Piece ID: G2-2747 (GaAs Sac)
and G2-2738 (Al_{0.98}Ga_{0.02}As Sac)

Init.	Process	Notes
	21a) Place sample in etching solution <ul style="list-style-type: none"> ○ Immerse the mounted sample in to the solution prepared before ○ Start timing when liquid covers the semiconductor surface (solution has a tendency to bead up around the sample) ○ Immediately cover dish with foil to keep light out 	
	22a) Stop Etch <ul style="list-style-type: none"> ○ When time has expired, rinse sample with methanol and submerge in methanol for transport. DO NOT let the sample dry at any time 	
	Oxidize and Release for AlAs Sacrificial	
	Strip resist by submerging in 1165 stripper heated to 90 °C – 100 °C for five minutes for the oxidation sample	
	18b) Set up oxidation system <p>Ensure water bottle is full of fresh DIW Set for oxidation at desired temperature (400 °C preliminarily) Set flow parameters according to operating instruction Place sample on heated chuck Note time when water vapor flow is begun</p>	
	19b) Time Oxidation <p>Use previous data to determine sufficient time to completely oxidize sacrificial layer under mirror structures—go slightly longer to ensure 100% release</p>	
	20b) Halt Oxidation <p>When the desired oxidation progress has been achieved</p> <ul style="list-style-type: none"> ○ Shut-off water vapor valve ○ Shut down system according to instructions—don't forget to turn off the Nitrogen Dewar <p>Remove sample from chamber after it has cooled below 100 °C</p>	
	21b) Place sample in etching solution <ul style="list-style-type: none"> ○ Immerse the mounted sample in to the oxide removal solution: KOH (1.0 M):DI 1:12 ○ Start timing when liquid covers the semiconductor surface (solution has a tendency to bead up around the sample) ○ Immediately cover dish with foil to keep light out 	
	22b) Stop Etch <ul style="list-style-type: none"> ○ When time has expired, rinse sample with methanol and submerge in methanol for transport. DO NOT let the sample dry at any time 	
	Supercritical CO₂ Drying	
	23) Dry Structures <p>Clean drying chamber with methanol, and place enough methanol to cover sample into chamber.</p> <ul style="list-style-type: none"> ○ If first run of the day, allow a conditioning run <p>Submerge sample in methanol in drying chamber Cool chamber and push Fill to start drying cycle</p>	
	End	

A.5 Fabrication of Lift-off Optical Devices

Lift-off VCSEL Study		
24 February 2002		Piece ID: UNM Run 1184
Init.	Process	Notes
	Metalization	
	1) Prepare Wafer Surface Cleave wafer and use one quarter for study Spin clean wafer with acetone, methanol, and isopropyl alcohol, 30 seconds each @ 500 rpm N ₂ blow dry 2 minute hot plate bake (HPB) @ 110° C (<i>removes accumulated H₂O</i>) Cool	
	2) XP LOR 3A Coat Set spinner ramp rate = 200 ; spin 4000 rpm Coat sample with XP LOR 3A Spin 30 seconds @ 4K rpm 2 minute HPB @ 170° C Cool	
	3) 1805 Coat Set photoresist spinner ramp rate = 200; spin = 4000 rpm Flood wafer with 1805 Spin 30 seconds @ 4000 rpm 1:15 minute HPB @ 110° C Cool	
	4) Edge Bead Removal Flood expose edge bead mask for 2 min (2mw/cm ²) Spin develop (500 rpm) for 30 seconds using LDD26W developer DI rinse, N2 dry	
	5) Metalization Contact Mask Expose ring contact mask for 17.5 sec (2mw/cm ² , 405 nm) Spin develop for 75 seconds at 1000 RPM using LDD26W developer DI rinse for 30 sec, N2 dry Microscope inspect to ensure alignment good development Clean mask using mask cleaner, DI Water, and N ₂ dry	
	6) Step Height Profile Prior to Metal Deposition Measure step height in several places using TENCOR profilometer	Step Height: _____
	7) Clean to ensure no photoresist in metal contact areas 1 cycle(4 min, 200 W) in oxygen ash	
	8) Place metalization order for lift-off VCSEL sample Deposit standard SD contact <ul style="list-style-type: none"> ○ 50 Å Ni ○ 170 Å Ge ○ 330 Å Au ○ 150 Å Ni ○ 3000 Å Au 	
	9) Remove oxide immediately prior to metal deposition Dip 30 seconds in BOE:DIW 1:7 Rinse 3 cycles in DIW rinse tank, N ₂ blow dry	

Lift-off VCSEL Study

24 February 2002

Piece ID:
UNM Run 1184

Init.	Process	Notes
	10) Clean Silicon Blank Spin clean wafer with acetone, methanol, and isopropyl alcohol, 30 seconds each @ 500 rpm N ₂ blow dry 2 minute hot plate bake (HPB) @ 110° C (<i>removes accumulated H₂O</i>) Cool	
	11) Place metalization order for blank 200 Å Ti 2550 Å Au 500 Å Pt 300 Å Ti	
	12) Remove oxide immediately prior to metal deposition Dip 30 seconds in BOE:DIW 1:7 Rinse 3 cycles in DIW rinse tank Thoroughly N ₂ blow dry	
	13) Metal Lift Off from VCSEL material Acetone Spray lift off (as necessary, no more than 30 sec at a time) Methanol, Isopropanol rinse, 30 seconds each N ₂ dry Microscope inspect and repeat as necessary to remove metal	
	14) XPLOR 3A Removal from VCSEL material Submerge wafer for 5 minutes in 1165 Stripper heated to 90 °C – 100 °C Rinse 3 cycles in DI rinse tank N ₂ dry	
	15) Step Height Profile after Metal Deposition Measure step height at several locations using TENCOR profilometer	Step Height: _____
	Mesa Etch Structures	
	16) 1818 Resist Spin On 2 min HPB @ 110° C (to drive off water) Set photoresist spinner ramp rate = 200; spin = 4000 rpm Flood wafer with 1818 Spin 30 seconds @ 4000 rpm 1:15 minute HPB @ 110° C Cool	
	17) Edge Bead Removal Flood expose edge bead mask for 2 min (2mw/cm ²) Develop for 30 seconds using LDD26W developer DI rinse, N2 dry	
	18) Mesa Contact Mask Use alignment marks and drop-out to ensure alignment with metal Expose mesa contact mask for 2 min (2mw/cm ² , 405 nm) Develop for 30 seconds using 351 developer DI rinse for 30 sec, N2 dry Microscope inspect to ensure alignment	

Lift-off VCSEL Study

24 February 2002

Piece ID:
UNM Run 1184

Init.	Process	Notes
	19) Step Height Profile Prior to Mesa RIE Etch Measure step height as several locations using TENCOR profilometer	Step Height: _____
	20) Mesa RIE Etch Mount sample on sapphire holder using diffusion pump oil (<i>use a SMALL amount of oil, otherwise it will contaminate wafer surface!</i>) Etch 3-4 HL pairs past sacrificial layer using reflectance data Clean wafer and sapphire holder using isopropanol swabs	
	21) Post RIE Step Height Measurement (w/ 1818 resist) Measure step height using TENCOR profilometer	Step Height: _____
	22) 1818 Resist Removal Remove remaining 1818 resist using acetone spray, methanol rinse, isopropanol rinse, and N ₂ dry, 30 seconds each Microscope inspect Clean further in oxygen asher if necessary	
	23) Step Height Profile After 1818 Resist Removal Measure step height using TENCOR profilometer	Step Height: _____
	Test Devices Before Release	
	24) Clean Probe Chuck <ul style="list-style-type: none"> ○ Wipe probe chuck with acetone, then with isopropyl alcohol to allow better contact ○ Use vacuum feature to maximize contact to chuck ○ Be aware that this procedure will produce a Schottky contact—threshold voltage will be higher than normal 	
	25) Test Devices <ul style="list-style-type: none"> ○ Place sample on probe stand and probe several devices to determine: <ul style="list-style-type: none"> ○ Whether devices are functional ○ Threshold voltage and current ○ L-I properties, V-I properties of note ○ Power out vs. Wavelength (emission spectra) 	
	Oxidize and Release	
	26) Set up oxidation system Ensure water bottle is full of fresh DIW Set for oxidation at desired temperature (400 °C preliminarily) Set flow parameters according to operating instruction Place sample on heated chuck Note time when water vapor flow is begun	
	27) Time Oxidation Use previous data to determine sufficient time to completely oxidize sacrificial layer	
	28) Halt Oxidation When the desired oxidation progress has been achieved <ul style="list-style-type: none"> ○ Shut-off water vapor valve ○ Shut down system according to instructions—don't forget to turn off the Nitrogen Dewar Remove sample from chamber after it has cooled below 100 °C	

Lift-off VCSEL Study

24 February 2002

Piece ID:
UNM Run 1184

Init.	Process	Notes
	29) Release VCSELs <ul style="list-style-type: none"> o Place gold-coated silicon blank in the bottom of the release vessel <ul style="list-style-type: none"> o Select a vessel where the blank will cover as much of the bottom as possible o Hold sample (using plastic tweezers) in KOH(1.0 M):DIW 1:12 for 15 minutes with occasional side to side movement for agitation o Pull acceptor substrate out of solution and rinse three, 30 second cycles in DIW rinse tank o Bake acceptor substrate at 110 °C until no water is visible o Microscope inspect to ensure novel examples present 	
	30) Anneal New Contacts <ul style="list-style-type: none"> o Place entire sample in rapid thermal annealer at 410 °C for 15 seconds in the presence of forming gas 	
	Test Relocated Devices	
	31) Probe Test <ul style="list-style-type: none"> o Probe gold on top of silicon blank and contact to ground o Probe several devices to determine <ul style="list-style-type: none"> o Whether devices are functional o Threshold voltage and current o L-I properties, V-I properties of note o Power out vs. Wavelength (spectral analysis) 	
	End	

Appendix B. Materials and Epitaxial Growths Used

Material with a G2 prefix was grown at the in the Generation II molecular beam epitaxy system at the Air Force Research Laboratory, Materials and Manufacturing Directorate, Wright-Patterson Air Force Base, OH. Samples with UNM designations were grown by Dr. Andreas Stintz at the University of New Mexico, Albuquerque, New Mexico. In both cases, exact growth conditions are considered proprietary information and are not included here.

Growth Number	Brief Description	Growth Details	Sectors Used
G2-2696	$\text{Al}_{0.1}\text{Ga}_{0.9}\text{As} / \text{Al}_{0.9}\text{Ga}_{0.1}\text{As}$ DBRs surrounding GaAs sacrificial	Appendix B.1	All
G2-2697	AlAs Sacrificial $\text{Al}_{0.9}\text{Ga}_{0.1}\text{As}$ mechanical	Appendix B.2	A and C
G2-2698	GaAs Sacrificial $\text{Al}_{0.1}\text{Ga}_{0.9}\text{As}$ mechanical	Appendix B.3	All lost to residual film
G2-2718	$\text{Al}_{0.1}\text{Ga}_{0.9}\text{As} / \text{Al}_{0.9}\text{Ga}_{0.1}\text{As}$ DBRs surrounding GaAs sacrificial	Appendix B.4	All patterned with circular mesas
G2-2722	$\text{Al}_{0.1}\text{Ga}_{0.9}\text{As} / \text{Al}_{0.9}\text{Ga}_{0.1}\text{As}$ DBRs surrounding GaAs sacrificial	Appendix B.5	All patterned with circular mesas
G2-2738	$\text{Al}_{0.9}\text{Ga}_{0.1}\text{As} / \text{GaAs}$ DBRs surrounding $\text{Al}_{0.98}\text{Ga}_{0.02}\text{As}$ sacrificial	Appendix B.6	A
G2-2747	$\text{Al}_{0.1}\text{Ga}_{0.9}\text{As} / \text{Al}_{0.9}\text{Ga}_{0.1}\text{As}$ DBRs surrounding GaAs sacrificial	Appendix B.7	All
G2-2748	$\text{Al}_{0.1}\text{Ga}_{0.9}\text{As} / \text{Al}_{0.9}\text{Ga}_{0.1}\text{As}$ DBRs surrounding GaAs sacrificial	Appendix B.8	C
UNM Run 1152	$\text{Al}_{0.1}\text{Ga}_{0.9}\text{As} / \text{Al}_{0.9}\text{Ga}_{0.1}\text{As}$ DBR atop AlAs sacrificial	Appendix B.9	All (received only half of wafer)
UNM Run 1184	980 nm VCSEL atop AlAs sacrificial	Appendix B.10	A and C

B.1 Details for Growth G2-2696

MBE# G2-2696a

Layer	(starting at substrate)			Angst.	Sec.	Repeats	Temp. (°V, volt, amp)
AlAs	Si	4e18		1675.1	666		610
Ga1As	Si	4e18		696.03	246.4		
AlGa2As	Si	4e18		812.69	290.6		
AlGa2As/Ga1As	SL	Al x=.1	Si	4e18	708	250.9	/ -- 18 --
AlGa2As	Si	4e18			812.69	290.6	-----/
Ga1As					696.03	246.4	
<hr/>							
Interrupt							
Ga1As				14304			610
AlGa2As	Al x = .9	C	1e19	812.69			
AlGa2As/Ga1As	SL	Al x=.1	C	1e19	708		/ -- 18 --
AlGa2As	Al x = .9	C	1e19	812.69			-----/
Ga1As		C	1e19	696.03			

B.2 Details for Growth G2-2697

MBE# G2-2697

Layer	(starting at substrate)			Angst.	Sec.	Repeats	Temp. (°V, volt, amp)
Ga1Ga2As	S	4e18		500	300		600
AlAs				15000	5543		700
Ga1Ga2As	C	1e19		200	120		600
AlGa1As	C	1e19	x=.9	15000	5257		
Ga1Ga2As	C	1e19		200	120		

B.3 Details for Growth G2-2698

MBE# G2-2698

Layer	(starting at substrate)			Angst.	Sec.	Repeats	Temp. (°V, volt, amp)
AlAs	Si			700	2478		600
Ga1As	>As			15000	6034		
AlGa1As	C	1e19		15000	5363		
Ga1As	C	1e19		200	80.5		

B.4 Details for Growth G2-2718

MBE# G2-2718a

Layer	(starting at substrate)		Angst.	Sec.	Repeats	Temp. (°V, volt, amp)
AlAs	Si	4e18	1675.1	644.5		600
Ga1As	Si	4e18	696.03	249		
AlGa2As	Si	4e18	812.69	282		
AlGa2As/Ga1As	SL Al x=.1 Si	4e18	708	252	/ -- 18 --	
AlGa2As	Si	4e18	812.69	282	-----/	
Ga1As			696.03	249		
<hr/>						
Interrupt						
Ga1As			14304	5063		600
AlGa2As	Al x = .9 C	1e19	812.69	282		
AlGa2As/Ga1As	SL Al x=.1 C	1e19	708	250	/ -- 18 --	
AlGa2As	Al x = .9 C	1e19	812.69	282	-----/	
Ga1As	C	1e19	696.03	246		

B.5 Details for Growth G2-2722

MBE# G2-2722a

Layer	(starting at substrate)		Angst.	Sec.	Repeats	Temp. (°V, volt, amp)
Ga2As	Si		696	243.94	/ -- 38 --	610
AlGa1As	Si		812.69	284.83	-----/	
Ga2As	Si <Si		696	243.94		
AlGa2As	Si x=.9		786	281		610
Ga1As/AlGa2As (DA)	Si x=.1		682.12	239.67	/ --- 3 ---	
AlGa2As	Si		786	281	-----/	
Ga1As			15000	5257		
As	>C			300		
AlGa2As	C		786	281		
Ga1As/AlGa2As (DA)	C x=.1		682.12	239.67	/ --- 18 ---	
AlGa2As	C		786	281	-----/	
Ga1As	C		670.58	235		

B.6 Details for Growth G2-2738

MBE# G2-2738a

Layer	(starting at substrate)			Angst.	Sec.	Repeats	Temp. (°V, volt, amp)
AlGa2As	Si	4e18	x=.9	809.97	281	/ -- 15 --	610
Ga1As	Si	4e18		694.92	246	-----/	
AlGa2As	Si	4e18	x=.9	809.97	281		
Ga1As	Si	8e18		694.92	246		
AlGa2As				15000	5589		610
As					475		
Ga1As	C	4e19		694.92	248		
AlGa2As	C	1e19	x=.1	809.97	283.9	/ -- 10 --	610
Ga1As	C	1e19		694.92	251	-----/	

B.7 Details for Growth G2-2747

MBE# G2-2747a

Layer	(starting at substrate)			Angst.	Sec.	Repeats	Temp. (°V, volt, amp)
Ga2As	Si			696	246.38	/ -- 38 --	610
AlGa1As	Si			812.69	273.98	-----/	
Ga2As	Si	<Si		696	246.38		
AlGa1As	Si		x=.9	786	267.53		610
Ga2As/AlGa1As (DA)	Si	x=.1		682.12	240.4	/ --- 3 ---	
AlGa1As	Si			786	267.53	-----/	
Ga2As				15000	5310		
As		>C			350		
AlGa1As	C			786	267.53		
Ga2As/AlGa1As (DA)	C	x=.1		682.12	240.4	/ --- 18 ---	
AlGa1As	C			786	267.53	-----/	
Ga2As	C			670.58	237.37		

B.8 Details for Growth G2-2748

MBE# G2-2748

Layer (starting at substrate)			Angst.	Sec.	Repeats	Temp. (°V, volt, amp)
AlGa1As	Si	4e18	x=.9	812.68	274	/-- 38 -- 610
Ga2As	Si	4e18		696	249	-----/
interrupt to load second half of program						
AlGa1As	Si	4e18	x=.9	812.68	274	/-- 3 --
Ga2As/AlGa1As (DA)	Si	4e18	x=.1	708	251.6	-----/
Ga2As				15000	5363	
As	>C				475	
Ga2As/AlGa1As (DA)	C	4e19	x=.1	708	251.6	
As	<C				150	
AlGa1As	C	1e19	x=.9	812.68	274	/--- 9 ---
Ga2As/AlGa1As (DA)	C	1e19	x=.1	708	251.6	-----/
AlGa1As	C	1e19	x=.9	812.68	274	
As	>C				150	
Ga2As/AlGa1As (DA)	C	4e19	x=.1	708	251.6	

B.9 Growth Details for UNM Run 1152

Material	Doping	Thickness	Repeats
GaAs	n 2 ¹⁸	60.6 nm	
Al _{0.1} Ga _{0.9} As→Al _{0.9} Ga _{0.1} As graded superlattice	n 2 ¹⁸	18 nm	30
Al _{0.9} Ga _{0.1} As	n 2 ¹⁸	63.8 nm	30
Al _{0.9} Ga _{0.1} As→Al _{0.1} Ga _{0.9} As graded superlattice	n 2 ¹⁸	18 nm	30
GaAs	n 2 ¹⁸	51.6 nm	
AlAs	n 2.2 ¹⁸	329 nm	
GaAs	n 2 ¹⁸	200 nm	
GaAs Substrate	n		

B.10 Growth Details for UNM Run 1184

1184) GaAs,p3.5¹⁸ 9nm
 GaAs,p3.5¹⁸ 51.6nm, 14x
 Al_{9.0}Ga_{1.1}As,p3.5¹⁸ 18nm, 14x
 Al₉Ga₁As,p3.5¹⁸ 63.8nm, 14x
 Al_{0.9}Ga_{1.1}As,p3.5¹⁸ 18nm, 14x
 GaAs,p1¹⁷ 51.6nm, 3x
 Al_{9.0}Ga_{1.1}As,p1¹⁷ 18nm, 3x
 Al₉Ga₁As,p1¹⁷ 63.8nm, 3x
 Al_{0.9}Ga_{1.1}As,p1¹⁷ 18nm, 3x
 GaAs,p1¹⁷ 51.6nm
 Al_{9.0}Ga_{1.1}As,p1¹⁷ 18nm
 Al_{.98}Ga_{.02}As,p1¹⁷ 20.6nm
 Al₉Ga₁As,p1¹⁷ 52.4nm
 Al₅Ga₅As,p1¹⁷ 72nm
 Al₅Ga₅As 50nm
 GaAs 4nm
 GaAs 5.2nm, 3x 590C
 GaAs 0.8nm, 3x
 In_{.161}Ga_{.839}As 8nm, 3x
 InAs .805ML, 3x 510C
 GaAs 10nm
 Al_xGa_{1-x}As 50nm
 Al₅Ga₅As,n1¹⁷ 72nm
 Al₉Ga₁As,n1¹⁷ 52.4nm
 Al_{.98}Ga_{.02}As,n1¹⁷ 20.6nm
 Al_{0.9}Ga_{1.1}As,n1¹⁷ 18nm
 GaAs,n1¹⁷ 51.6nm
 Al_{9.0}Ga_{1.1}As,n1¹⁷ 18nm, 3x
 Al₉Ga₁As,n1¹⁷ 63.8nm, 3x
 Al_{0.9}Ga_{1.1}As,n1¹⁷ 18nm, 3x
 GaAs,n1¹⁷ 51.6nm, 3x
 Al_{9.0}Ga_{1.1}As,n2¹⁸ 18nm, 27x
 Al₉Ga₁As,n2¹⁸ 63.8nm, 27x
 Al_{0.9}Ga_{1.1}As,n2¹⁸ 18nm, 27x
 GaAs,n2¹⁸ 51.6nm, 27x
 GaAs,n2¹⁸ 9nm
 AlAs,n2.2¹⁸ 329nm
 GaAs,n2¹⁸ 200nm
 GaAs N 2" 1-side AXT G059S5188

REPORT DOCUMENTATION PAGE				Form Approved OMB No. 074-0188
<p>The public reporting burden for this collection of information is estimated to average 1 hour per response, including the time for reviewing instructions, searching existing data sources, gathering and maintaining the data needed, and completing and reviewing the collection of information. Send comments regarding this burden estimate or any other aspect of the collection of information, including suggestions for reducing this burden to Department of Defense, Washington Headquarters Services, Directorate for Information Operations and Reports (0704-0188), 1215 Jefferson Davis Highway, Suite 1204, Arlington, VA 22202-4302. Respondents should be aware that notwithstanding any other provision of law, no person shall be subject to a penalty for failing to comply with a collection of information if it does not display a currently valid OMB control number.</p> <p>PLEASE DO NOT RETURN YOUR FORM TO THE ABOVE ADDRESS.</p>				
1. REPORT DATE (DD-MM-YYYY) 26-03-2002	2. REPORT TYPE Master's Thesis	3. DATES COVERED (From – To) Jun 2001 – Mar 2002		
4. TITLE AND SUBTITLE FABRICATION TECHNIQUES FOR III-V MICRO-OPTO-ELECTRO-MECHANICAL SYSTEMS		5a. CONTRACT NUMBER		
		5b. GRANT NUMBER		
		5c. PROGRAM ELEMENT NUMBER		
6. AUTHOR(S) Raley, Jeremy A., Captain, USAF		5d. PROJECT NUMBER		
		5e. TASK NUMBER		
		5f. WORK UNIT NUMBER		
7. PERFORMING ORGANIZATION NAMES(S) AND ADDRESS(S) Air Force Institute of Technology Graduate School of Engineering and Management (AFIT/EN) 2950 P Street, Building 640 WPAFB OH 45433-7765		8. PERFORMING ORGANIZATION REPORT NUMBER AFIT/GE/ENG/02M-21		
9. SPONSORING/MONITORING AGENCY NAME(S) AND ADDRESS(ES) AFRL/SNDD Attn: Dr. Thomas R. Nelson, Jr. 2241 Avionics Circle, Rm. C2G69 WPAFB OH 45433-7322		10. SPONSOR/MONITOR'S ACRONYM(S)		
		11. SPONSOR/MONITOR'S REPORT NUMBER(S)		
12. DISTRIBUTION/AVAILABILITY STATEMENT APPROVED FOR PUBLIC RELEASE; DISTRIBUTION UNLIMITED.				
13. SUPPLEMENTARY NOTES				
<p>14. ABSTRACT</p> <p>This thesis studies selective etching techniques for the development of $\text{Al}_x\text{Ga}_{1-x}\text{As}$ micro-opto-electro-mechanical systems (MOEMS). New MEMS technology based on materials such as $\text{Al}_x\text{Ga}_{1-x}\text{As}$ enables the development of micro-systems with embedded active micro-optical devices. Tunable micro-lasers and optical switching based on MOEMS technology will improve future wavelength division multiplexing (WDM) systems. WDM vastly increases the speed of military communications and sensor data processing.</p> <p>From my designs, structures are prepared by molecular beam epitaxy. I design a mask set for studies of crystal plane selectivity. I perform a series of experiments on the selective removal of GaAs and AlAs. I convert AlAs and $\text{Al}_{0.98}\text{Ga}_{0.02}\text{As}$ layers within the test structures to AlO_x and $\text{Al}_{0.98}\text{Ga}_{0.02}\text{O}_x$ and perform selective etching experiments on these sacrificial oxide layers. The etchants and materials studied showed high selectivity for removal of all materials studied. Results suggest that any of these material layers are useful as sacrificial layers for general MOEMS technology.</p> <p>I design, fabricate, and characterize prototype III-V MOEMS. Using AlO_x sacrificial layers, I investigate a new technique for transplanting microcavity light-emitting devices. I successfully transplant arrays of light-emitting diodes. Finally, I discuss ideas on how this work forms the basis for nano-electro-mechanical systems (NEMS) fabrication in III-V materials.</p>				
<p>15. SUBJECT TERMS</p> <p>Microelectromechanical Systems, Aluminum Gallium Arsenide, Etching, Oxidation, Micromachining Micro-Opto-Electro-Mechanical Systems, III-V Micromachining, Lift-off Optical Devices</p>				
16. SECURITY CLASSIFICATION OF:		17. LIMITATION OF ABSTRACT	18. NUMBER OF PAGES	19a. NAME OF RESPONSIBLE PERSON James A. Lott, Lt Col, USAF (ENG)
a. REPORT U	b. ABSTRACT U	c. THIS PAGE U	UU	19b. TELEPHONE NUMBER (Include area code) (937) 255-3636, ext 4576; e-mail: James.Lott@afit.edu